A Novel Approach to Modeling Arbitrary Damage in Composite Structures through a Discontinuous Galerkin Cohesive Zone Model

Filippo Maggioli

Delft University of Technology

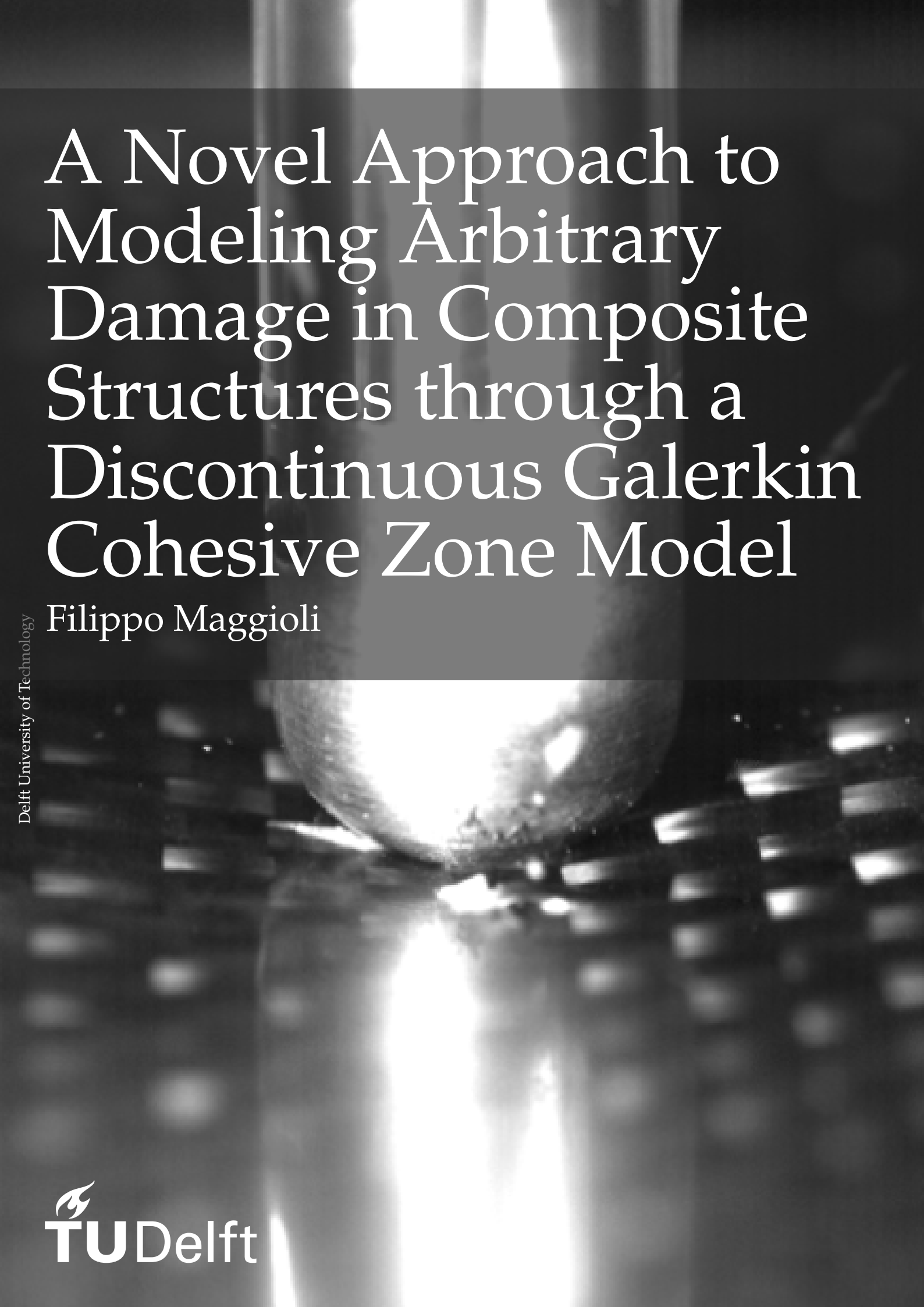

TU Delft

A Novel Approach to Modeling Arbitrary Damage in Composite Structures through a Discontinuous Galerkin Cohesive Zone Model

by

Filippo Maggioli

to obtain the degree of Master of Science
at the Delft University of Technology,
to be defended publicly on Monday April 29, 2024 at 09:00.

Student number:	5248760	
Project duration:	March 7, 2022 – April 29, 2024	
Thesis committee:	Dr. B. Giovanardi,	TU Delft, supervisor
	Dr.ir. J.-A. Pascoe,	TU Delft, supervisor
	Dr. D.M.J. Peeters,	TU Delft, chair
	Dr. B. Çağlar,	TU Delft, external member

Cover:	Illustration of an impactor hitting a composite laminate, courtesy of [1]
Style:	TU Delft Report Style, with modifications by Daan Zwaneveld

An electronic version of this thesis is available at `http://repository.tudelft.nl/`.

TU Delft

Preface

This report presents the findings of my master's thesis in Aerospace Structures and Materials conducted at the Technical University of Delft. The thesis focuses on enhancing damage modeling techniques for composite materials, which are increasingly prevalent in the aerospace industry. Specifically, the goal is to address the limitations of the Cohesive Zone Model (CZM) in allowing arbitrary damage development in composites. The objective is to improve the accuracy of damage description and reduce its reliance on preliminary experimental data.

The research comprised a comprehensive literature review of damage modeling techniques suitable for composite structures. This was followed by the development of a novel CZM damage formulation capable of facilitating arbitrary damage development in composites based solely on the structural stress state. Subsequently, the novel formulation was implemented in Summit-lite, a Finite Element (FE) object-oriented research code. The implementation was verified against a simple analytical model and validated against experimental data to evaluate the method's suitability for arbitrary damage modeling in composites.

I extend my gratitude to Bianca Giovanardi and John-Alan Pascoe for their constant and enthusiastic guidance throughout this project. Their approach of blending step by step critical analysis with a wider holistic perspective on this research topic was truly inspiring. Additionally, I would like to thank Sai Kubair Kota for his willingness to address my queries regarding coding and fracture mechanics. Finally, to my family, friends and colleagues, I am grateful for your unwavering support throughout this journey.

Filippo Maggioli
Delft, April 2024

Summary

Composite structures have become increasingly popular in the aerospace industry due to their exceptional high specific properties (Shah et al. [2], Bui and Hu [3]). However, compared to traditional metal structures, composites are more susceptible to sudden failure due to their brittle nature (Davies and Olsson [4]). This vulnerability is particularly pronounced in scenarios such as impact events, where detecting damage occurrence during regular inspections can be complex and expensive ([4]). Therefore, employing accurate damage modeling techniques becomes crucial to ensure structural integrity and define design allowables that guarantee sufficient residual strength up to the damage detectability threshold (Shah et al. [2]).

Finite Element Methods (FEMs) are widely employed for damage simulation in composites, with the Cohesive Zone Model (CZM) being particularly favored for its robustness and scalability (Radovitzky et al. [5]). The CZM has the potential to capture composites' complex damage mechanisms including delaminations, matrix cracking, and simultaneous fiber and matrix cracking (Wisnom [6]). Despite the CZM's mesh-dependent nature, the Discontinuous Galerkin Cohesive Zone Model (DG/CZM) formulation allows for relatively arbitrary crack propagation: the DG/CZM facilitates highly refined meshes, reducing the mesh-dependency of the CZM (Radovitzky et al. [5]). This is enabled by the DG/CZM's extrinsic damage formulation, which allows cohesive damage to evolve at any internal boundary without introducing inconsistency ([5]). Moreover, the DG/CZM is highly suitable for parallel implementation, as mesh and data structures reliant on the mesh do not require redefinition upon crack propagation ([5]). Scalability is crucial for damage simulation in composites due to its high computational load (Bogenfeld et al. [7]), making the DG/CZM's parallel implementation particularly advantageous as it enables drastic reductions in simulation times (Radovitzky et al. [5]).

However, a challenge with the CZM in modeling damage in composites lies in determining which damage mechanism occurs at a given numerical interface based on the stress state of the structure. This challenge arises from the anisotropic nature of lamina material fracture properties, which are typically known only along specific directions such as parallel and transverse to the fiber direction. Numerical fracture properties defined at a given numerical interface, derived from these material properties, are likewise anisotropic. When a numerical interface does not align with directions where material fracture properties are known, it is not clear how to determine numerical properties and, consequently, the appropriate fracture mechanism to apply.

To date, no solution has been devised to address this limitation. Therefore, modeling damage in composite laminates has mainly relied on methods designed for isotropic materials (Shi et al. [8], Abrate et al. [9], Sun et al. [10]). However, these methods come with notable modeling constraints: they limit the arbitrariness of damage propagation and can only be employed when experimental data on fracture propagation are available.

In this thesis, a novel approach is proposed to ensure arbitrary damage development solely based on the stress state of a composite lamina thanks to the DG/CZM approach. The proposed method involves decomposing numerical interfaces, along with the opening and traction vectors acting on them, into parallel and transverse directions relative to the fiber direction of the lamina. Specifically, opening and traction components perpendicular to the virtual numerical interface aligned with the fiber direction are assumed to contribute to matrix damage along the fiber direction. Conversely, components perpendicular to the virtual numerical interface transverse to the fiber direction are assumed to contribute to simultaneous fiber and matrix damage transverse to the fiber direction. By assuming that damage virtually propagates along these virtual interfaces, where numerical fracture properties are known, and by considering the discrepancy in energy dissipation caused by the mismatch in length between the numerical interface and the virtual interface experiencing fracture, it becomes possible to model damage development along arbitrary numerical interfaces solely based on the stress state of the structure.

To evaluate the suitability of the method in capturing damage and validate its underlying assumptions, the novel damage formulation is first verified against a simple analytical model to confirm that it accurately represents damage development under controlled conditions. Subsequently, it is validated

by comparing its predictions against experimental data sourced from relevant literature. While the novel method qualitatively reproduces experimental data, achieving a quantitative match remains a challenge, warranting further investigation.

Contents

Preface i

Summary ii

Contents iv

List of Figures v

List of Tables vi

Nomenclature vii

1 Introduction 1

2 Literature Review 6
2.1 Damage Mechanisms in Composites . . . 6
2.2 Damage Modeling Techniques for Composites . . . 7
2.3 Research Question . . . 10

3 Research Methodology 11
3.1 Mathematical Framework of Novel Cohesive Zone Model Damage Formulation . . . 11
3.1.1 Standard Damage Formulation . . . 12
3.1.2 Limitations of Standard Damage Formulation in addressing Intra-laminar Damage in Composites . . . 15
3.1.3 Novel Damage Formulation . . . 17
3.2 Implementation Aspects . . . 21
3.2.1 Orthotropic Stress-Strain Equation Implementation for Bulk Material . . . 23
3.2.2 Novel Damage Formulation Implementation for Cohesive Interface Material . . . 23
3.3 Verification against Analytical Model . . . 26
3.3.1 Orthotropic Stress-Strain Equation Verification . . . 26
3.3.2 Novel Damage Formulation Verification . . . 26
3.4 Validation against Experimental Data . . . 31
3.4.1 Experimental Setup . . . 32
3.4.2 Numerical Setup . . . 35

4 Results and Discussion 38
4.1 Verification Results . . . 38
4.2 Validation Results . . . 40

5 Conclusions 46

6 Recommendations 48

Bibliography 50

A Stress-Strain Equations for Composite Lamina 50

B Classical Laminate Theory 53

C Weak Formulation of Discontinuous Galerkin Cohesive Zone Model 56

List of Figures

1.1 Example of BVID . . . 2
1.2 Isotropic Specimen with Arbitrary Mesh undergoing Fracture . . . 3
1.3 Anisotropic Lamina with Arbitrary Mesh undergoing Fracture . . . 3
1.4 Cross-ply Laminate with Structured Mesh undergoing Fracture . . . 4

2.1 BVID Damage Mechanisms . . . 7
2.2 Damage Simulation according to XFEM, PFM, and CZM . . . 8

3.1 Crack Initiation and Evolution in CZM . . . 12
3.2 Opening and Traction Definition at Cohesive Interface . . . 13
3.3 Opening and Traction Decomposition for Standard Damage Formulation . . . 14
3.4 Linear Extrinsic DG TSL for Standard Damage Formulation . . . 15
3.5 Damage in Cross-ply Laminate . . . 15
3.6 Standard Formulation for Lamina with Biased Mesh . . . 16
3.7 Standard Formulation Limitations for Lamina with Arbitrary Mesh . . . 17
3.8 Traction and Opening (Wrong) Decomposition for Novel Damage Formulation . . . 18
3.9 Traction and Opening (Correct) Decomposition for Novel Damage Formulation . . . 19
3.10 Detail of Components contributing to Opening of Virtual Interfaces . . . 20
3.11 Opening and Traction Components (Wrong) Correction based on Standard Damage Formulation . . . 21
3.12 TSL for Novel Damage Formulation . . . 22
3.13 Cohesive Fracture Toughness Adjustment based on Mismatch in Length between Numerical and Active Virtual Interface . . . 22
3.14 Damage Constitutive Update Implementation . . . 24
3.15 Opening and Traction Components for Standard and Novel Damage Implementations . . . 25
3.16 Fracture Initiation for Standard and Novel Damage Implementations . . . 27
3.17 Fracture Evolution for Standard and Novel Damage Implementations . . . 28
3.18 Mesh for Orthotropic Equation Verification . . . 28
3.19 Strain Error Convergence between FEM and CLT . . . 29
3.20 Analytical Configuration for Novel Damage Formulation Verification . . . 29
3.21 Parallel and Transverse Configurations for Novel Damage Formulation Verification . . . 31
3.22 Geometry of CT Specimens . . . 32
3.23 Experimental Crack Surfaces . . . 33
3.24 Experimental FD Curves . . . 34
3.25 Experimental COD Measurement . . . 35
3.26 Mesh and BCs of Numerical Setup for Validation . . . 37

4.1 Verification Results for Novel Damage Formulation . . . 39
4.2 Particular Verification Results unaffected by Errors in Novel Damage Formulation . . . 40
4.3 FD Results . . . 42
4.4 Crack Evolution for 90 Laminate . . . 43
4.5 Crack Evolution for 0 Laminate . . . 44
4.6 Detail of Overly Structured Mesh . . . 45

A.1 Angle Mismatch between Lamina and Laminate Reference Systems . . . 52

B.1 Laminate BCs for CLT . . . 55

List of Tables

3.1 Experimental Lamina Parameters 33

4.1 Analytical Model Interface Parameters for Novel Damage Formulation Verification . . . 38

Nomenclature

Abbreviations

Abbreviation	Definition
BC	Boundary Condition
BVID	Barely Visible Impact Damage
CG	Continuous Galerkin
CL	Cohesive Law
CLT	Classical Laminate Theory
COD	Crack-Opening Displacement
CPU	Central Processing Unit
CT	Compact Tension
CZM	Cohesive Zone Model
DG	Discontinuous Galerkin
DG/CZM	Discontinuous Galerkin Cohesive Zone Model
DOF	Degree of Freedom
FD	Force-Displacement
FE	Finite Element
FEM	Finite Element Method
PFM	Phase Field Method
PK	Piola-Kirchhoff
TSL	Traction-Separation Law
UD	Uni-Directional
XFEM	eXtended Finite Element Method

Symbols

Symbol	Definition	Unit
a	Geometrical parameter (1)	$[m]$
A	In-plane stiffness matrix	$[N\,m^{-1}]$
B	Coupling stiffness matrix	$[N\,m^{-1}]$
B	Geometrical parameter (2)	$[m]$
$\boldsymbol{b}$	Body forces vector	$[N\,m^{-3}]$
$\boldsymbol{C}$	Stiffness matrix (1)	$[Pa]$
$\boldsymbol{C}$	Stiffness tensor	$[Pa]$
$\boldsymbol{C_0}$	Stiffness matrix (2)	$[Pa]$
D	Bending stiffness matrix	$[N]$
$\boldsymbol{d}$	Displacement vector (verification model)	$[m]$
d_c	Critical displacement	$[m]$
d_e	Elastic displacement	$[m]$
d_{on}	Displacement at fracture onset	$[m]$
d_r	Displacement rate	$[m\,s^{-1}]$
E_1	Lamina longitudinal Young's modulus	$[Pa]$
E_2	Lamina transverse Young's modulus	$[Pa]$
$\boldsymbol{F}$	Load vector	$[N]$
G_{12}	Lamina in-plane shear modulus	$[Pa]$

Symbol	Definition	Unit
$G_{c_\parallel}$	Lamina mode I fracture toughness for damage parallel to fiber direction	$[J\,m^{-2}]$
$G_{c_\perp}$	Lamina mode I fracture toughness for damage transverse to fiber direction	$[J\,m^{-2}]$
G_{I_c}	Lamina mode I fracture toughness	$[J\,m^{-2}]$
$\boldsymbol{h}$	Numerical flux vector	$[Pa]$
h	Laminate thickness	$[m]$
s L	Element size	$[m]$
L_c	Finite element characteristic length	$[m]$
l_{cz}	Cohesive zone length	$[m]$
l_{ms}	Mesh size	$[m]$
$\boldsymbol{M}$	Moment per unit width vector	$[N]$
$\boldsymbol{M}_x$	Bending moment per unit width around y direction	$[N]$
$\boldsymbol{M}_y$	Bending moment per unit width around x direction	$[N]$
$\boldsymbol{M}_{xy}$	Torsional moment per unit width	$[N]$
$\boldsymbol{N}$	Load per unit width vector	$[N\,m^{-1}]$
$\boldsymbol{N}_x$	Normal load per unit width along x direction	$[N\,m^{-1}]$
$\boldsymbol{N}_y$	Normal load per unit width along y direction	$[N\,m^{-1}]$
$\boldsymbol{N}_{xy}$	Shear load per unit width	$[N\,m^{-1}]$
$\boldsymbol{n}$	Unit vector normal to numerical interface	$[-]$
$\boldsymbol{n}_\parallel$	Unit vector parallel to fiber direction	$[-]$
$\boldsymbol{n}_\perp$	Unit vector transverse to fiber direction	$[-]$
$\boldsymbol{P}$	Piola-Kirchhoff stress tensor	$[Pa]$
$\boldsymbol{Q}$	Stiffness matrix (3)	$[Pa]$
$\boldsymbol{Q_0}$	Stiffness matrix (4)	$[Pa]$
s	Numerical interface	$[-]$
$s_\parallel$	Virtual numerical interface parallel to fiber direction	$[-]$
$s_\perp$	Virtual numerical interface transverse to fiber direction	$[-]$
$\boldsymbol{t}$	Traction vector at numerical interface	$[Pa]$
$\hat{\boldsymbol{t}}$	Traction vector at Neumann boundary	$[Pa]$
$\boldsymbol{t}_{eff}$	Effective traction vector	$[Pa]$
t_{eff}	Effective traction	$[Pa]$
t_{max}	Effective traction at maximum damage extension	$[m]$
t_n	Traction component normal to numerical interface	$[Pa]$
t_τ	Traction component tangent to numerical interface	$[Pa]$
$t_\parallel$	Traction component parallel to fiber direction	$[Pa]$
$t_\perp$	Traction component transverse to fiber direction	$[Pa]$
$\boldsymbol{u}$	Displacement vector	$[m]$
$\hat{\boldsymbol{u}}$	Displacement vector at Dirichlet boundary	$[m]$
u_x	Displacement component along x axis	$[m]$
u_x	Displacement component along y axis	$[m]$
w	Geometrical parameter (3)	$[m]$
z	Position along thickness	$[m]$
$\alpha_\parallel$	Mismatch angle between numerical and parallel virtual interface	$[-]$
$\alpha_\perp$	Mismatch angle between numerical and transverse virtual interface	$[-]$
β_s	Stabilization parameter	$[-]$
Γ_d	Dirichlet boundary	$[-]$
Γ_n	Neumann boundary	$[-]$
γ	Mixed-mode coefficient	$[-]$
$\boldsymbol{\Delta}$	Opening vector at numerical interface	$[m]$
Δ_c	Critical effective opening	$[m]$

Symbol	Definition	Unit
Δ_{eff}	Effective opening	$[m]$
Δ_{max}	Effective opening at maximum damage extension	$[m]$
Δ_n	Opening component normal to numerical interface	$[m]$
Δ_{on}	Effective opening at fracture onset	$[m]$
Δ_τ	Opening component tangent to the numerical interface	$[m]$
$\Delta_\parallel$	Opening component parallel to fiber direction	$[m]$
$\Delta_\perp$	Opening component transverse to fiber direction	$[m]$
δ	Cohesive opening	$[m]$
δ_c	Critical cohesive opening	$[m]$
$\boldsymbol{\varepsilon}$	Strain tensor/vector	$[-]$
$\boldsymbol{\varepsilon}_0$	Laminate mid-plane strain vector	$[-]$
η	Friction coefficient	$[-]$
θ	Lamina fiber direction angle	$[-]$
κ	Laminate mid-plane curvature vector	$[m^{-1}]$
ν_{12}	Lamina major in-plane Poisson's ratio	$[-]$
ν_{23}	Lamina out-of-plane Poisson's ratio	$[-]$
ρ	Material density	$[kg\, m^{-3}]$
$\boldsymbol{\sigma}$	Cauchy stress tensor/vector	$[Pa]$
$\boldsymbol{\sigma}$	Traction vector (verification model)	$[Pa]$
σ_c	Cohesive fracture strength	$[Pa]$
σ_{c_I}	Cohesive fracture strength for pure mode I opening	$[Pa]$
$\sigma_{c_{II}}$	Cohesive fracture strength for pure mode II opening	$[Pa]$
$\sigma_{c_\parallel}$	Lamina fracture strength for damage parallel to fiber direction	$[Pa]$
$\sigma_{c_\perp}$	Lamina fracture strength for damage transverse to fiber direction	$[Pa]$
$\boldsymbol{\tau}$	Unit vector tangential to numerical interface	$[Pa]$
Ω	Element domain	$[-]$

1

Introduction

Composite structures have become increasingly popular for aerospace applications due to their exceptional specific properties, such as specific strength and specific stiffness (Bui and Hu [3], Shah et al. [2]). These properties enable composite structures to meet the stringent structural requirements of the aerospace sector, which demands highly strong and stiff structures while maintaining minimal weight.

However, compared to traditional aerospace metal structures, composites are more prone to sudden and potentially catastrophic damage evolution (Davies and Olsson [4]). In particular, impact damage presents significant challenges in ensuring structural integrity: impact events typically introduce loading components transverse to the laminate mid-plane. Given the low out-of-plane mechanical properties of composite laminates, impact-induced damage can easily initiate and develop (Wisnom [6], Shah et al. [2]). Moreover, the brittle nature of composites often results in minimal visual evidence of permanent indentation due to impact, making damage detection difficult (Davies and Olsson [4], Elder et al. [11], Shah et al. [2]).

When extensive internal damage occurs alongside with surface damage minimally visible with the naked eye, impact damage is referred to as Barely Visible Impact Damage (BVID) (Davies and Olsson [4]). In BVID cases, the impactor-induced dent on the surface of the laminate is typically small, on the order of just a few tenths of mm, but damage on its inner side may be widespread and inclusive of damage mechanisms like delaminations, matrix failure, and simultaneous fiber and matrix cracking ([4]), as illustrated in figure (1.1). Further, mechanical properties can be highly reduced due to BVID, with compression strength after impact being reduced by up to 70% ([4]). Given the critical nature of BVID, accurate modeling becomes crucial to ensure structural integrity and define design allowables that guarantee sufficient residual strength up to the BVID detectability threshold (Shah et al. [2]).

A common numerical technique adopted to model fracture is the Finite Element Method (FEM), which relies on discretizing the domain into sub-elements to resolve the stress state of the structure.

Modeling damage in composite laminates is inherently more challenging compared to metal structures due to their anisotropic nature: while metals exhibit isotropic material fracture properties, composites display varying material fracture properties depending on the combination of material phases undergoing damage, determining different damage mechanisms such as matrix fracture alone or simultaneous fiber and matrix cracking (Bui and Hu [3]). In isotropic structures, material fracture properties, intrinsic to the specific material, are not influenced by directionality. This results in numerical fracture properties, dependent on the damaged numerical interface where they are evaluated, that can be readily derived from material fracture properties regardless of the interface orientation relative to the real crack (see figure 1.2). Conversely, in composite laminates, lamina material fracture properties are directionally dependent and rely on the occurring damage mechanism. As these properties are typically known only along the principal directions of a lamina, it is not clear how to derive numerical fracture properties for numerical interfaces not aligned with such directions, thus restricting the possibility for numerical cracks to arise at arbitrary orientations (see figure 1.3).

As of yet, no solution has been developed to overcome this limitation. Consequently, damage in composite laminates has been primarily modeled using methods developed for isotropic materials, albeit with significant modeling limitations (Shi et al. [8], Abrate et al. [9], Sun et al. [10]). These approaches involve conducting preliminary experimental testing on the structure intended for modeling.

(a) *Hardly noticeable BVID from Laminate Outer Surface*

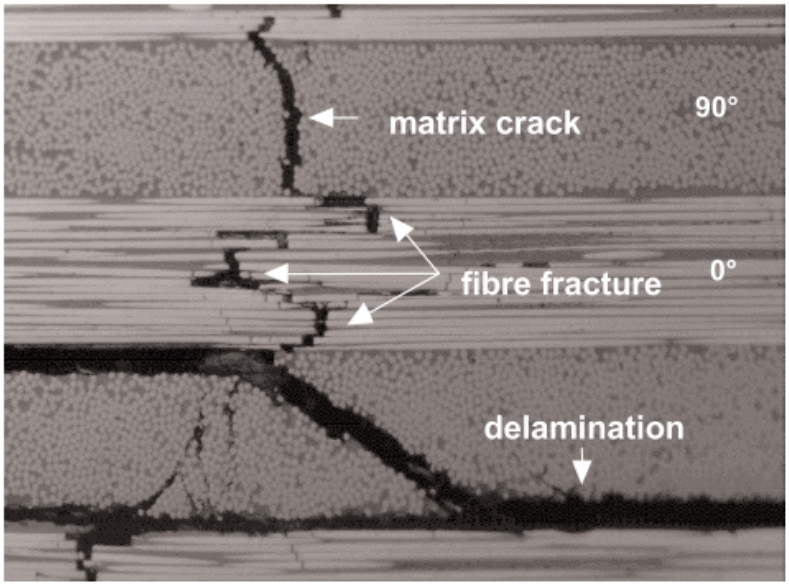

(b) *Widespread BVID on Laminate Inner Side*

Figure 1.1: *BVID refers to an impact scenario where there is minimal visible damage, in the form of a small plastic dent, on the outer surface of the laminate, while extensive damage, inclusive of delaminations, matrix failure, and fiber cracking, occurs on its inner side. Figure credits: Davies and Olsson [4].*

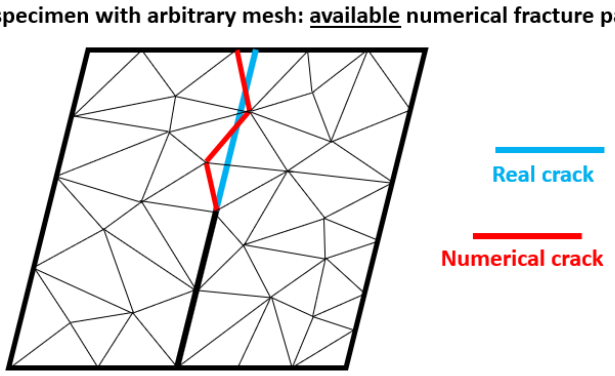

Figure 1.2: *Isotropic specimen with pre-crack undergoing fracture. The mesh boundaries of the specimen are highlighted to emphasize the discrepancy between real damage and numerical damage. In isotropic materials, where material fracture properties are the same regardless of the orientation of the real crack, numerical fracture properties can be readily derived from material fracture properties regardless any mismatch in orientation between the numerical and the real crack.*

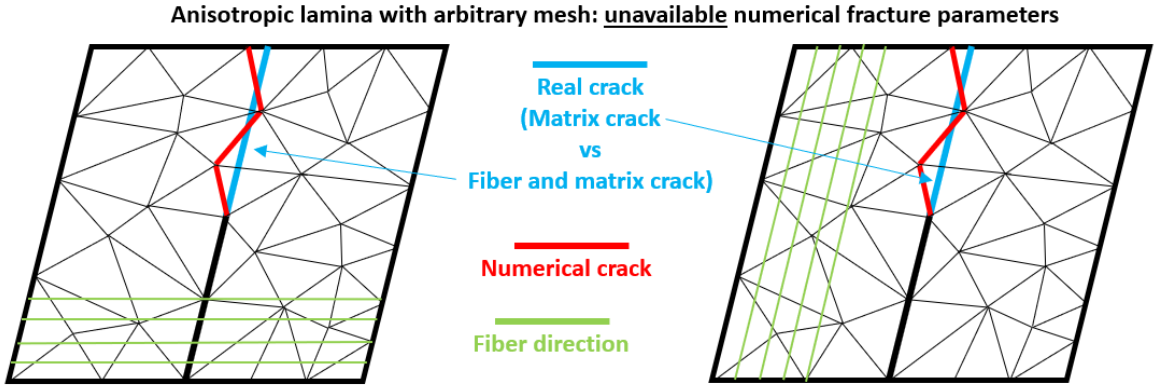

Figure 1.3: *Anisotropic laminae with pre-crack undergoing fracture. The mesh boundaries of the laminae are highlighted to illustrate the distinction between real damage and numerical damage. Due to the anisotropy of the laminae, material fracture properties vary depending on the orientation of the real crack, and are typically known only along the principal axes of the lamina, parallel and transverse to the fiber direction, as for the real cracks depicted in the two sub-figures. Consequently, numerical fracture properties derived from material fracture properties are influenced by the mismatch in orientation between the numerical crack and the real crack, and cannot be obtained when damaged numerical interfaces do not align with the real crack.*

Through these experiments, crack development is determined in advance. Subsequently, potential crack surfaces with specified numerical fracture properties are manually inserted into the numerical model at the same locations where real cracks occurred during the experiment. Following this, based on the structural stress, damage development is assumed to occur exclusively at these designated numerical interfaces, as depicted in figure (1.4). However, it is important to note that this approach introduces predetermined crack locations, limiting the arbitrariness of damage propagation. Additionally, it relies not only on the stress state of the structure but also on experimental observations, potentially limiting its applicability to scenarios where experimental data is available.

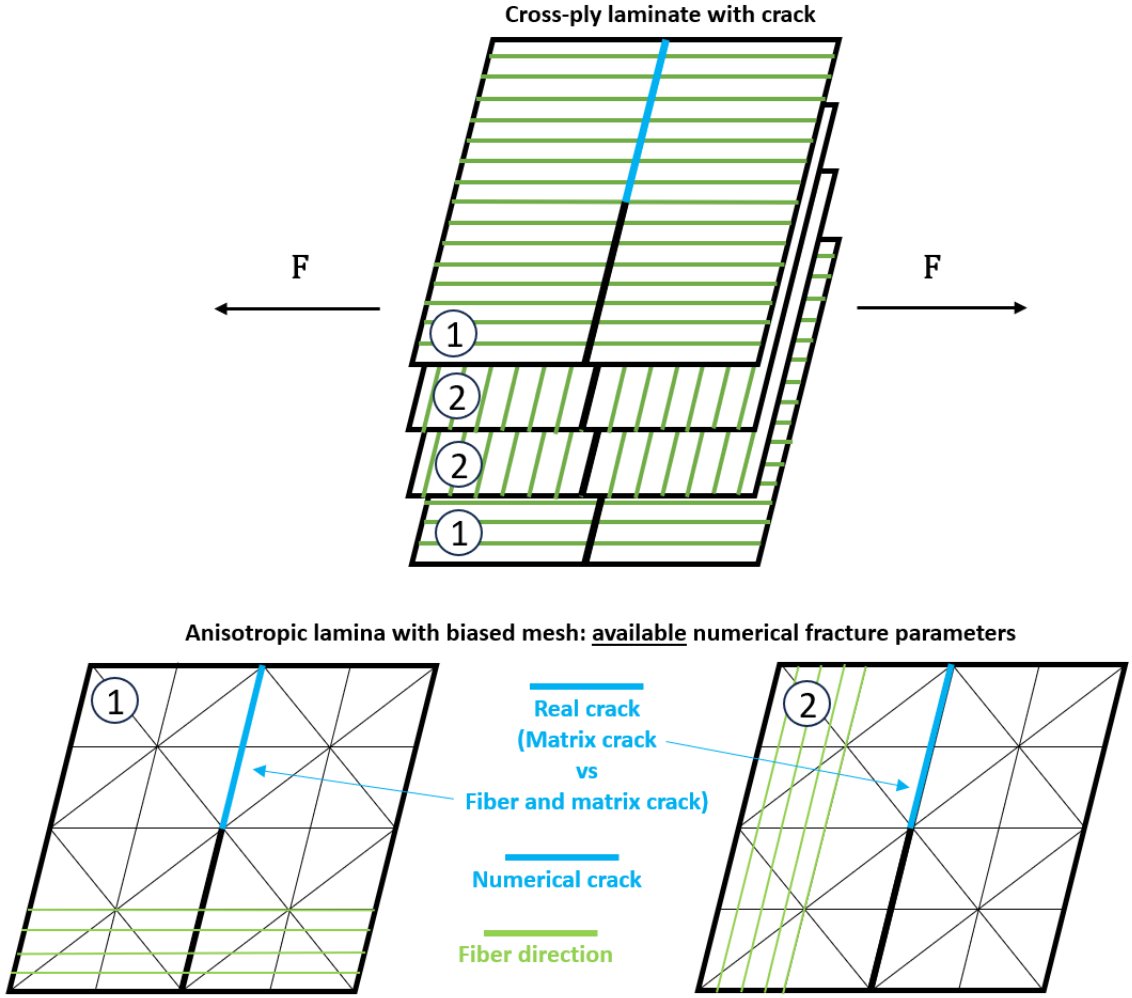

Figure 1.4: *Cross-ply laminate with pre-crack undergoing fracture due to load* ***F****. Based on experimental results, laminae marked with a "1" experience simultaneous fiber and matrix cracking, while laminae marked with a "2" experience matrix cracking only. The mesh boundaries of the laminae are highlighted to illustrate that they have been aligned with the crack paths identified in preliminary experimental tests. Numerical cracks are constrained to propagate along these input paths, allowing for the derivation of numerical fracture properties from the material fracture properties of the laminae.*

To enable accurate and physically realistic damage modeling in composites, this study proposes a novel damage formulation allowing for arbitrary crack development at any numerical interface of the mesh according to the evolving stress field of the structure. As detailed in the Literature Review chapter (2), this novel formulation is developed within a Discontinuous Galerkin Cohesive Zone Model (DG/CZM) framework implementing highly refined meshes enabled by parallel computation schemes.

The outline of the thesis is as follows. Following this Introduction chapter, the Literature Review chapter illustrates typical damage mechanisms in composites and presents modeling techniques capable of capturing them. Based on this review, gaps in the literature regarding arbitrary damage modeling in composites are highlighted, and a research question is formulated (to find a solution to fill such gaps).

The next chapter is the Research Methodology chapter, which searches for an answer to the research question by formulating, implementing, verifying and validating the novel modeling technique for arbitrary damage in composites. In the Results and Discussion chapter, the results of the novel method are presented and critically discussed, assessing the potential and the limitations of the new model. The Conclusions chapter reflects on the entire work, especially assessing the extent to which the research question was answered. Finally, the Recommendations chapter suggests potential improvements for the novel model and provides suggestions for better addressing the research question.

2

Literature Review

The focus of this Literature Review chapter is on identifying modeling techniques suitable for accurate damage simulation in composite structures. The chapter introduces typical damage mechanisms observed in composites, along with the modeling techniques commonly adopted to capture such damage mechanisms. The review highlights significant gaps in the literature regarding the modeling of arbitrary damage in composites: existing damage modeling techniques often pre-determine damage locations based on input data from experimental tests, thereby hindering spontaneous and arbitrary damage development, and limit simulations to cases where experimental data are available (Shi et al. [8], Abrate et al. [9], Sun et al. [10]). To address this limitations, the chapter formulates a research question aimed at enabling arbitrary damage simulation in composites based solely on the structural stress state. By addressing this research question, the literature review seeks to advance the current state-of-the-art in damage modeling in composites and pave the way for more realistic and predictive simulations in the field.

2.1. Damage Mechanisms in Composites

As previously mentioned in the Introduction chapter (1), damage mechanisms in composites can be related to multiple combinations of damaged material phases, determining different failure mechanisms such as matrix damage alone or simultaneous fiber and the matrix damage. The specific damage mechanism that occurs depends on the stress conditions experienced by the composite laminate. By considering composite laminate undergoing Barely Visible Impact Damage (BVID) depicted in figure (2.1), we can gain insight into damage mechanisms typical of composites:

- Plastic dent: It happens at the impact location due to compressive stresses (Tabiei and Zhang [12]);
- Oblique cracks: Matrix cracking oblique to the laminate mid-plane occurs due to out-of-plane shear stresses ([12]);
- Delaminations: Matrix cracking in between plies occurs due to in-plane shear stresses ([12]). They most likely occur in between laminae of different fiber orientations ([12]);
- Transverse cracks: Simultaneous fiber and matrix cracking transverse to the laminate mid-plane occurs due to bending stresses, often at the back of the laminate ([12]).

For damage modelling purposes, as will be further explained in the following section (2.2), the aforementioned damage mechanisms can be grouped as follows:

- Inter-laminar damage: Delaminations fall within this group, indicating damage occurring in between laminae;
- Intra-laminar damage: Oblique matrix cracking and simultaneous fiber and matrix cracking transverse to the laminate mid-plane fall within this group, indicating damage occurring inside a lamina.

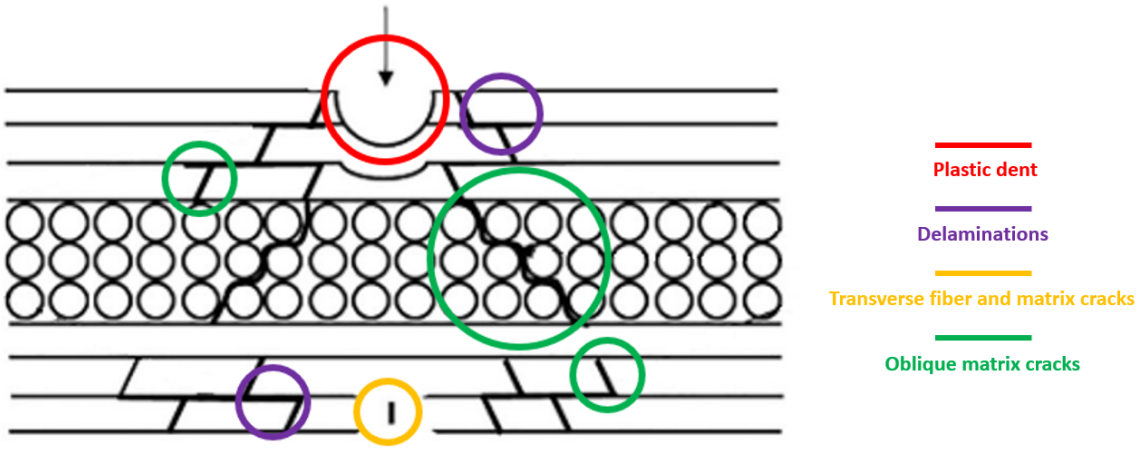

Figure 2.1: *Composite laminate cross-section illustrating damage mechanisms typically related to BVID. It is noted that the lamina with circles inside represents a lamina with fibers oriented perpendicular to the plane of the paper, while the other laminae have their fiber direction parallel to the horizontal. Figure credits: Tabiei and Zhang [12].*

2.2. Damage Modeling Techniques for Composites

When considering the modeling of damage in composite materials, analytical models may initially seem appealing due to their ability to provide exact solutions, which are generally convenient to interpret and implement. However, Faggiani and Falzon [13] argue that analytical models often fall short in accurately capturing the complex damage mechanisms inherent in composites, especially those associated with impact damage.

In contrast, numerical methods offer greater flexibility and capability in handling complex modeling scenarios such as general Boundary Conditions (BCs) and dynamic phenomena (Guo et al. [14]). Finite Element Methods (FEMs), in particular, have been widely employed to model both inter- and intra-laminar damage in composites (Faggiani and Falzon [13]).

The FEMs for damage simulation in composites can be categorized into discrete and continuum damage frameworks (Forghani et al. [15], Sun et al. [10]). In the discrete approach, damage is represented as a discontinuity in the displacement field, typically localized at mesh boundaries ([15]). Conversely, the continuum approach represents damage in a smeared sense through a damage variable defined at each point of the domain, indicating the fracture status at that specific location ([15]).

Depending on the application, it may be more convenient to adopt either the discrete or the continuum approach to model damage in composites. When damage is diffused and propagates along arbitrary directions, which is often the case for intra-laminar damage, a continuum damage model is generally implemented ([15]). In contrast, when damage is localized in specific areas, such as inter-laminar damage, a discrete damage model is largely preferred (Mukhopadhyay and Hallett [16]).

Several FEMs are commonly used for simulating damage in composite materials:

- eXtended Finite Element Method (XFEM) (Belytschko and Black [17], Moës et al. [18]): This discrete framework method extends the capabilities of traditional FEMs by enriching the FE discretization through discontinuous functions, which make damage evolution relatively independent of the underlying mesh;
- Phase Field Method (PFM) (Francfort and Marigo [19], Bourdin et al. [20], Ambrosio and Tortorelli [21], Tanné et al. [22]): It is a continuum damage model where the crack development results from the minimization of the total energy of the cracked domain. The method implements a scalar damage variable referred to as the phase-field, diffusing in the area surrounding the crack. The width of this diffusion zone is controlled through a characteristic length-scale parameter;
- Cohesive Zone Model (CZM) (Barenblatt [23] and [24], Dugdale [25], Hillerborg [26]): This discrete method is strictly related to the concept of cohesive zone, an area near the crack tip where damage is localized and cohesive forces arise to oppose to the separation of the crack surfaces. The model allows for crack propagation along internal mesh boundaries which gradually open upon reaching their cohesive fracture properties.

A depiction of a cracked domain according to the three methods is presented in figure (2.2). The illustration aims to showcase the differences in how the real crack is approximated with the numerical crack derived using the various methods.

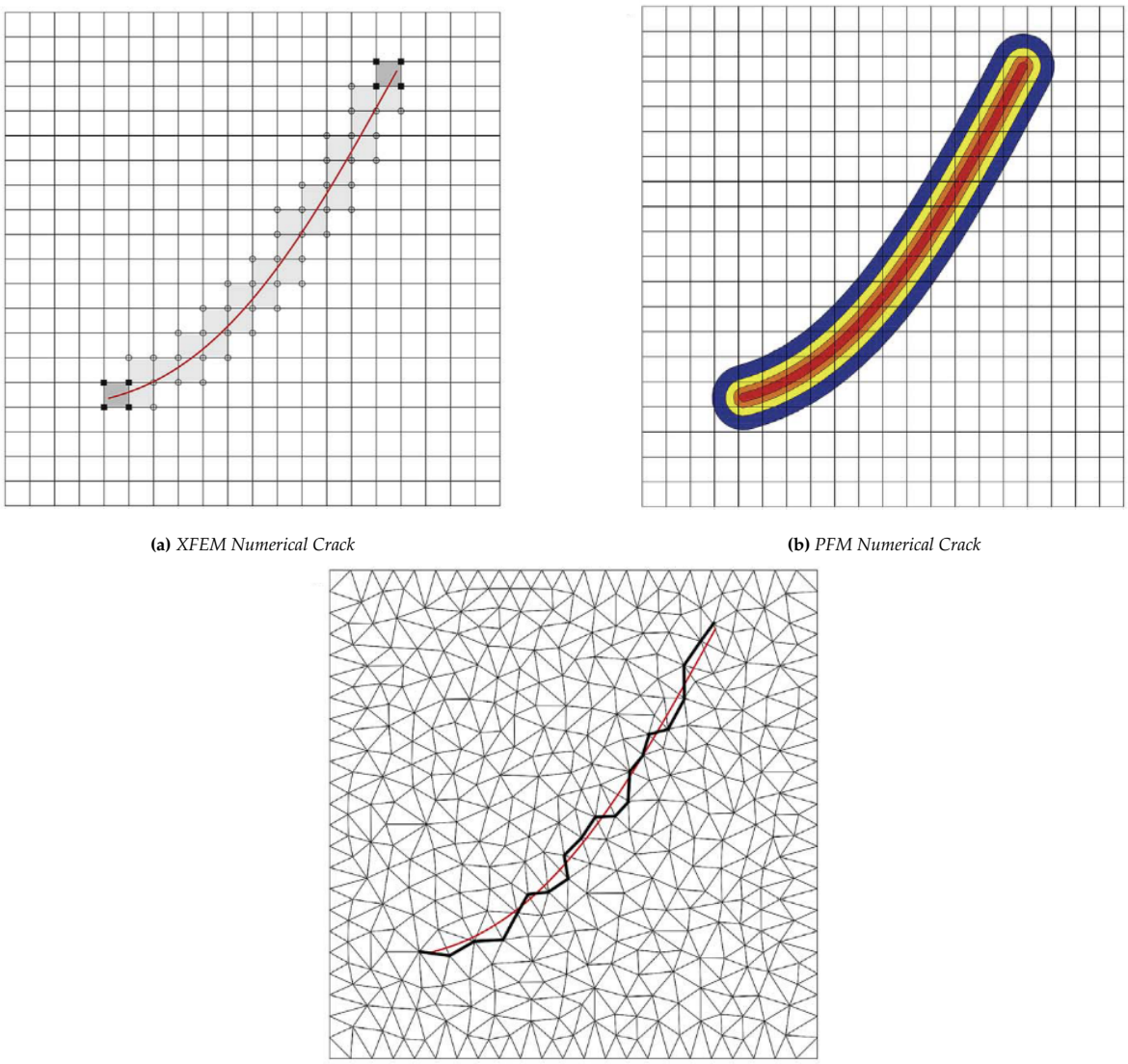

(a) *XFEM Numerical Crack*

(b) *PFM Numerical Crack*

(c) *CZM Numerical Crack*

Figure 2.2: *Differences in crack modeling among the XFEM, PFM, and CZM. The real crack is depicted in red, while the numerical crack approximates it. In the XFEM approach, enriched Degrees of Freedom (DOFs) are incorporated to model displacement discontinuities relatively independently of the underlying mesh. With the PFM, damage is represented in a smeared sense through a damage variable defined at each point of the domain. This variable assumes a value of* 1 *in the central region marked in red, where damage is fully developed, and gradually decreases towards* 0*, in white areas. Contrary to the previous methods, damage growth in the CZM is confined to mesh boundaries. Figure credits: Lecampion et al. [27].*

When considering the effectiveness of the XFEM, PFM, and CZM for modeling inter- and intra-laminar damage in composites:

- Inter-laminar damage modeling: The CZM emerges as the preferred method to model inter-laminar damage. With potential delamination areas already known beforehand, mesh boundaries can be aligned with these damage regions to facilitate the determination of numerical fracture properties (Sun et al. [10]). In contrast, employing the XFEM to capture delaminations would unnecessarily complicate the model due to the additional DOFs associated with enrichment functions. Similarly, using the PFM would add complexity to the simulation: attempting to precisely localize the continuum-based crack at delamination areas by narrowing the diffusion

zone to obtain accurate damage simulations would significantly escalate computational costs compared to employing the CZM;

- Intra-laminar damage modeling: All three methods analyzed face challenges in effectively modeling intra-laminar damage in composites:

  1. The XFEM is particularly ill-suited for this task due to several reasons. Firstly, Radovitzky et al. [5] highlight that the method has not demonstrated scalability, which is crucial for damage simulation in composites due to their complex damage patterns and 3D geometries that require high computational loads to be modeled (Bogenfeld et al. [7]). Secondly, complex damage patterns involving branching or merging, as well as 3D geometries, make the XFEM implementation cumbersome (Giovanardi [28], Bui and Hu [3]);
  2. Although the PFM shows promise in predicting complex crack paths inclusive of branching, merging, and dynamic fragmentation thanks to its solid physical formulation (Bui and Hu [3], Pillai [29]), it is not yet mature enough to effectively capture intra-laminar damage in composites because of its challenges with the material's anisotropic behavior ([3], [29]). Also, fracture behaviors are highly influenced by the length-scale diffusion parameter, and deriving this is not straightforward and necessitates accurate tuning based on experimental tests ([3], [29]);
  3. Unlike the previous methods, the CZM does not face specific scalability issues, challenges in capturing complex damage patterns, or difficulties in defining damage numerical parameters. Despite the CZM's mesh-dependent nature, its Discontinuous Galerkin Cohesive Zone Model (DG/CZM) formulation allows for relatively arbitrary damage description: the DG/CZM facilitates highly refined meshes, reducing the mesh-dependency of the CZM (Radovitzky et al. [5]). This is enabled by the DG/CZM's extrinsic damage formulation, which avoids artificial stiffness introduction in the constitutive damage law and allows cohesive damage to evolve at any internal boundary without introducing inconsistency ([5]). Moreover, the DG/CZM is highly suitable for parallel implementation, as mesh and data structures reliant on the mesh do not require redefinition upon crack propagation ([5]). This makes the DG/CZM's parallel implementation particularly advantageous for arbitrary damage modeling in composites, enabling drastic reductions in simulation times distributing the computational load among multiple processors running concurrently ([5]). Even if its inherent mesh-dependence can be alleviated, the CZM faces challenges in modeling intra-laminar damage in composites due to the material's anisotropic behavior, as outlined in the Introduction chapter (1).

In composite laminates modeling, addressing both inter- and intra-laminar damage often necessitates the use of two distinct damage models (Forghani et al. [15], Bui and Hu [3]). However, this dual-model approach inherently complicates the overall simulation, as it requires intricate coupling mechanisms between the two diverse methods ([3]). Given that the CZM emerges as the preferred method for inter-laminar damage, utilizing the CZM for modeling both inter- and intra-laminar damage can streamline the modeling process and avoid the added complexity of coupling different damage models.

Nevertheless, before fully embracing such an approach, it is paramount to address the CZM's limitation in handling the anisotropic nature of composites. This constraint pertains to the challenge of determining the specific intra-laminar fracture mechanism for cohesive interfaces not aligned with directions where the lamina material fracture properties are known. Established approaches originally developed for isotropic materials offer solutions to mitigate this limitation (Shi et al. [8], Abrate et al. [9], Sun et al. [10]). However, they come at a cost: they introduce predetermined crack locations based on experimental observations, which constrain the arbitrariness of damage propagation. Additionally, they rely not only on the structural stress state but also on experimental data, limiting the applicability of these approaches to scenarios where such data is available.

By adopting a unified CZM-based approach, the simulation complexity is notably reduced while still facilitating accurate damage modeling in composites. Nonetheless, the acknowledgment and mitigation of the CZM's limitation regarding anisotropy are imperative for ensuring the efficacy of this approach.

2.3. Research Question

In summary, this literature review highlights that the CZM is a promising method for capturing damage in composite laminates. Among the advantages of the method:

- Robustness: The CZM numerical parameters can be readily derived from experimental results. Also, the method is able to model complex damage scenarios typical of composites inclusive of branching, merging, and fragmentation;
- Scalability: The CZM is suitable for parallel implementation, which is crucial for damage simulation in composites due to its high computational load. Especially, the DG/CZM facilitate this task by avoiding the mesh redefinition upon fracture.

However, the review identifies a major gap in the literature concerning the CZM's limitation in accurately modeling arbitrary intra-laminar damage in composites, specifically in determining the damage mechanism occurring at a numerical interface solely based on the stress state of the structure.

Based on this gap, the main research question is formulated as follows:

How can a novel CZM-based damage formulation be developed to facilitate arbitrary intra-laminar damage development by distinguishing between damage mechanisms based on the stress state of the laminate?

3

Research Methodology

The Research Methodology chapter illustrates how to address the research question outlined in the Literature Review chapter (2) by implementing a novel Cohesive Zone Model (CZM) damage formulation capable of allowing for arbitrary intra-laminar damage in composites based solely on the evolving stress state of the structure.

The novel damage formulation is derived from an established damage formulation enabling arbitrary damage in isotropic materials. The novel method considers an alternative decomposition of both opening and traction at a numerical interface into components parallel and transverse to the fiber direction of the lamina. The method assumes potential intra-laminar damage mechanisms to be decoupled, with the parallel traction component assumed to contribute to simultaneous fiber and matrix cracking of the numerical interface once it reaches the lamina material strength in the direction parallel to the fibers, while the transverse traction component is assumed to contribute to matrix cracking of the interface once it reaches the lamina material strength in the direction transverse to the fibers. Additionally, the method assumes that the two damage mechanisms cannot occur simultaneously.

The structure of this chapter is as follows: First, the chapter discusses the mathematical framework behind the novel CZM damage formulation (section 3.1). Subsequently, it details the implementation of the novel formulation in Summit-lite, a Finite Element (FE) object-oriented research code (section 3.2). To ensure the correctness of the implementation under controlled conditions, the novel method is verified against a simple analytical model (section 3.3). Once verified, the novel CZM formulation is validated against experimental data sourced from relevant literature (section 3.4).

3.1. Mathematical Framework of Novel Cohesive Zone Model Damage Formulation

This section presents the mathematical framework underlying the novel CZM damage formulation. The novelty of the proposed method lies in its constitutive law governing damage at the mesh internal boundaries. Classical CZM damage constitutive laws, developed for isotropic materials, are inadequate for addressing damage in composites. Specifically, this limit concerns the activation of different intra-laminar damage mechanisms depending on the stress state of the laminate. Established approaches, such as the one proposed by Sun et al. [10], offer solutions to mitigate this limitation. However, these approaches introduce predetermined crack locations based on experimental observations, which constrain the arbitrariness of damage propagation. Additionally, they rely not only on the stress state of the numerical model but also on experimental data. The novel CZM damage constitutive law is derived in this section to address these limitations.

First, the section introduces a CZM damage constitutive law popular in the literature, here referred to as the standard damage formulation. Then, the section discusses the shortcomings of the standard formulation in adequately representing arbitrary intra-laminar damage in composites. Finally, based on the standard damage constitutive law, the section proposes a novel damage constitutive law to overcome these limitations.

3.1.1. Standard Damage Formulation

The Traction-Separation Law (TSL), or Cohesive Law (CL), serves as the constitutive law governing damage in the CZM. As illustrated in figure (3.1), the TSL relates the opening of two crack surfaces at the crack tip to the reaction forces that keep such surfaces together. When the stress at the crack tip reaches the cohesive strength, the crack surfaces start to open, leading to a reduction in traction. Upon reaching zero traction at the crack tip, the crack surfaces fully separate, allowing the crack tip to advance.

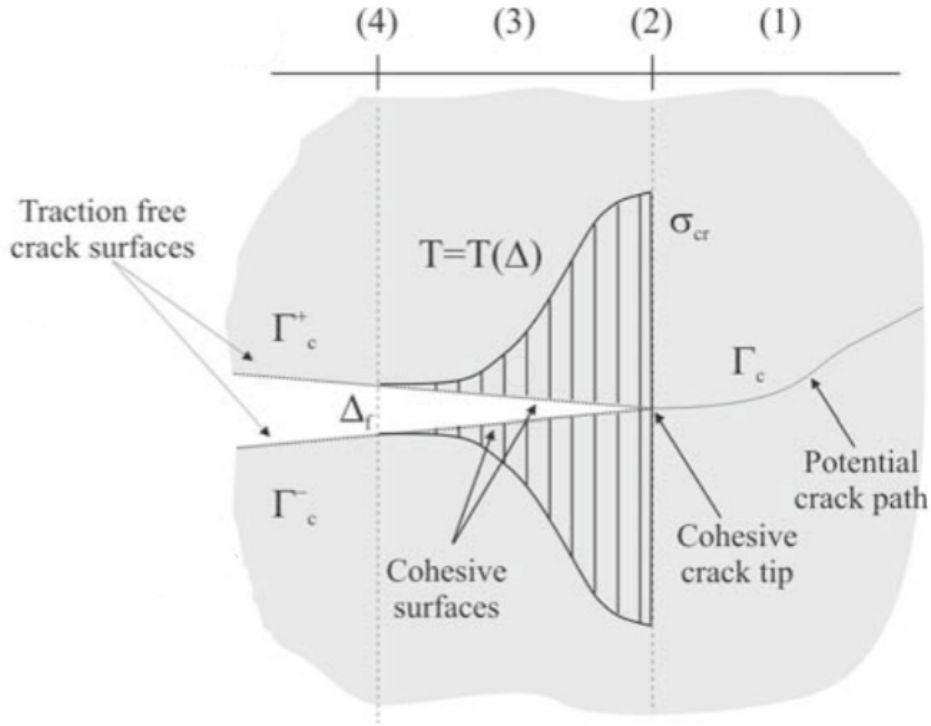

Figure 3.1: *Crack initiation and evolution according to the CZM proceeds as follows: In region (1), the traction T is lower than the cohesive strength σ_{cr}, and damage does not initiate. At section (2), when $T = \sigma_{cr}$, damage initiates. As damage evolves in region (3), the traction at the two cohesive interfaces Γ_c^+ and Γ_c^+ starts to decrease, while the opening Δ increases. Upon reaching section (4), when $\Delta = \Delta_f$, damage is fully developed, rendering the two cohesive surfaces incapable of stress transfer. At this point, the crack tip advances. Figure credits: Alfano et al. [30].*

Next, the TSL derived by Ortiz and Pandolfi [31] is presented. As this formulation is widely adopted in the literature, it is here referred to as the standard TSL. To introduce the standard TSL, let's determine the opening $\boldsymbol{\Delta}$ and the traction $\boldsymbol{t}$ at a point P lying on the cohesive interface s between two FEs Ω_- and Ω_+, as illustrated in figure (3.2). The opening $\boldsymbol{\Delta}$ is defined as the difference in displacement $\boldsymbol{u}$ between the Ω^+ and the Ω^- elements:

$$\begin{aligned} \boldsymbol{\Delta}^- &= \boldsymbol{u}^+ - \boldsymbol{u}^- \\ \boldsymbol{\Delta}^+ &= \boldsymbol{u}^- - \boldsymbol{u}^+ \end{aligned} \tag{3.1}$$

The displacement $\boldsymbol{u}$ is derived by solving the weak formulation of equilibrium of the linear momentum, detailed in the appendix chapter (C) for the Discontinuous Galerkin Cohesive Zone Model (DG/CZM). The traction at the elements interface is defined as

$$\begin{aligned} \boldsymbol{t}^- &= \boldsymbol{P}^- \boldsymbol{n}^- \\ \boldsymbol{t}^+ &= \boldsymbol{P}^+ \boldsymbol{n}^+ \end{aligned} \tag{3.2}$$

where $\boldsymbol{P}$ is the Piola-Kirchhoff (PK) stress tensor, and $\boldsymbol{n}$ is the unit vector normal to the interface of the Ω element in the deformed configuration, defined so that it points outward to the FE region. Assuming small deformations, the actual configuration can be approximated with the reference configuration,

meaning that the PK stress tensor can be approximated with the Cauchy stress tensor σ, and the unit normal vector in the deformed configuration with the one in the reference configuration:

$$\boldsymbol{P} = \boldsymbol{\sigma} \tag{3.3}$$

Additionally, by imposing the linear elastic material assumption, σ is determined as a linear function of $\boldsymbol{u}$, as derived in equation (C.2).

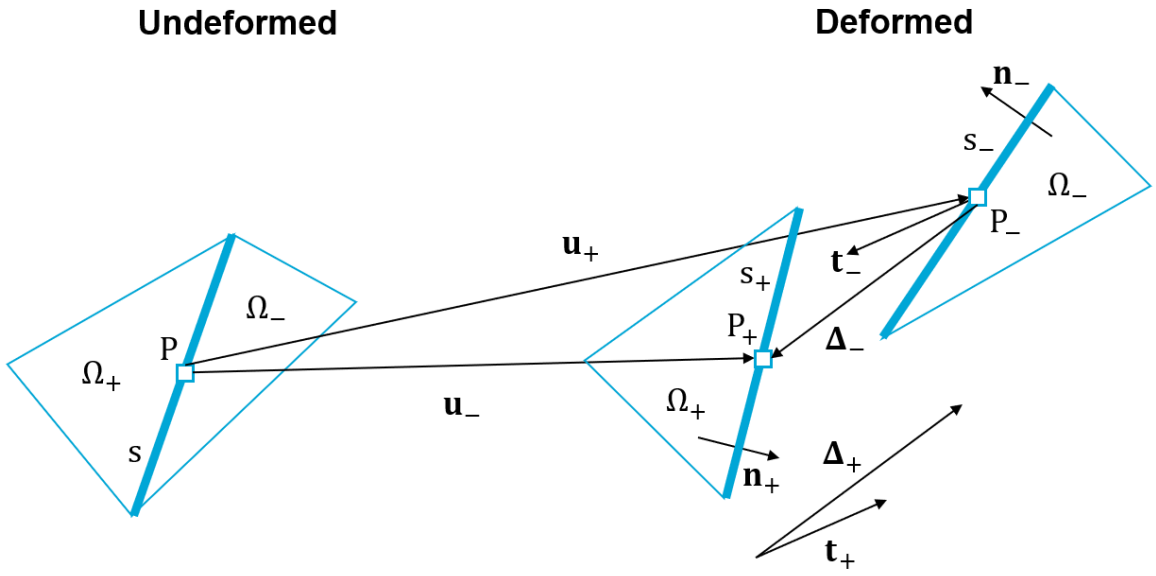

Figure 3.2: *Definition of the opening* $\boldsymbol{\Delta}$ *and the traction* $\boldsymbol{t}$ *at a point P on the cohesive interface s between two FEs* Ω_+ *and* Ω_-. $\boldsymbol{\Delta}$ *is defined as the difference in displacement* $\boldsymbol{u}$ *between points* P^+ *and* P^-. *The unit vector* $\boldsymbol{n}$ *is defined as the normal to the numerical interface in the deformed configuration and points outward to the FE region. Note that vectors* $\boldsymbol{\Delta}^+$ *and* $\boldsymbol{t}^+$ *are evaluated at point* P^+ *and are opposite in direction to* $\boldsymbol{\Delta}^-$ *and* $\boldsymbol{t}^-$.

Once $\boldsymbol{\Delta}$ and $\boldsymbol{t}$ have been determined, Ortiz and Pandolfi [31] decompose them along the unit vectors normal and tangential to the cohesive interface $\boldsymbol{n}$ and $\boldsymbol{\tau}$:

$$\begin{aligned} \Delta_n &= \boldsymbol{\Delta} \cdot \boldsymbol{n} \\ \Delta_\tau &= \boldsymbol{\Delta} \cdot \boldsymbol{\tau} \end{aligned} \tag{3.4}$$

$$\begin{aligned} t_n &= \boldsymbol{t} \cdot \boldsymbol{n} \\ t_\tau &= \boldsymbol{t} \cdot \boldsymbol{\tau} \end{aligned} \tag{3.5}$$

The normal components Δ_n and t_n are related to mode I opening, while the tangential components Δ_τ and t_τ are related to mode II opening. The components are illustrated in figure (3.3).

Based on the normal and tangent components, the effective values for the opening and the traction are obtained (Wu et al. [32]) as

$$\Delta_{eff} = \sqrt{\langle\langle \Delta_n \rangle\rangle^2 + \gamma^2 (\Delta_\tau)^2} \tag{3.6}$$

and

$$t_{eff} = \begin{cases} \sqrt{t_n^2 + \frac{1}{\gamma^2} t_\tau^2}, & t_n \geq 0 \\ \frac{1}{\gamma} \langle\langle |t_\tau| - \eta |t_n| \rangle\rangle, & t_n < 0 \end{cases} \tag{3.7}$$

In equations (3.7) and (3.6), the normal and tangential components contribute with different weights to the values of Δ_{eff} and t_{eff}. The weight is determined by the parameter $\gamma = \sigma_{c_{II}} / \sigma_{c_I}$, representing the ratio of the cohesive strengths in pure mode II and in pure mode I. η denotes the friction coefficient, introduced in case of compressive stresses $t_n < 0$. The operator $\langle\langle \cdot \rangle\rangle$ returns its argument when this is positive, and 0 otherwise.

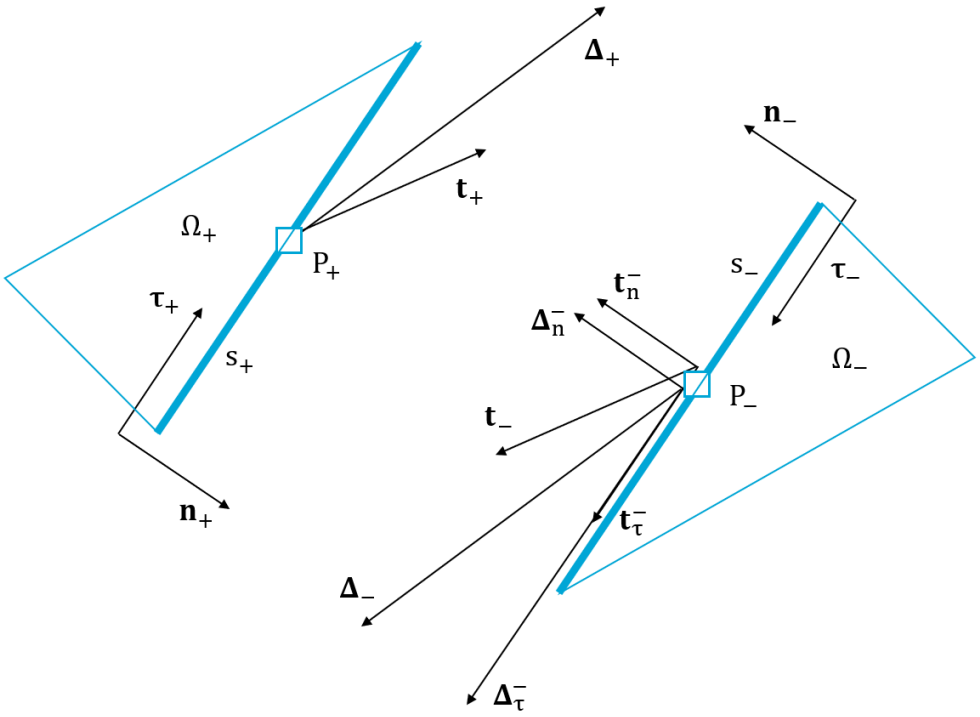

Figure 3.3: *Decomposition of opening $\boldsymbol{\Delta}_-$ and traction $\boldsymbol{t}_-$ of the Ω_- element along the unit vectors $\boldsymbol{n}_-$ and $\boldsymbol{\tau}_-$ normal and tangent to the cohesive interface s_-.*

Fracture initiation occurs as soon as t_{eff} reaches the cohesive strength σ_c of the numerical interface:

$$t_{eff} \geq \sigma_c \tag{3.8}$$

where σ_c can be assumed for simplicity to be equal to the highest value between σ_{c_I} and $\sigma_{c_{II}}$ when $t_n \geq 0$, and equal to $\sigma_{c_{II}}$ when $t_n < 0$. t_{eff} can be related to Δ_{eff} according to the linear extrinsic CL depicted in figure (3.4), which considers an irreversible softening phase during opening and a reversible phase during unloading:

$$t_{eff} = \begin{cases} \sigma_c\left(1 - \frac{\Delta_{eff}}{\Delta_c}\right), & \text{softening} \\ t_{max}\frac{\Delta_{eff}}{\Delta_{max}}, & \text{unloading} \end{cases} \tag{3.9}$$

where Δ_{max} and t_{max} are the opening and traction reached at maximum damage extension upon irreversible softening, and Δ_c is the critical opening defined as

$$\Delta_c = \frac{2G_c}{\sigma_c} \tag{3.10}$$

where G_c is the cohesive toughness. Equation (3.10) can be easily obtained through geometrical considerations on the linear TSL defined in figure (3.4). It is important to emphasize that, in case of a Discontinuous Galerkin (DG) formulation, Δ_{eff} has to be re-scaled so that its value is 0 at fracture onset. This rescaling guarantees that the traction at $\Delta_{eff} = 0$ corresponds to the cohesive strength:

$$\begin{aligned} \Delta'_{eff} &= \Delta_{eff} - \Delta_{on} \\ t_{eff}(\Delta'_{eff} = 0) &= \sigma_c \end{aligned} \tag{3.11}$$

Based on t_{eff}, the effective traction vector $\boldsymbol{t}_{eff}$ is defined as

$$\boldsymbol{t}_{eff} = \begin{cases} t_{eff}\left(\frac{\Delta_n}{\Delta_{eff}}\boldsymbol{n} + \gamma\frac{\Delta_\tau}{\Delta_{eff}}\boldsymbol{\tau}\right), & t_n \geq 0 \\ t_{eff}\gamma\frac{\Delta_\tau}{\Delta_{eff}}\boldsymbol{\tau}, & t_n < 0 \end{cases} \tag{3.12}$$

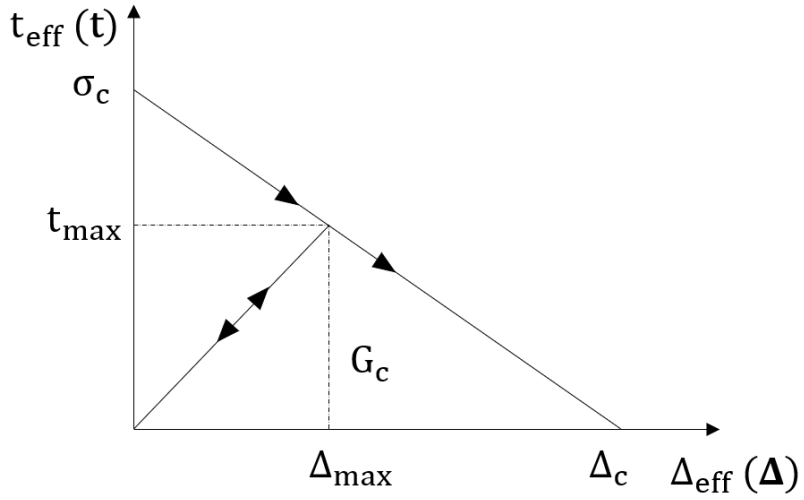

Figure 3.4: *Linear extrinsic TSL describing damage initiation and propagation within the DG/CZM framework. When the effective traction t_{eff} reaches the cohesive strength σ_c, irreversible damage starts to form. Upon reaching final failure of the numerical interface at the critical opening Δ_c, the amount of cohesive energy release rate gets equal to the cohesive toughness G_c. In case where, after damage onset and before complete failure, unloading occurs, t_{eff} decreases reversibly from the point of maximum damage extension (Δ_{max}, t_{max}) to 0. If reloading occurs after this unloading, the effective opening Δ_{eff} must reversibly return to Δ_{max} before further irreversible damage occurs. The irreversible path is indicated by an arrow pointing in the direction of increasing Δ_{eff}, while the reversible path is marked by arrows pointing in both directions.*

3.1.2. Limitations of Standard Damage Formulation in addressing Intra-laminar Damage in Composites

Expanding on the discussion of the Introduction chapter (1), this sub-section elucidates why the standard damage formulation proves inadequate for modeling arbitrary damage in composite laminates. The primary reason of this unsuitability stems from the anisotropic nature of composites: given a cohesive interface oriented at an arbitrary angle relative to lamina directions where material fracture properties are known, it becomes unclear how to define the cohesive fracture parameters for such interface based solely on the structural stress state.

To highlight these limitations of the standard TSL, let's revisit the case of the cross-ply laminate with a pre-crack under fracture, which was previously introduced in the Introduction chapter (1) and depicted in figure (3.5). The figure illustrates a cross-ply laminate containing a pre-existing crack,

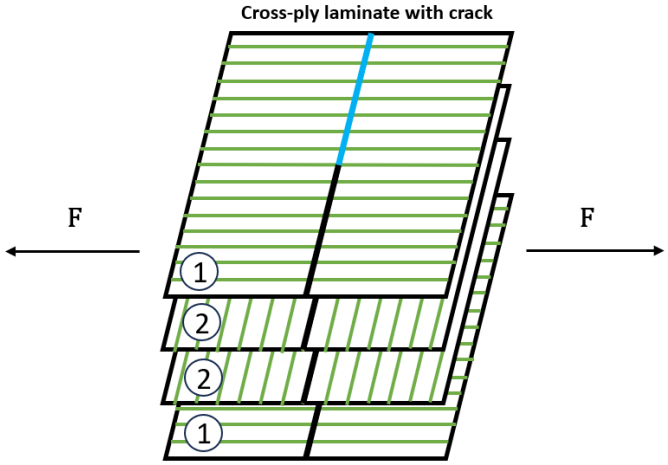

Figure 3.5: *Cross-ply laminate subjected to load. A pre-crack, depicted in black, is introduced into the laminate. Under the influence of the applied tensile load **F**, damage, shown in light blue, propagates along the pre-crack direction. The fiber angle of the plies, indicated in green, is either 90° when fibers are transverse to **F**, or 0° when fibers are parallel to **F**.*

subjected to a tensile load inducing crack propagation parallel to the pre-existing crack direction. Directing attention to the mesh solution for the cross-ply laminate shown in figure (3.6), where mesh boundaries of the 90° and 0° plies align with the expected crack path, and cohesive interfaces are exclusively placed at mesh boundaries coinciding with these expected crack paths. This arrangement facilitates numerical crack development along the crack direction determined from experimental data. Consequently, for a 90° lamina, a numerical crack parallel to the fiber direction occurs. Here, the cohesive fracture properties of the numerical interface σ_c and G_c are set equal to lamina tensile fracture properties for matrix cracking $\sigma_{c_\parallel}$ and $G_{c_\parallel}$. Conversely, for a 0° lamina, a numerical crack transverse to the fibers occurs. In this instance, the cohesive fracture properties are set equal to lamina tensile fracture properties for simultaneous fiber and matrix cracking $\sigma_{c_\perp}$ and $G_{c_\perp}$. The resulting TSLs for the 90° and the 0° laminae are depicted in figure (3.6). Essentially, this method represents a classic

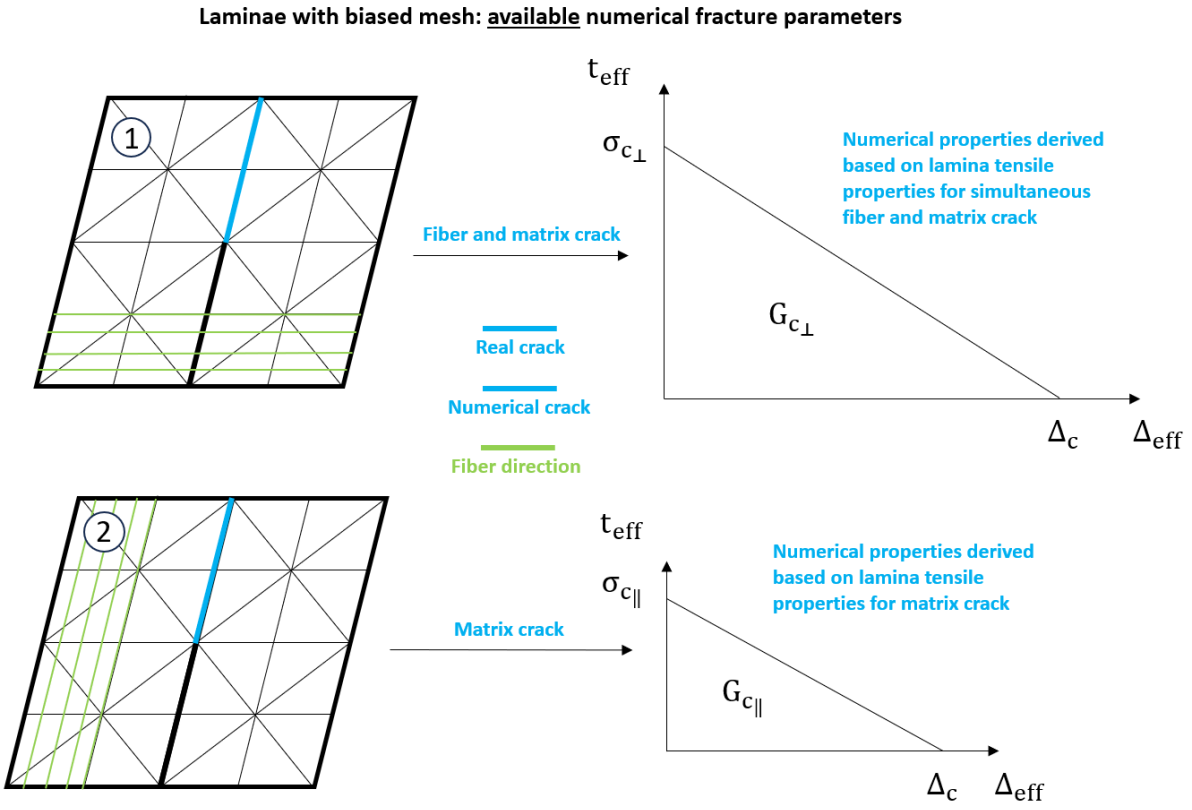

Figure 3.6: *Laminae of the cross-ply laminate with mesh boundaries aligned with the expected crack, and cohesive interfaces placed only at mesh boundaries where damage is expected based on preliminary experimental observations. Consequently, numerical damage coincides with expected damage, both depicted in light blue here. Since numerical damage is only allowed to form along the directions where lamina material fracture properties are known, cohesive fracture properties σ_c and G_c of the cohesive interfaces can be determined from the material fracture properties. Specifically, we can set cohesive fracture properties equal to lamina tensile fracture properties for matrix cracking $\sigma_{c_\parallel}$ and $G_{c_\parallel}$ for numerical damage parallel to the fiber direction, and lamina tensile fracture properties for simultaneous fiber and matrix cracking $\sigma_{c_\perp}$ and $G_{c_\perp}$ for numerical damage transverse to the fiber direction.*

CZM damage formulation developed for isotropic materials but commonly utilized in the literature to model intra-laminar damage. The approach restricts numerical damage development to predetermined directions established through preliminary experimental testing on the structure intended for modeling. Through these experiments, crack development, including both location and fracture mechanism, is determined. Subsequently, potential crack surfaces with specified numerical fracture properties are manually inserted into the numerical model at the same locations where real cracks occurred during the experiment.

Now, let's consider the alternative damage formulation presented in figure (3.7) characterized by a different meshing strategy. Here, the mesh of the 90° and 0° laminae is assumed to be entirely arbitrary and in general not aligned with the crack path observed in experimental data. In this scenario, cohesive interfaces are placed at every mesh boundary, and numerical cracks are free to develop at any mesh

boundary. Consequently, numerical damage is not bound to propagate along directions where lamina material fracture properties are known, as was the case previously. This variability in the numerical crack orientation relative to the directions along which lamina fracture parameters are known implies that the cohesive fracture properties of the cohesive interface cannot be always determined from the lamina fracture properties, as indicated by the undefined TSL in figure (3.7).

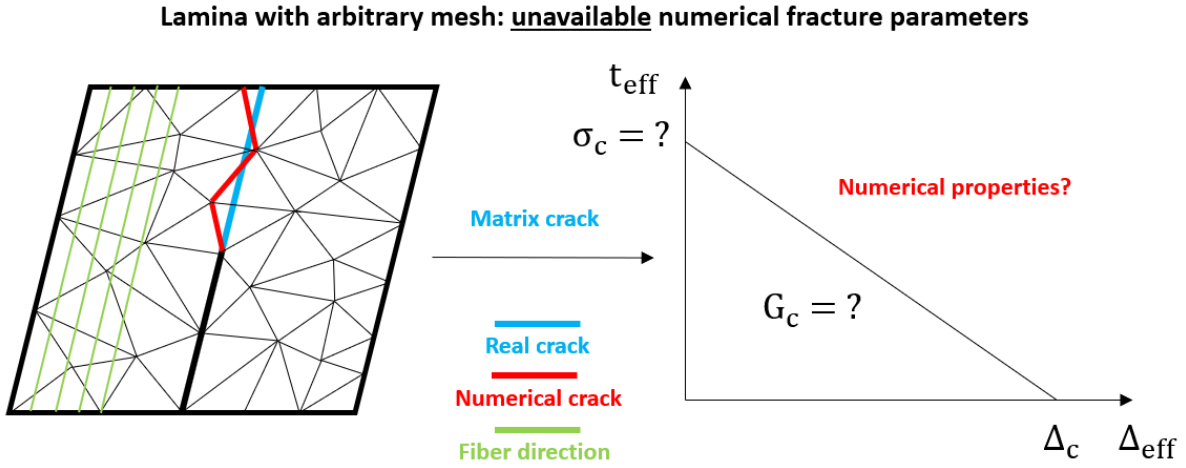

Figure 3.7: *Laminae of the cross-ply laminate with mesh boundaries not required to coincide with the expected crack. Cohesive interfaces are placed at every mesh boundary, allowing numerical damage to arise according to the stress state of the laminate. Consequently, numerical damage, depicted in red, is not constrained to coincide with expected damage, depicted in light blue. Since numerical damage can form anywhere, not only along the directions where lamina material fracture properties are known, the cohesive fracture properties σ_c and G_c of the cohesive interfaces cannot always be determined from lamina material fracture properties.*

3.1.3. Novel Damage Formulation

As the standard TSL developed for isotropic materials is incapable of modelling arbitrary damage in composite laminates, this sub-section proposes an adaptation of the standard TSL to address this limitation.

Instead of decomposing the traction and the opening into normal and a tangential components to the numerical interface, as done in the standard case, it is proposed to decompose them into parallel and transverse components to the fiber direction of the lamina. Under this framework, if the transverse traction reaches the lamina material strength for matrix cracking parallel to the fiber direction, the parallel virtual interface opens. Conversely, if the parallel traction reaches the lamina material strength for simultaneous fiber and matrix cracking transverse to the fiber direction, the transverse virtual interface opens. It is assumed that only one damage mechanism can be activated for a given numerical interface, which is either matrix cracking along the parallel virtual interface, or simultaneous fiber and matrix cracking along the transverse virtual interface. The proposed approach allows the numerical fracture properties of an arbitrary cohesive interface not aligned with directions where lamina material fracture properties are known to be related to the lamina material fracture properties.

Let's delve into a more detailed analysis of the proposed damage formulation and identify all its underlying assumptions and limitations. The opening and traction components according to the novel formulation are as follows:

$$\begin{aligned} \Delta_{\parallel} &= \boldsymbol{\Delta} \cdot \boldsymbol{n}_{\parallel} \\ \Delta_{\perp} &= \boldsymbol{\Delta} \cdot \boldsymbol{n}_{\perp} \end{aligned} \tag{3.13}$$

$$\begin{aligned} t_{\parallel} &= \boldsymbol{t} \cdot \boldsymbol{n}_{\parallel} \\ t_{\perp} &= \boldsymbol{t} \cdot \boldsymbol{n}_{\perp} \end{aligned} \tag{3.14}$$

where $\boldsymbol{n}_{\parallel}$ and $\boldsymbol{n}_{\perp}$ represent the unit vectors parallel and transverse to the fiber direction, and are determined purely based on the fiber angle θ. The proposed decomposition can be observed in figure (3.8). Upon closer inspection of the decomposition, it was realized that the $\boldsymbol{n}_{\parallel}$ and $\boldsymbol{n}_{\perp}$ vectors were

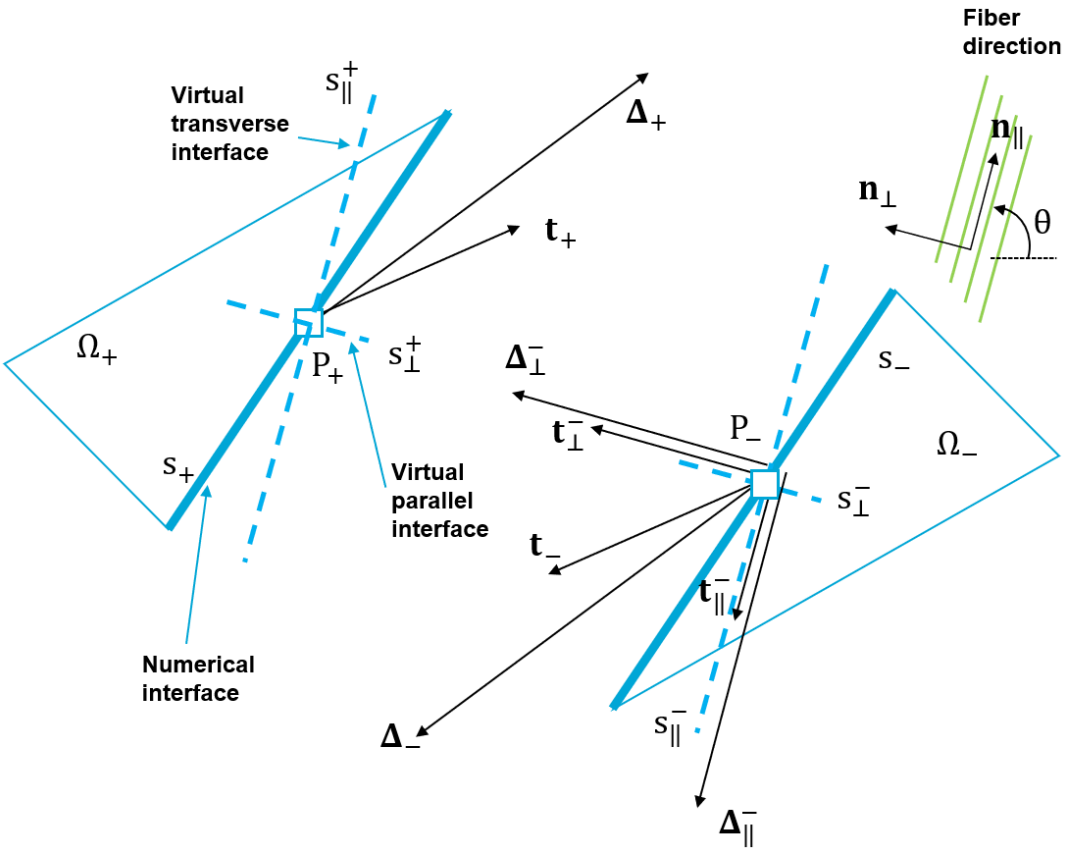

Figure 3.8: *(Wrong) Decomposition of the traction and the opening according to the novel damage formulation. The traction $\boldsymbol{t}_-$ and the opening $\boldsymbol{\Delta}_-$ of the Ω_- element are decomposed along the unit vectors parallel and transverse to the fiber direction $\boldsymbol{n}_{\parallel}$ and $\boldsymbol{n}_{\perp}$. These vectors are determined based on the fiber orientation θ of the lamina. The arbitrary numerical interface is decomposed into virtual interfaces parallel and transverse to the fiber direction $s_{\parallel}$ and $s_{\perp}$.*

defined improperly. Two sets of the two vectors needed to be defined, one for the Ω_- and one for the Ω_+ element ($\boldsymbol{n}_{\parallel}^{+}$ and $\boldsymbol{n}_{\perp}^{+}$, and $\boldsymbol{n}_{\parallel}^{-}$ and $\boldsymbol{n}_{\perp}^{-}$) in a way that they pointed outward to the respective FE's region. The adjusted decomposition, which could not be implemented due to time constraints, can be observed in figure (3.9).

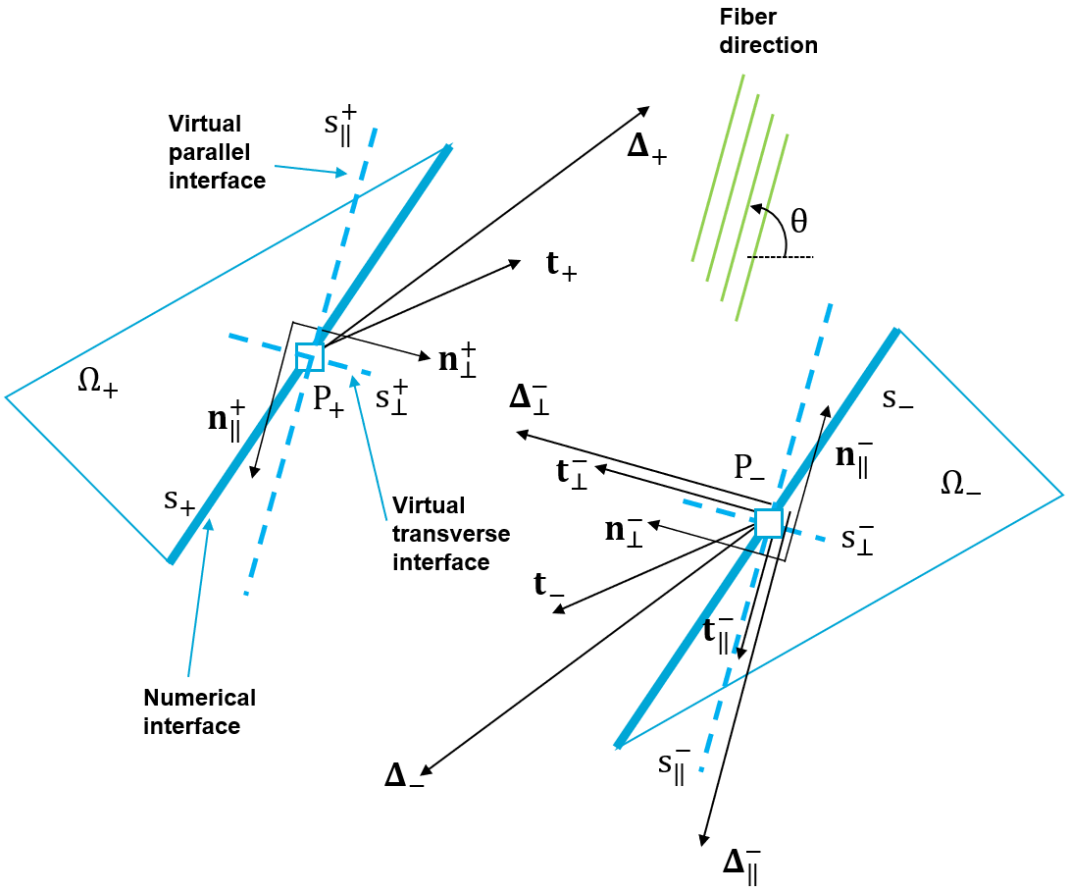

Figure 3.9: *(Correct) Decomposition of the traction and the opening according to the novel damage formulation. Compared to the decomposition shown in figure (3.8), a set of $\boldsymbol{n}_{\parallel}$ and $\boldsymbol{n}_{\perp}$ vectors is defined per each element Ω, so that both vectors point outwards to the FEs' region.*

Considering the proposed (wrong) decomposition, it is assumed that the parallel traction $t_{\parallel}$ contributes to the parallel opening $\Delta_{\parallel}$ of the transverse virtual interface $s_{\perp}$, while the transverse traction $t_{\perp}$ contributes to the transverse opening $\Delta_{\perp}$ of the parallel virtual interface $s_{\parallel}$. This implies that both virtual interfaces are assumed to open in pure mode I, with no contribution from mode II. Figure (3.10) illustrates more clearly which traction and opening components are associated with the parallel and virtual interfaces.

Another assumption is that the sign of the components in the standard damage formulation controls the sign of the parallel and transverse components in the novel formulation. However, right when the error in vectors $\boldsymbol{n}_{\parallel}$ and $\boldsymbol{n}_{\perp}$ was discovered, it was realized that this assumption was incorrect, and that this adjustment was justified by the improper assumptions for the vectors $\boldsymbol{n}_{\parallel}$ and $\boldsymbol{n}_{\perp}$ that did not necessarily point outwards to the FEs' region. Nevertheless, due to a lack of time to implement the latest improvement, the improper sign adjustment was implemented, and the opening and traction components were re-defined as

$$\Delta_{\parallel/\perp} = \begin{cases} |\Delta_{\parallel/\perp}|, & \Delta_n \geq 0 \\ -|\Delta_{\parallel/\perp}|, & \Delta_n < 0 \end{cases} \tag{3.15}$$

and

$$t_{\parallel/\perp} = \begin{cases} |t_{\parallel/\perp}|, & t_n \geq 0 \\ -|t_{\parallel/\perp}|, & t_n < 0 \end{cases} \tag{3.16}$$

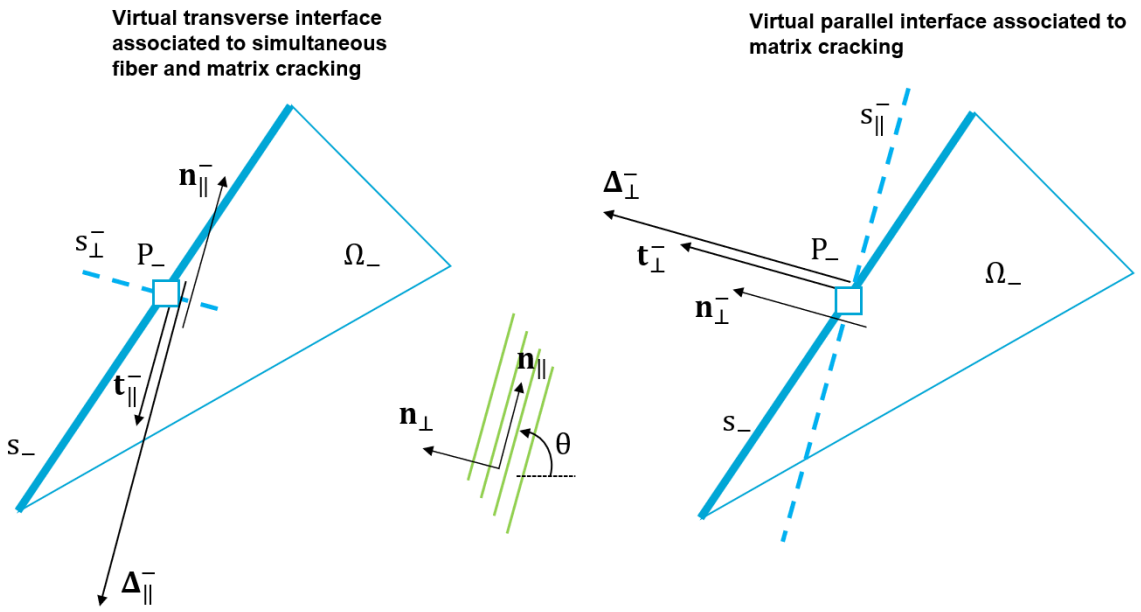

Figure 3.10: *The opening of virtual interfaces is assumed to be caused by mode I components transverse to them. Focusing on the Ω_- element, it is assumed that the parallel traction $t_{\parallel}^{-}$ contributes to the parallel opening $\Delta_{\parallel}^{-}$ of the transverse virtual interface $s_{\perp}^{-}$, while the transverse traction $t_{\perp}^{-}$ contributes to the transverse opening $\Delta_{\perp}^{-}$ of the parallel virtual interface $s_{\parallel}^{-}$. Note that the figure is based on the adjusted decomposition of figure (3.9), but what is stated above is still valid for the original decomposition of figure (3.8).*

The illustration of the sign correction for the novel decomposition is shown in figure (3.11). To explain why the sign correction is wrong, consider the correct decomposition of figure (3.9), where the correct definition for the vectors $\boldsymbol{n}_{\parallel}$ and $\boldsymbol{n}_{\perp}$ is employed. By focusing on the traction $t_{\parallel}^{-}$ acting on $s_{\perp}^{-}$, we see that it is negative, as its scalar product with the $\boldsymbol{n}_{\perp}^{-}$ vector is negative. This means that $t_{\parallel}^{-}$ effectively closes the gap in between Ω_- and Ω_+. This makes perfect sense, and there is no need of a sign correction of the opening and traction components based on the sign of the standard components when the normal unit vectors relative to the virtual interfaces are defined correctly.

Once the sign of the traction and the opening for the novel formulation has been (wrongly) adjusted, it is possible to formulate the novel TSL. It is assumed that only one damage mechanism can be active for a given numerical interface, which is either matrix cracking along the parallel virtual interface or simultaneous fiber and matrix cracking along the transverse virtual interface. The novel TSL is based on this active damage mechanism. Additionally, it is assumed that if a damage mechanism is activated but does not lead to complete failure, the other cannot be activated afterwards. To determine the TSL, the following procedure is assumed. First, it is checked if $t_{\perp}$ reaches the cohesive strength of the parallel virtual interface, which is assumed to be equal to the lamina tensile strength for matrix cracking $\sigma_{c_{\parallel}}$. If so, the TSL for matrix cracking is activated. If not, it is checked if $t_{\parallel}$ reaches the cohesive strength of the transverse virtual interface, which is assumed to be equal to the lamina tensile strength for simultaneous fiber and matrix cracking $\sigma_{c_{\perp}}$. If so, the TSL for simultaneous fiber and matrix cracking is activated. If not, no TSL is activated. The various conditions for the TSL selection are illustrated in figure (3.12). Based on the equations for the standard TSL illustrated in sub-section (3.1.1), the equations for the novel TSL become

$$\Delta_{eff} = \begin{cases} \Delta_{\perp}, & \text{matrix failure} \\ \Delta_{\parallel}, & \text{fiber and matrix failure} \end{cases} \tag{3.17}$$

$$t_{eff} = \begin{cases} t_{\perp}, & \text{matrix failure} \\ t_{\parallel}, & \text{fiber and matrix failure} \end{cases} \tag{3.18}$$

$$\sigma_c \text{ and } G_c = \begin{cases} \sigma_{c_{\parallel}} \text{ and } G_{c_{\parallel}}, & \text{matrix failure} \\ \sigma_{c_{\perp}} \text{ and } G_{c_{\perp}}, & \text{fiber and matrix failure} \end{cases} \tag{3.19}$$

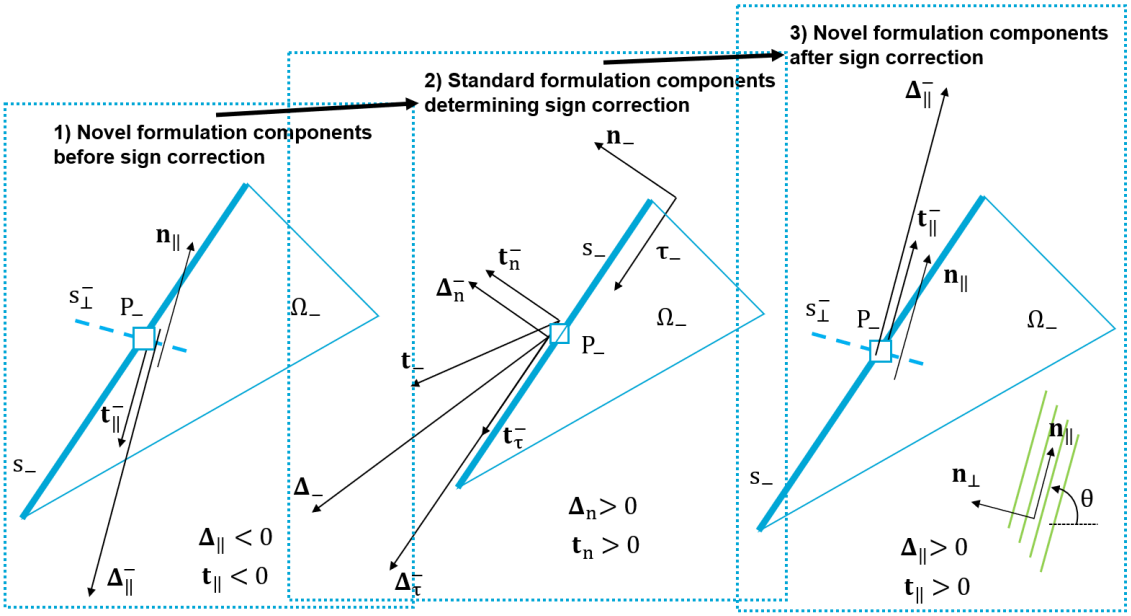

Figure 3.11: *(Wrong) Adjustment of the traction and opening components for the novel damage formulation based on the standard formulation. On the left, considering the opening along the transverse virtual interface $s_{\perp}^{-}$, it is observed that the parallel traction and opening $t_{\parallel}^{-}$ and $\Delta_{\parallel}^{-}$ are defined to be negative with respect to the unit vector parallel to the fiber direction $\boldsymbol{n}_{\parallel}$. On the middle, we see that the sign of the normal components according to the standard decomposition t_n^{-} and Δ_n^{-} are both positive. On the right, t_n^{-} is assumed to control the sign of $t_{\parallel}^{-}$, while Δ_n^{-} is assumed to control the sign of $\Delta_{\parallel}^{-}$.*

$$t_{eff} = \begin{cases} \sigma_c\left(1 - \frac{\Delta_{eff}}{\Delta_c}\right), & \text{softening} \\ t_{max}\frac{\Delta_{eff}}{\Delta_{max}}, & \text{unloading} \end{cases} \tag{3.20}$$

where

$$\Delta_c = \frac{2G_c}{\sigma_c} \tag{3.21}$$

and Δ_{max} and t_{max} are the effective opening and traction reached at maximum damage extension upon irreversible softening. Finally, based on equation (3.20), the effective traction vector is obtained as

$$\boldsymbol{t}_{eff} = \begin{cases} t_{eff}\,\boldsymbol{n}_{\perp}, & \text{matrix failure} \\ t_{eff}\,\boldsymbol{n}_{\parallel}, & \text{fiber and matrix failure} \end{cases} \tag{3.22}$$

As a final remark for the proposed TSL, it is essential to correct the cohesive toughness G_c for the mismatch in length between the numerical interface and the active virtual interface, so that the correct amount of energy is dissipated. First, the active fracture toughness is set to be equal either to the lamina tensile toughness parallel to the fiber direction $G_{c_{\parallel}}$, or to the lamina tensile toughness transverse to the fiber direction $G_{c_{\perp}}$, depending on the active fracture mechanism. Then, the adjustment of the active toughness is achieved by dividing it by the cosine of the angle between the numerical surface and the active virtual surface $\cos\alpha_{\parallel}$ or $\cos\alpha_{\perp}$. Referring to figure (3.13), the equation for the adjusted G_c is expressed as:

$$G_c = \begin{cases} \frac{G_{c_{\parallel}}}{\cos\alpha_{\parallel}}, & \text{matrix cracking} \\ \frac{G_{c_{\perp}}}{\cos\alpha_{\perp}}, & \text{fiber and matrix cracking} \end{cases} \tag{3.23}$$

3.2. Implementation Aspects

The present section details the implementation of the novel CZM damage formulation for arbitrary damage in composites within the Summit-lite framework. Summit-lite already incorporates a suite of functions for the CZM standard damage formulation illustrated in sub-section (3.1.1) which is designed

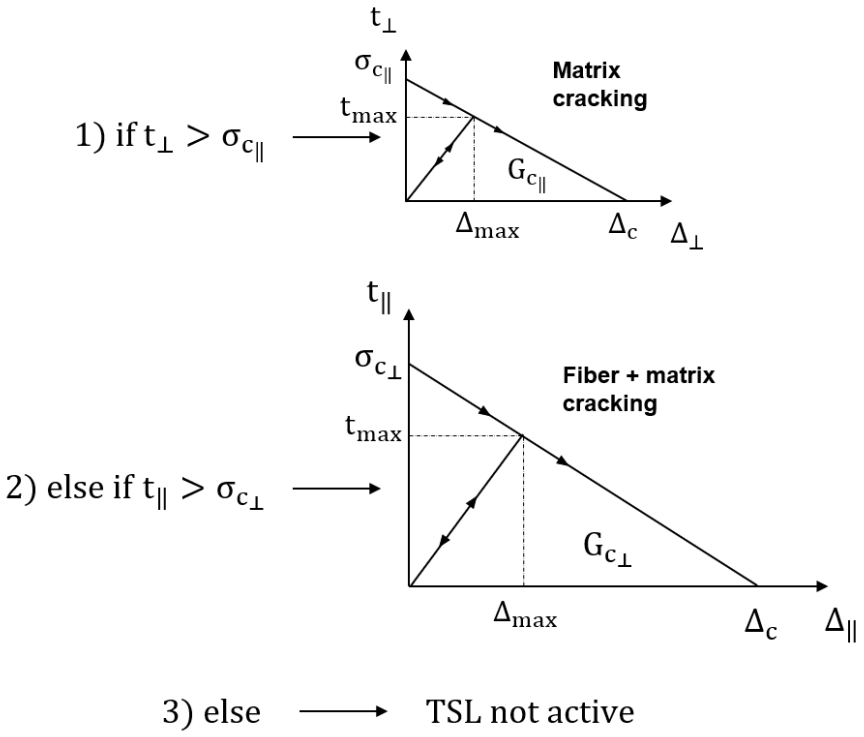

Figure 3.12: *Selection of the novel TSL based on the active damage mechanism. First, it is checked whether the transverse traction $t_\perp$ reaches the lamina tensile strength for fracture parallel to the fiber direction $\sigma_{c_\parallel}$. If that is the case, the TSL for matrix cracking is activated. Otherwise, it is checked whether the parallel traction $t_\parallel$ reaches the lamina tensile strength for fracture transverse to the fiber direction $\sigma_{c_\perp}$. If that is the case, the TSL for fiber and matrix cracking together is activated. If neither condition is met, no TSL is activated. (Δ_{max}, t_{max}) represents the point of maximum damage reached upon irreversible softening.*

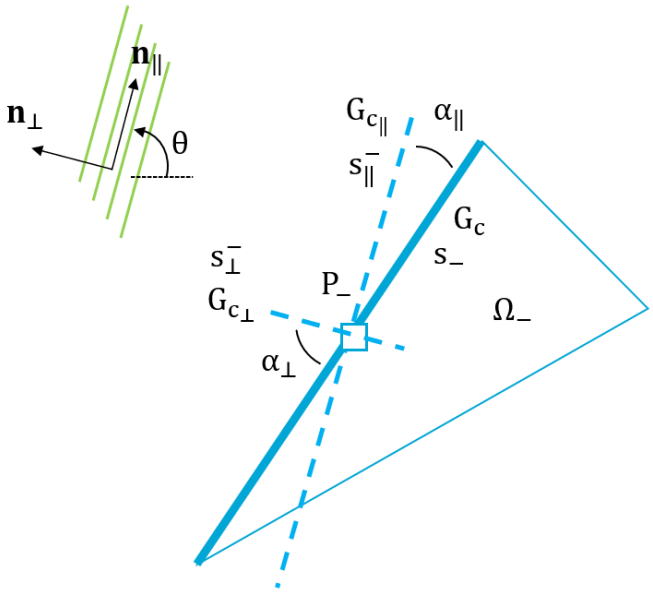

Figure 3.13: *Adjustment of the cohesive toughness G_c. Despite introducing virtual interfaces $s_\parallel$ and $s_\perp$ to compute the cohesive fracture properties for an arbitrary numerical interface s, the crack is still assumed to occur along this original numerical interface. Due to the mismatch in length between the numerical interface and the active virtual interface, G_c needs to be adjusted with the cosine of the angle between these two interfaces. In case of matrix cracking, G_c is set equal to the lamina tensile toughness parallel to the fiber direction $G_{c_\parallel}$ and adjusted by dividing it by $\cos\alpha_\parallel$, the cosine of the angle between s and the active virtual interface $s_\parallel$, while in the case of simultaneous fiber and matrix cracking, G_c is set equal to the lamina tensile toughness transverse to the fiber direction $G_{c_\perp}$ and adjusted by dividing it by $\cos\alpha_\perp$, the cosine of the angle between s and the active virtual interface $s_\perp$.*

for damage in isotropic structures. Many of these functions are reusable for implementing the novel method, thus simplifying the development process.

Summit-lite organizes CZM utilities into functions, each handling specific aspects of the model. These functions are specific for material assignment, solver selection for the linear momentum equilibrium equation, space discretization, and more. Building upon the existing infrastructure, this section focuses on implementing two key functions within the Summit-lite material functions.

The first function concerns the novel damage formulation proposed in sub-section (3.1.3) that controls the damage constitutive behavior at internal mesh boundaries. Additionally, the novel method necessitates the implementation of a function within the material library to govern the orthotropic stress-strain constitutive behavior of the bulk elements of the mesh. Unlike the cohesive elements at the mesh boundaries, which are affected by damage, these bulk elements remain undamaged. The orthotropic stress-strain equations are readily available in the literature and are provided in the appendix chapter (A).

By integrating these two functions into the material functions, Summit-lite aims to offer capabilities for simulating arbitrary intra-laminar damage in composite materials based solely on the evolving stress state of the lamina.

3.2.1. Orthotropic Stress-Strain Equation Implementation for Bulk Material

This sub-section implements the orthotropic stress-strain equations for the constitutive behavior of the bulk elements within the Summit-lite framework.

The 3D stress-strain equations for a composite lamina, as derived in the appendix chapter (A), are utilized here. Equations (A.1) are implemented into the novel Summit-lite function named *orthotropic*. In this function, the 5 independent elastic parameters of the lamina, along with the mode (plane stress, plane strain, or 3D), and the strain vector $\boldsymbol{\varepsilon}_{(xyz)}$ at the given quadrature point are provided. Based on these inputs, the function yields the stress vector $\boldsymbol{\sigma}_{(xyz)}$ at the specified quadrature point.

3.2.2. Novel Damage Formulation Implementation for Cohesive Interface Material

This sub-section implements the novel damage formulation proposed in sub-section (3.1.3) for simulating damage in cohesive elements at internal mesh boundaries of the numerical model within the Summit-lite framework. Notably, Summit-lite already implements the standard CZM damage formulation illustrated in sub-section (3.1.1) through the function *cohesive_dg*. This sub-section creates a variant of *cohesive_dg*, named *fiber_matrix_cohesive_dg* to implement the novel damage formulation. Unlike *cohesive_dg*, *fiber_matrix_cohesive_dg* tailors the numerical fracture properties of the cohesive interface to the specific fracture mechanism activated at the cohesive interface, namely matrix cracking, or simultaneous fiber and matrix cracking. The subsequent discussion will illustrate how the *fiber_matrix_cohesive_dg* function operates, including comparisons with the *cohesive_dg* function.

The flowchart depicted in figure (3.14) illustrates the damage constitutive update process for both the *cohesive_dg* and the *fiber_matrix_cohesive_dg* functions. This update process evaluates whether fracture has occurred at a specific quadrature point of a cohesive element and, if so, computes the cohesive traction at that quadrature point. Figure (3.14) provides a detailed explanation of each step in the damage constitutive update process.

The main differences between the *cohesive_dg* and *fiber_matrix_cohesive_dg* functions in the damage constitutive update are highlighted as follows:

1. Opening and traction components: For the standard implementation, the assessment of the opening and traction components involves determining the normal and tangential components relative to the numerical interface. Conversely, in the case of the novel implementation, the evaluation focuses on the components parallel and transverse to the fiber direction. Depending on the active failure mechanism, either the parallel or the transverse components are identified as the components contributing to the virtual opening of the active virtual interface. The detailed process of evaluating these components is outlined in figure (3.15).
2. Fracture initiation and evolution: In *cohesive_dg*, fracture initiation and evolution consider both normal and tangential components to the numerical interface, effectively describing a mixed-mode opening fracture, while in *fiber_matrix_cohesive_dg*, only normal components to the active virtual interface contribute to virtual fracture, which configures as a mode I opening scenario.

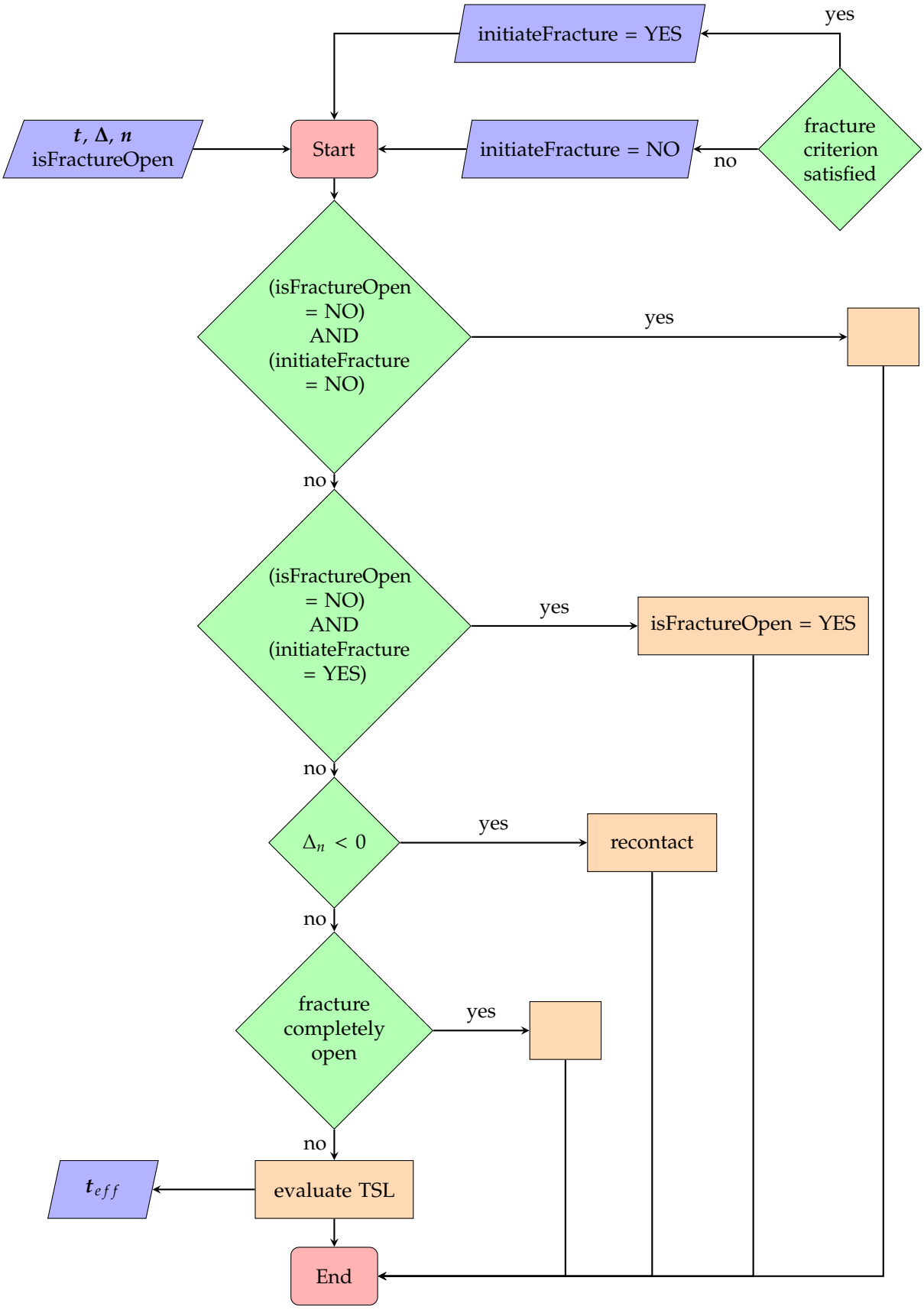

Figure 3.14: *The damage constitutive update process is formally the same for both the standard and the novel implementations. The constitutive update function, applied at a specific quadrature point of the cohesive interface of interest, accepts input variables such as traction* $\boldsymbol{t}$*, opening* $\boldsymbol{\Delta}$*, unit normal vector* $\boldsymbol{n}$*, and boolean variables* $initiateFracture$ *and* $isFractureOpen$*. The value of* $initiateFracture$ *is determined by a fracture criterion specific to each case. If* $initiateFracture$ *is equal to YES, fracture initiation occurs, and* $isFractureOpen$ *is subsequently set to YES. When* $isFractureOpen$ *is equal to YES, it indicates that fracture is ongoing. If fracture is active, the function assesses whether the normal opening* Δ_n *is greater than 0. In such case, the TSL is evaluated, yielding the effective cohesive traction* $\boldsymbol{t}_{eff}$ *as output for the function. Conversely, if* Δ_n *is less than 0, the function deals with re-contact scenarios.*

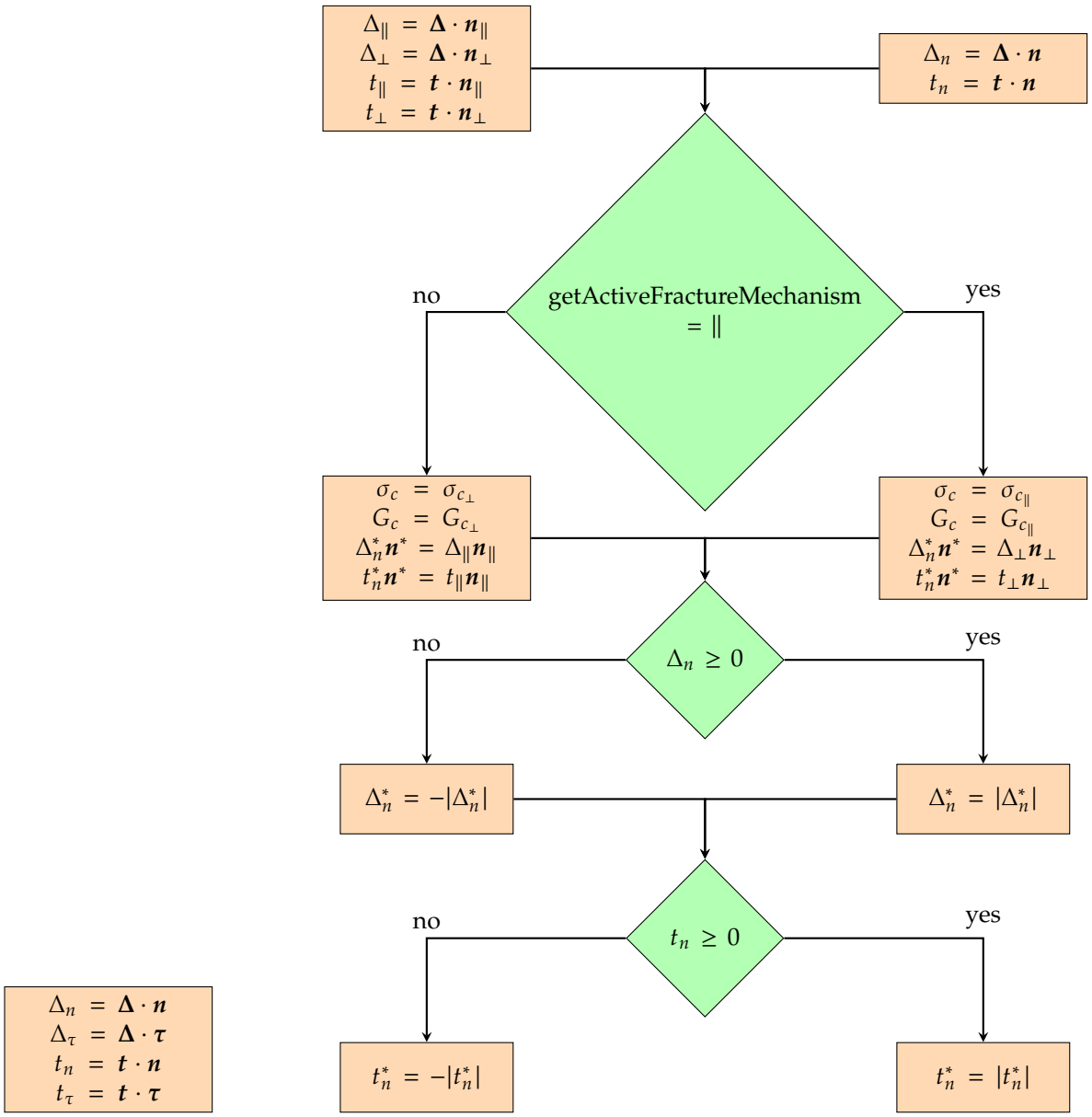

(a) Components for Standard Implementation

(b) Components for Novel Implementation

Figure 3.15: *The evaluation of the opening and traction components differs between the standard and the novel damage implementations. In the standard case, the components normal and tangential to the numerical interface, denoted as Δ_n, Δ_τ, t_n, t_τ, need to be determined. Instead, for the novel case, the components parallel and transverse to the fiber direction, denoted as $\Delta_\parallel$, $\Delta_\perp$, $t_\parallel$, $t_\perp$, need to be determined. Additionally, Δ_n and t_n are required to assess the sign of the opening and traction components normal to the active virtual interface, denoted as Δ_n^* and t_n^*. The determination of Δ_n^* and t_n^*, the unit vector normal to the active virtual interface $\boldsymbol{n}^*$, and the cohesive fracture parameters σ_c and G_c, all depend on the value of the $getActiveFailureMechanism$ parameter, which is determined by the fracture initiation criterion (see figure (3.16)). The parameter is set to $\parallel$ if matrix fracture along the parallel virtual interface occurs, or $\perp$ if simultaneous fiber and matrix fracture along the transverse virtual interface occurs. The sign of Δ_n^* is dictated by the sign of Δ_n, while the sign of t_n^* is determined by the sign of t_n.*

This differences are illustrated in figure (3.16) for fracture onset and figure (3.17) for damage evolution.

3.3. Verification against Analytical Model

The objective of this section is to verify the CZM Summit-lite implementation outlined in section (3.2) based on the novel method for arbitrary damage in composites. Specifically, the focus is on verifying the novel damage formulation implemented in sub-section (3.2.2) through comparison with a simple analytical configuration. This configuration comprises two elements joined by a cohesive interface and subjected to tensile traction normal to the interface. Additionally, the orthotropic stress-strain equations implemented in sub-section (3.2.1) are subjected to verification against analytical results derived from the Classical Laminate Theory (CLT).

3.3.1. Orthotropic Stress-Strain Equation Verification

This sub-section illustrates the verification of the orthotropic stress-strain equations implemented in sub-section (3.2.1). The verification process consists of two steps.

The first step involves verifying the stress calculation at a single quadrature point to identify potential errors in the constitutive equations (A.1) implemented in the *orthotropic* function. A pre-defined strain vector $\boldsymbol{\varepsilon}$ is input into the *orthotropic* function, and the resulting stress vector $\boldsymbol{\sigma}$ is computed. Any discrepancies between the numerical and hand-calculated stress results would indicate errors in the implemented equations.

In the second step, a simple Finite Element Method (FEM) setup relying on the *orthotropic* function is established to verify the orthotropic stress-strain equations against analytical results obtained from the CLT. The main idea is to apply the same Boundary Conditions (BCs) in both the FEM and the CLT, and check whether the strain results in the two models are consistent. More details on the CLT are given in the appendix chapter (B). The FEM setup is as follows:

- Spatial discretization: The mesh configuration depicted in figure (3.18) is selected, consisting of 2D triangular linear FEs with translational Degrees of Freedom (DOFs) for the nodes u_x and u_y;
- Time discretization: An explicit Newmark solver is employed for time discretization. The load rate is adjusted to achieve quasi-static simulation conditions closely matching the static loading conditions of the CLT. The stable time step for the chosen dynamic solver is estimated in equation (3.24);
- Material assignment: The elements are assigned orthotropic material properties from function *orthotropic*;
- BCs assignment: Neumann BCs are prescribed at the nodes on the external boundaries of the mesh.

The stable time step is estimated based on the major Young's modulus of the lamina E_1 to ensure conservative results:

$$t_s = L_c \sqrt{\frac{\rho}{E_1}} \tag{3.24}$$

where L_c is the characteristic length of the FEs, defined as the radius of the circumference inscribed to the elements, and ρ is the material density.

The strain results from the FE analysis are compared to those obtained from the CLT. The goal is to ensure that the error in strain between the two models decreases as the loading conditions approach the static conditions of the CLT. Figure (3.19) illustrates the strain error between the FE analysis and the CLT at different load rates. The convergence of strain results between the two models by reducing load rates verifies the accuracy of the implemented orthotropic stress-strain equations.

3.3.2. Novel Damage Formulation Verification

This sub-section aims to verify the novel damage formulation implemented in sub-section (3.2.2) by comparing the results of a FEM built upon this novel formulation with analytical results for a simple configuration consisting of two elements joined by a cohesive interface.

The analytical results are derived for the configuration depicted in figure (3.20). The figure illustrates two triangular elements joined by a cohesive interface of infinitesimal thickness. It is assumed that

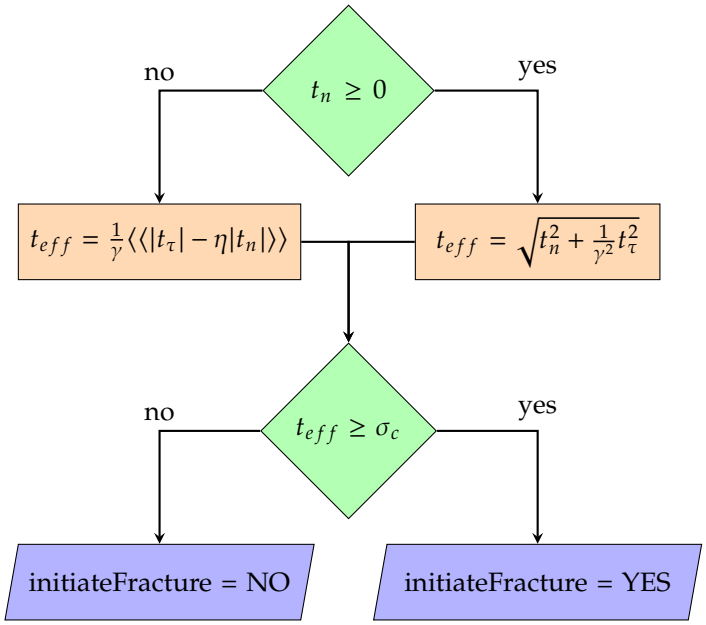

(a) Fracture Initiation for Standard Implementation

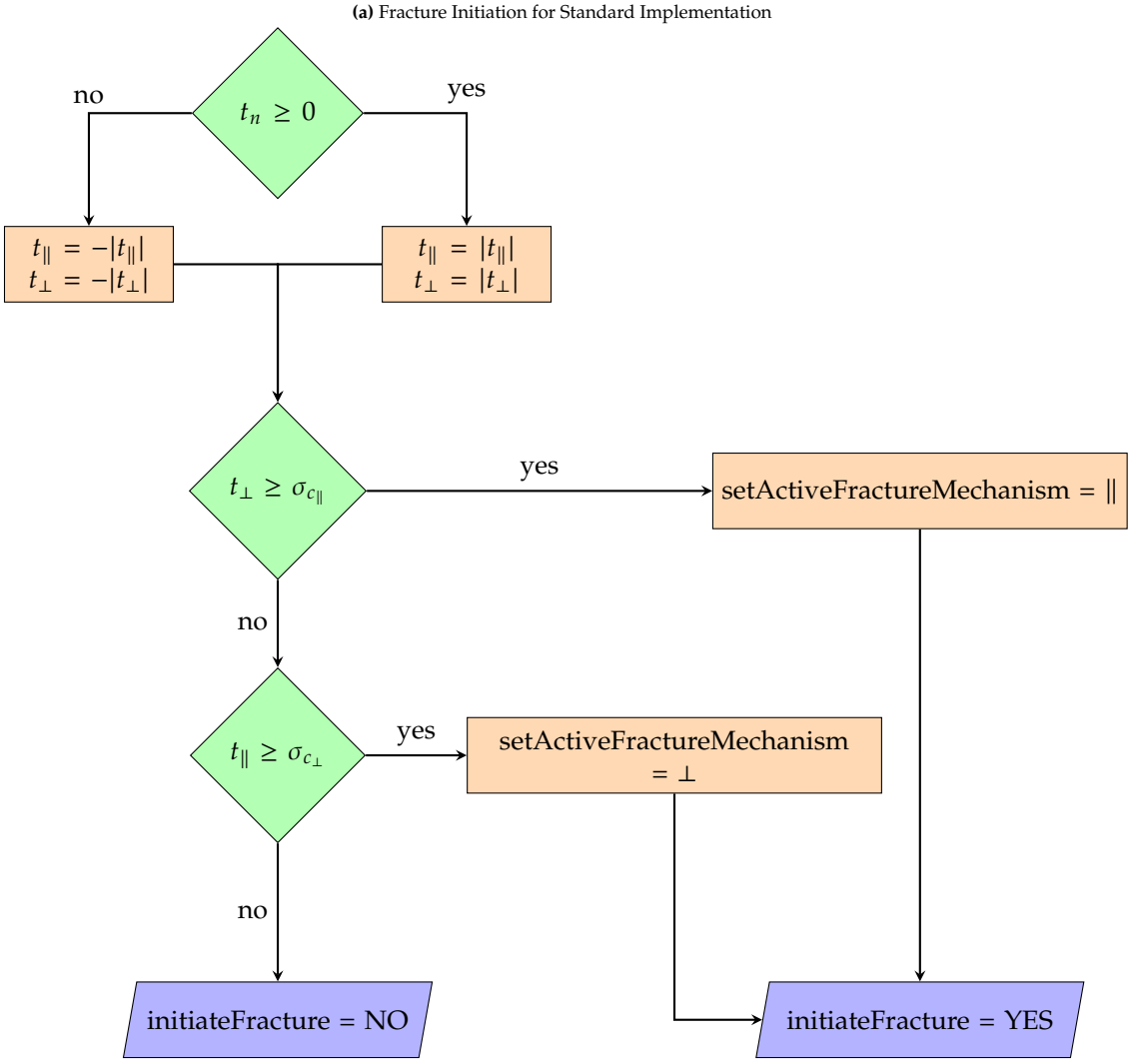

(b) Fracture Initiation for Novel Implementation

Figure 3.16: *The fracture initiation criterion differs between the standard and the novel damage implementations. In the standard case, fracture initiation is determined by evaluating the effective traction t_{eff}, which is derived from both the normal and transverse traction components t_n and t_τ, along with the mixed-mode coefficient γ, and the friction coefficient η. If t_{eff} surpasses the cohesive strength σ_c of the numerical interface, fracture initiation occurs, and the variable $initiateFracture$ is flagged as YES. Otherwise, $initiateFracture$ is set to NO. For the novel case, fracture initiation depends on the traction components parallel and transverse to the fiber direction $t_\parallel$ and $t_\perp$. The signs of $t_\parallel$ and $t_\perp$ are assumed to be controlled by t_n. $t_\parallel$ is compared to the lamina tensile strength for fracture transverse to the fiber direction $\sigma_{c_\perp}$, and $t_\perp$ is compared to the lamina tensile strength for fracture parallel to the fiber direction $\sigma_{c_\parallel}$. Upon either traction component reaching its respective strength fracture initiation occurs, and the variable $setActiveFractureParameter$ is adjusted based on the active fracture mechanism, with $initiateFracture$ set to YES. If neither $t_\parallel$ and $t_\perp$ reaches its respective strength, $initiateFracture$ is set to NO.*

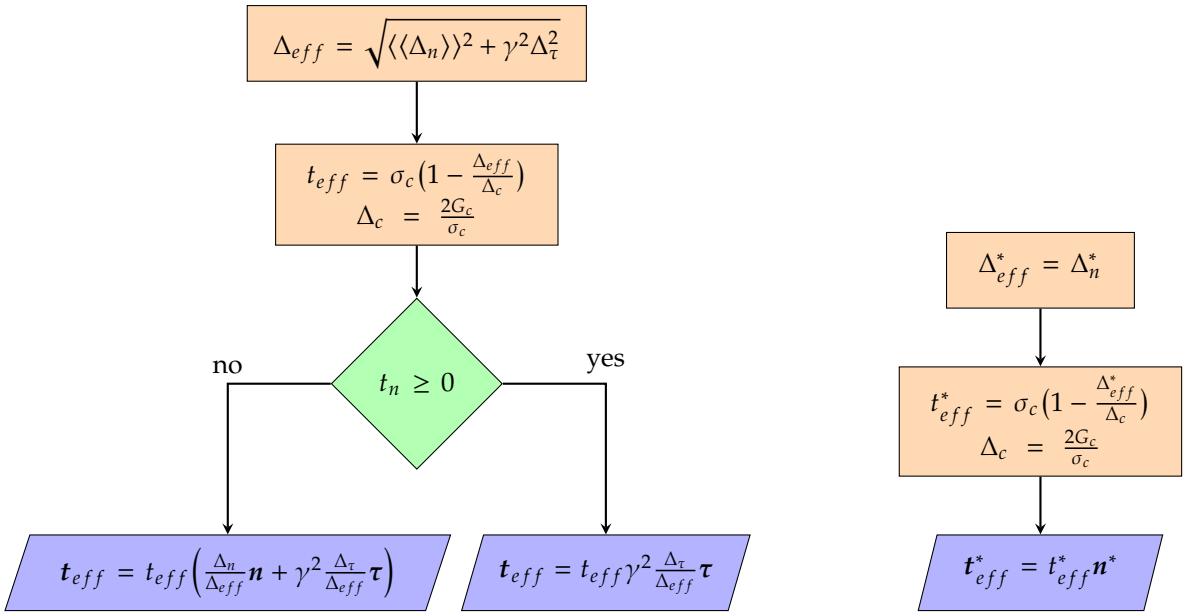

(a) Fracture Evolution for Standard Implementation

(b) Fracture Evolution for Novel Implementation

Figure 3.17: *The fracture evolution differs between the standard and novel damage implementations. In the standard TSL, the effective opening Δ_{eff} is computed based on both the openings normal and tangent to the numerical interface Δ_n and Δ_τ, and subsequently, the effective traction t_{eff} is calculated using the linear extrinsic DG TSL t_{eff} - Δ_{eff}. Finally, the effective traction vector $\boldsymbol{t}_{eff}$ is determined considering contributions from both Δ_n and Δ_τ. In contrast, for* fiber_matrix_cohesive_dg, *no shear contributions are considered. The effective virtual opening Δ^*_{eff} is assumed to be equal to the virtual opening Δ^*_n normal to the active virtual interface. Similarly, the effective virtual traction vector $\boldsymbol{t}^*_{eff}$ is aligned with the unit normal vector $\boldsymbol{n}^*$ to the active virtual interface.*

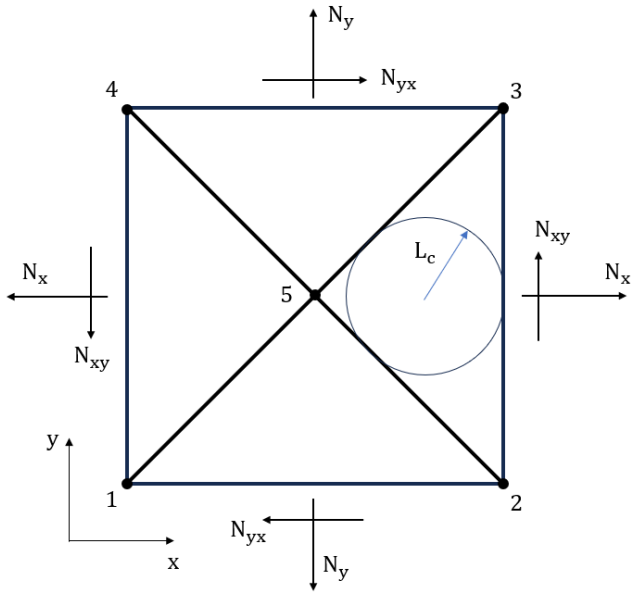

Figure 3.18: *Mesh considered for verifying the orthotropic stress-strain equations. 4 triangular FEs are considered. The characteristic length L_c is estimated as the radius of the inscribed circumference to the FEs. The BCs specified in terms of forces per unit width N_x, N_y, N_{xy} according to the CLT are converted into concentrated forces for the FEM analysis and applied as Neumann BCs at the mesh boundary nodes.*

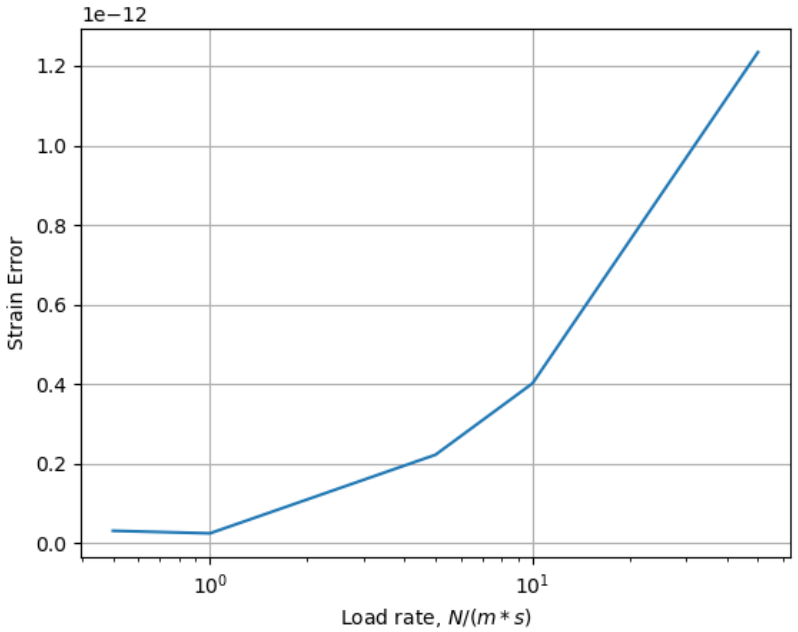

Figure 3.19: *Strain error between the FEM and the CLT at different load rates. As shown, the strain error between the two models diminishes as the load rate decreases, approaching the static loading conditions of the CLT.*

the two elements follow a linear elastic stress-strain relation and are made of an isotropic material of Young's modulus E. The cohesive interface possesses cohesive fracture properties σ_c and G_c. A displacement $\boldsymbol{d}$ is applied at the right node of the right element, while the displacement at the left node of the left element is set to 0. As a consequence of the applied displacement, the two elements start to deform elastically, resulting in the emergence of a tensile traction $\boldsymbol{\sigma}$ normal to the cohesive interface. Once the traction reaches the cohesive strength σ_c of the interface, this begins to open by a quantity δ, and fails completely when the critical opening $\delta = \delta_c$ is reached. According to the linear stress-strain

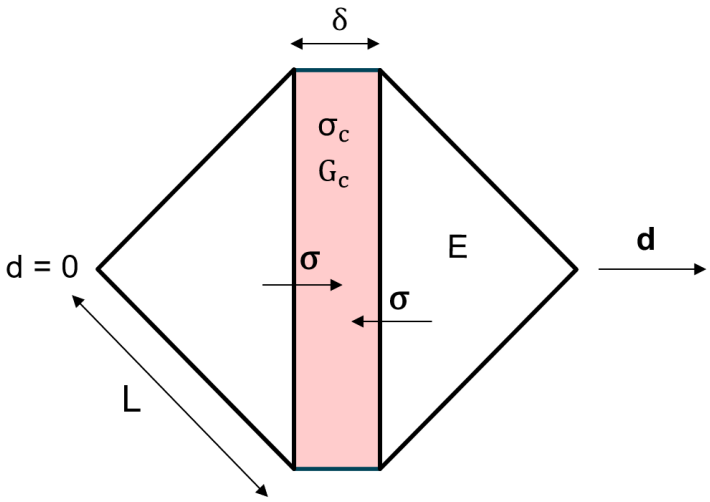

Figure 3.20: *Reference configuration for the verification of the anisotropic damage formulation. Two triangular elements of size L are joined by a cohesive interface, highlighted in pink. A displacement $\boldsymbol{d}$ is applied to the right node, while the left node is kept fixed. The elements have Young's modulus E, and the cohesive interface has cohesive strength σ_c and cohesive fracture toughness G_c. δ represents the opening of the cohesive interface after fracture onset, and $\boldsymbol{\sigma}$ is the traction that arises at the cohesive interface.*

assumption, the traction at the interface is given by

$$\sigma = E\varepsilon \tag{3.25}$$

Before fracture onset of the cohesive interface, the contribution to d is solely due to the elastic deforma-

tion d_e of the elements, as $\delta = 0$ according to the extrinsic DG TSL:

$$d = 2d_e + \delta = 2d_e, \quad d \leq d_{on} \tag{3.26}$$

where

$$d_{on} = \sqrt{2}\frac{L\sigma_c}{E} \tag{3.27}$$

represents the displacement at fracture onset. Before fracture onset, the strain at the right node is estimated as

$$\varepsilon = \frac{d_e}{L/\sqrt{2}} \tag{3.28}$$

Substituting equation (3.28) into (3.25), we find:

$$d_e = \frac{1}{\sqrt{2}}\frac{L\sigma}{E} \tag{3.29}$$

Substituting (3.29) in (3.26), the traction before damage onset is given by

$$\sigma = \frac{1}{\sqrt{2}}\frac{Ed}{L} \tag{3.30}$$

Considering the post-fracture regime, the opening δ of the cohesive interface is assumed to be regulated by the linear extrinsic DG TSL:

$$\delta = \delta_c\left(1 - \frac{\sigma}{\sigma_c}\right) \tag{3.31}$$

Substituting (3.31) into equation

$$d = 2d_e + \delta \tag{3.32}$$

we obtain

$$\sigma = (\delta_c - d)\frac{Ed}{L}\frac{E\sigma_c}{E\delta_c - \sqrt{2}L\sigma_c} \tag{3.33}$$

Considering both equations before and after fracture onset ((3.30) and (3.33)), the TSL becomes:

$$\sigma(d) = \begin{cases} \frac{1}{\sqrt{2}}\frac{Ed}{L}, & d \leq d_{on} \\ (\delta_c - d)\frac{Ed}{L}\frac{E\sigma_c}{E\delta_c - \sqrt{2}L\sigma_c}, & d_{on} < d \leq d_c \end{cases} \tag{3.34}$$

where

$$d_c = \delta_c \tag{3.35}$$

is the displacement at complete failure.

The FEM setup for the damage formulation verification includes the following:

- Weak formulation: The weak formulation of the equilibrium of linear momentum (C.7), which forms the foundation of this DG/CZM FE formulation, is established. The equation is derived in the appendix chapter (C);
- Spatial discretization: Triangular linear 2D FEs with translational DOFs for the nodes u_x and u_y are selected;
- Time Discretization: An explicit Newmark solver is employed for time discretization. The displacement rate is adjusted to achieve quasi-static simulation conditions closely matching the static loading conditions assumed for the analytical configuration of figure (3.20). The stable time step for the chosen dynamic solver is estimated in equation (3.24);
- Material assignment: The bulk elements are assigned isotropic material properties, while the cohesive interface between the two elements is set to behave according to the novel damage formulation of function *fiber_matrix_cohesive_dg*;
- BCs assignment: Dirichlet BCs are prescribed at the left and right nodes of the mesh.

The verification was done in incremental steps to facilitate the development the FEM setup. Initially, the simulation was conducted up to $d < d_{on}$, without including the cohesive interface, allowing for the verification of the FE setup in the pre-fracture regime. Upon achieving a match between the results of the two models, the investigation extended to the post-fracture regime by incorporating the cohesive interface. Initially, the interface material was defined according to the *cohesive_dg* function, enabling the verification of the FE setup also in the post-fracture regime. Once the results of the two models aligned, the analysis progressed to the novel interface material defined in *fiber_matrix_cohesive_dg*. The simulation was conducted with two different fiber orientations: parallel and transverse to the cohesive interface. It is noted that selecting a fiber angle other than these two would render it impossible to define the cohesive fracture properties for the cohesive interface in the analytical formulation. The two specific analytical configurations for the verification are illustrated in figure (3.21). It is also noted that for the configuration of figure (3.20), the opening is a pure mode I opening, as the traction is transverse to the interface. This means that, even if mode I opening is assumed in the novel damage formulation (sub-section (3.1.3)), *fiber_matrix_cohesive_dg* and *cohesive_dg* functions are expected to yield the same results here.

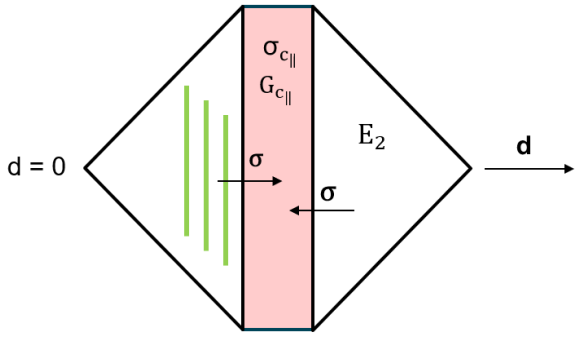

(a) Cohesive Interface Parallel to Fibers

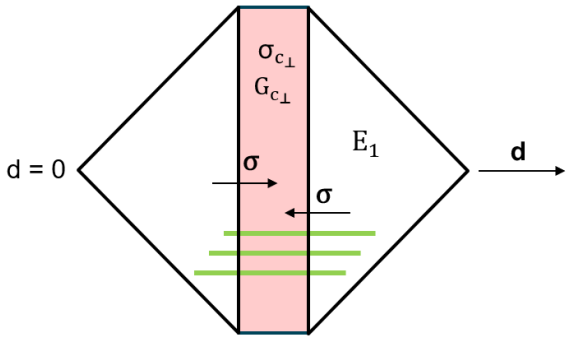

(b) Cohesive Interface Transverse to Fibers

Figure 3.21: *Special analytical configurations for novel damage formulation verification. The fiber direction is indicated in green and can be either parallel or transverse to the cohesive interface. Consequently, the Young's modulus of the elements is set to either the minor or the major Young's modulus E_2 or E_1, and the cohesive fracture properties of the interface are set equal to the lamina tensile fracture properties parallel or transverse to the fiber direction $\sigma_{c_\parallel}$ and $G_{c_\parallel}$, or $\sigma_{c_\perp}$ and $G_{c_\perp}$.*

3.4. Validation against Experimental Data

This section outlines the process for validating the novel CZM damage formulation for arbitrary damage in composites developed in this work. To accomplish this, the novel damage formulation is incorporated into the DG/CZM framework available in Summit-lite. Subsequently, the FEM utilizing the novel formulation is employed to simulate damage in composite laminates subjected to Compact Tension (CT) testing. The results obtained from the numerical model are then compared to experimental data sourced from relevant literature.

The subsequent sub-section details the experimental setup for the CT test, which serves as the reference for validating the method. Guided by the experiment specifications, the numerical setup is

established to ensure its assumptions align with the experimental conditions.

3.4.1. Experimental Setup

In this sub-section, the experimental setup by Jose et al. [33] is presented. The experiment involved CT tests of Uni-Directional (UD) laminates. Two types of laminates, each consisting of 30 plies, were tested: a $[90°]_{30}$ laminate, with the fiber direction perpendicular to the applied load, and a $[0°]_{30}$ laminate, with the fiber direction parallel to the applied load. It is important to note that the convention used for $[90°]_{30}$ and $[0°]_{30}$ in this thesis is opposite to that used in the article. FD curves were derived from the two CT tests, which serve as experimental references for the numerical results obtained from the novel DG/CZM setup discussed in sub-section (3.4.2).

The CT test of composites is one of the methods adopted for evaluating their material fracture properties. According to Monticeli et al. [34], one of the primary objective of CT tests is to determine the fracture toughness of the laminate under examination. In CT specimens, a pre-notch is created at the middle of one edge of the laminate, along with two holes drilled at an equal distance from the notch. The test involves the application of an equal force to the two holes using tensile clevises. The damage mechanisms induced by this loading include matrix damage parallel to the fiber direction, as well as simultaneous fiber and matrix cracking transverse to the fiber direction. Monticeli et al. [34] provide an extensive review of the CT test of composites, inclusive of the fracture mechanisms that can be observed according to the specific test settings.

The specimen geometry is illustrated in figure (3.22). Concerning the notch geometry, initially, a

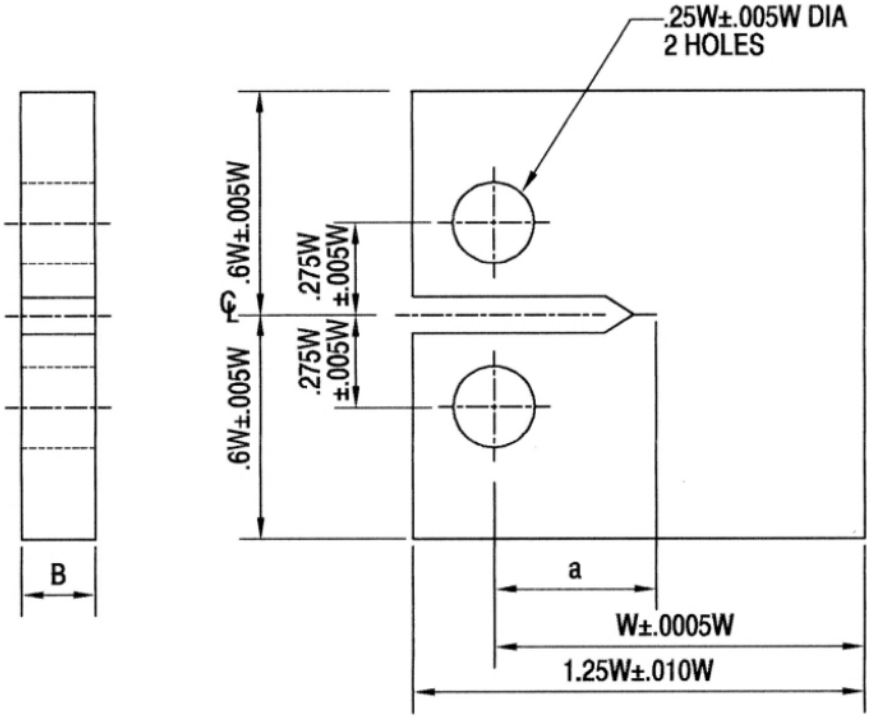

	a	W	B
Dimension (mm)	25.4	50.8	3.0

Figure 3.22: The geometry of the CT specimens in the article's experiment is defined by the parameters a, W, B. Figure credits: Jose et al. [33].

straight notch is created using a straight head disc cutter of 1.5 mm thickness, followed by refining with a razor blade to achieve a symmetric and sharp starter notch.

The plies composing the laminates are made of M55J/M18 carbon/epoxy material. The elastic and fracture properties of this material are presented in table (3.1). It is worth noting that ρ and ν_{23} from table (3.1) have been estimated from sources other than the article, with their values observed to have a minimal effect on the numerical results obtained from the novel model setup in sub-section (3.4.2). Additionally, the mode I tensile fracture toughnesses of the lamina, denoted as $G_{c_\parallel}$ and $G_{c_\perp}$, have been

Parameter	Value
ρ	1610.0 Kg/m^3
E_1	329.0 GPa
E_2	6.0 GPa
G_{12}	4.4 GPa
ν_{12}	0.346
ν_{23}	0.500
$\sigma_{c_\parallel}$	22.0 MPa
$\sigma_{c_\perp}$	1327.0 MPa
$G_{c_\parallel}$	0.168 KJ/m^2
$G_{c_\perp}$	31.678 KJ/m^2

Table 3.1: Material parameters for a M55J/M18 carbon/epoxy lamina.
ρ: density of the lamina; E_1, E_2, G_{12}, ν_{12}, ν_{23}: elastic properties of the lamina; $\sigma_{c_\parallel}$, $\sigma_{c_\perp}$: tensile strengths of the lamina; $G_{c_\parallel}$, $G_{c_\perp}$: mode I tensile fracture toughnesses of the lamina.

estimated using mode I fracture toughness Finite Element (FE) results provided in Jose et al. [33]'s article:

$$\begin{aligned} G_{c_\parallel} &= G_{Ic[90^\circ]_{30}} \\ G_{c_\perp} &= 2G_{Ic[0^\circ/90^\circ]_{15}} - G_{Ic[0^\circ]_{30}} \end{aligned} \tag{3.36}$$

$G_{c_\perp}$ in equations (3.36) is derived by assuming that the energy released by the cross-ply laminate tested in the article equals the sum of the energy released by half of its plies failing due to simultaneous fiber and matrix tensile failure and the other half failing due to matrix tensile failure.

The tests are conduced using an Instron machine, with two pins inserted into the specimen's holes. A quasi-static load is applied to one pin, while the other remains fixed. Specifically, the applied load rate is 3 kg/min for the $[90^\circ]_{30}$ laminate and 25 kg/min for the $[0^\circ]_{30}$ laminate.

Regarding the experimental results, in both cases, matrix cracking is observed to align with the fiber direction, as depicted in figure (3.23). No fiber cracking is reported in either case. It is also noted that no delamination between plies occurs. Two FD curves are generated from the two laminates, as illustrated

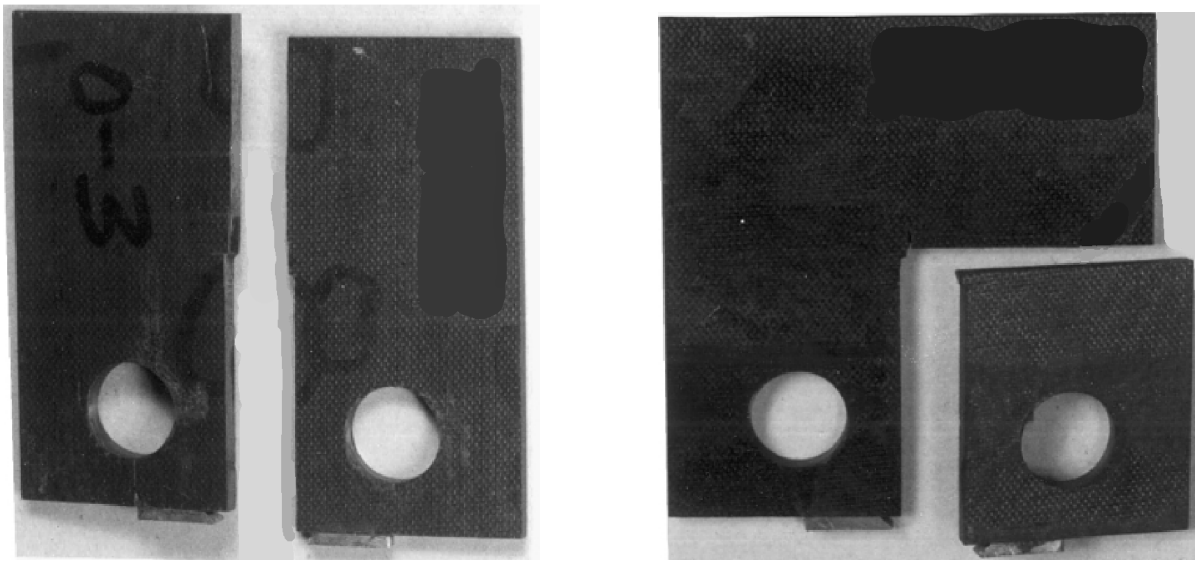

(a) 90 Laminate Crack **(b)** 0 Laminate Crack

Figure 3.23: *Crack surfaces observed in the* $[90^\circ]_{30}$ *and* $[0^\circ]_{30}$ *CT tests. In the* $[90^\circ]_{30}$ *laminate a mode I crack occurs, as the crack surface is transverse to the applied load. Conversely, in the* $[0^\circ]_{30}$ *laminate, a mode II crack occurs, as the crack surface is parallel to the applied load. Both fractures involve matrix cracking alone, with no fiber fracture. Also, in both cases, cracking occurs along the fiber direction. Figure credits: Jose et al. [33].*

in figure (3.24). It is noteworthy that the displacement in these curves is measured in terms of COD,

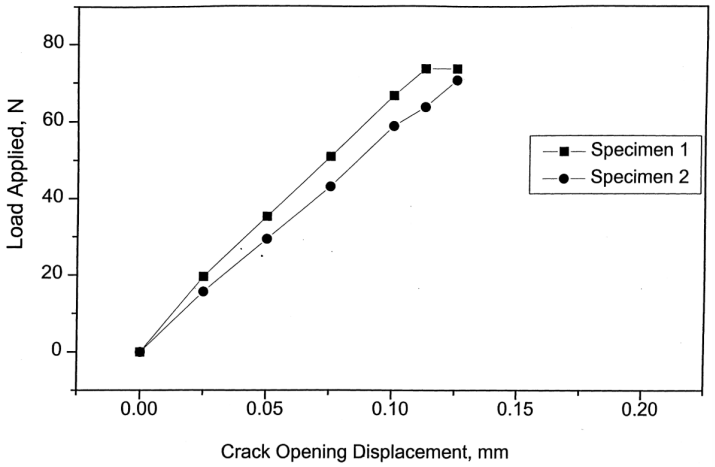

(a) 90 Laminate FD Curve

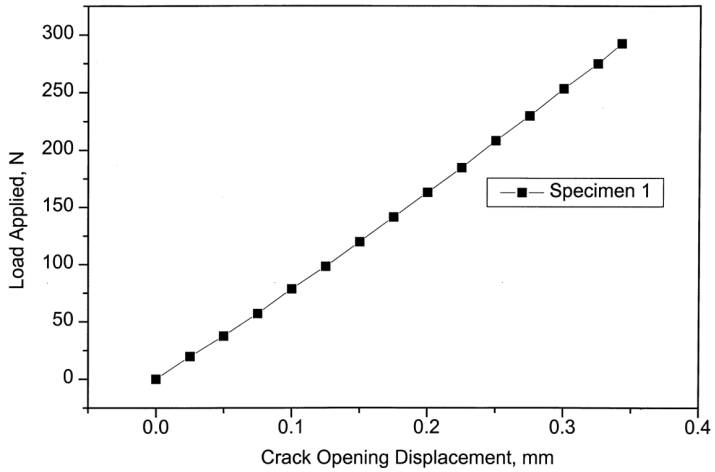

(b) 0 Laminate FD Curve

Figure 3.24: *FD curves generated from the CT specimens depict the force applied at the pin versus the COD far end to the crack tip. Figure credits: Jose et al. [33].*

with readings obtained by applying a clip gauge between the two gauge blocks shown in figure (3.25).

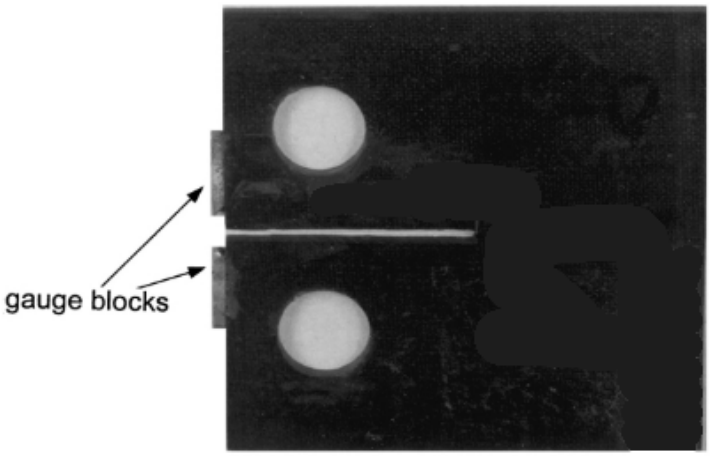

Figure 3.25: *Illustration of the measurement of the COD at the far end to the crack tip. A clip gauge is positioned between the gauge blocks in the figure to ensure the measurement. Figure credits: Jose et al. [33].*

3.4.2. Numerical Setup

To validate the novel damage formulation verified in sub-section (3.3.2), this was integrated into the DG/CZM framework available in Summit-lite, along with the orthotropic stress-strain equations (appendix chapter (A)). The resulting numerical model illustrated in this sub-section was then validated against the experimental data presented in sub-section (3.4.1). This sub-section outlines the novel numerical model setup, along with its underlying assumptions.

The numerical model involves several key components:

- Weak formulation: The weak formulation of the equilibrium of linear momentum (C.7), which forms the foundation of this DG/CZM FE formulation, is established. The equation is derived in the appendix chapter (C);
- Spatial discretization: A mesh with no bias direction is employed to allow for arbitrary intra-laminar damage. Triangular quadratic DG 2D FEs with translational DOFs for the nodes u_x and u_y are selected. The mesh size is adjusted based on the expected regions of damage from experimental results. The mesh adopted is shown in figure (3.26);
- Time discretization: An explicit Newmark solver is employed for time discretization. The load rate is adjusted to achieve quasi-static simulation conditions matching the loading conditions of the experimental setup. The stable time step for the chosen dynamic solver is estimated in equation (3.24), being L_c the lowest characteristic length among all the FEs of the mesh;
- Material assignment: The orthotropic material is assigned to the bulk elements of the mesh, while the novel damage formulation is assigned to the cohesive elements at the mesh internal boundaries;
- BCs Assignment: The BCs are applied at the nodes where the pins are assumed to be in contact with the specimen. A horizontal force is applied as a Neumann BC at the right hole, while Dirichlet BCs are prescribed at the left hole to keep it fixed. The BCs imposed are illustrated in figure (3.26);
- Parallel implementation: Parallel implementation is preferred to serial implementation due to the high number of DOFs of the mesh, allowing simulations to run much faster by taking advantage of multiple Central Processing Units (CPUs).

The mesh size is determined as $l_{ms} = l_{cz}/3$ in regions where damage is expected based on experimental results, and $l_{ms} = w/10$ where damage is not expected. Here, l_{cz} represents the length of the cohesive zone, and w is a geometrical parameter defined in figure (3.22). Considering matrix cracking alone, as observed in both tests in sub-section (3.4.1), Turon et al. [35] estimate l_{cz} using Hillerborg's model:

$$l_{cz} = \frac{E_2 G_{c_\parallel}}{\sigma^2_{c_\parallel}} \tag{3.37}$$

To accurately capture cohesive fracture, Pascoe et al. [36] suggest that at least 3 elements should be present along the cohesive zone. This reflects on the choice for l_{ms}.

It is highlighted that the DG formulation chosen for the numerical setup is best suitable for parallel implementation as it does not require mesh redefinition upon cracking, unlike the Continuous Galerkin (CG) formulation.

Regarding the laminate material model, the single lamina orthotropic model implemented in sub-section (3.2.1) is selected. This choice is based on the fact that both laminates from the tests in sub-section (3.4.1) are UD laminates, with no delamination occurring between their plies. Additionally, the plane stress mode is chosen due to the laminate's thickness being significantly smaller compared to its other dimensions.

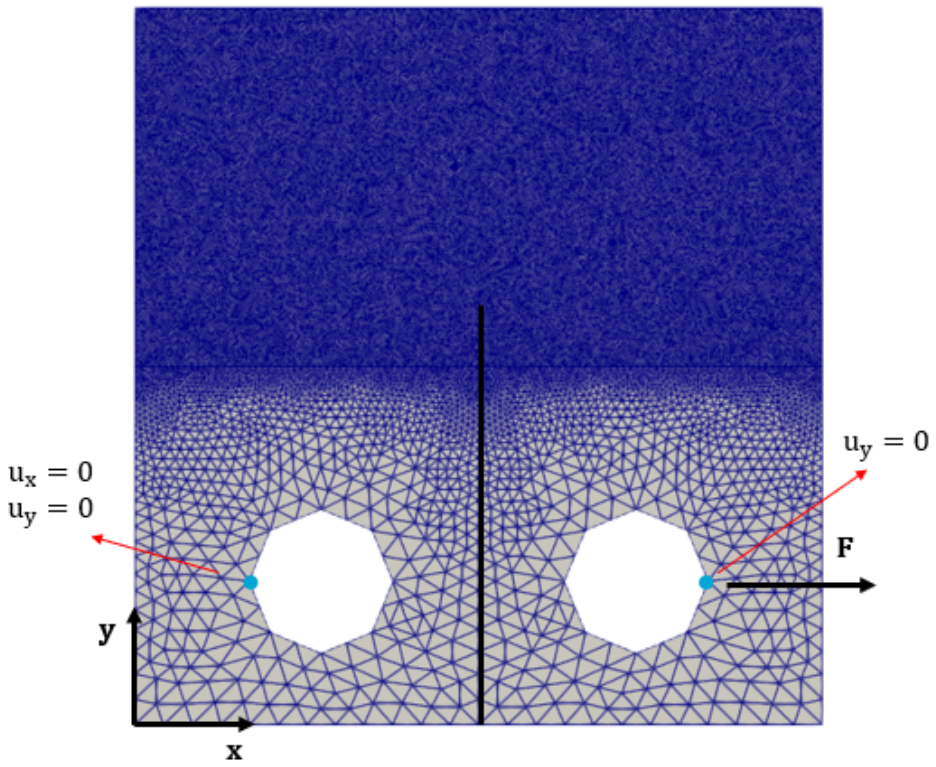

(a) Mesh and BCs for the CT Specimen

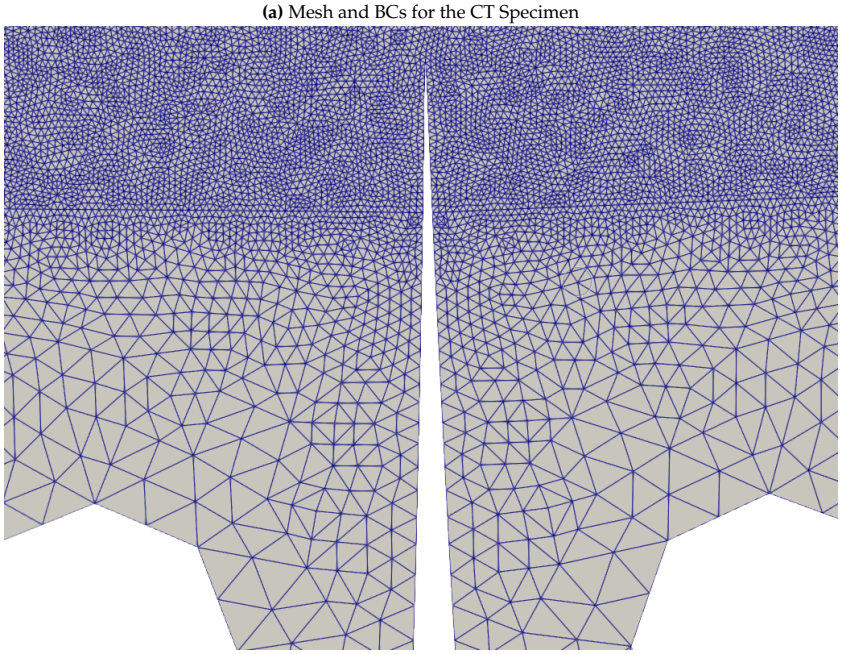

(b) Detail of Mesh Size where Fracture is Expected

Figure 3.26: *Mesh and BCs considered for the numerical model of the CT specimens. The mesh is designed to be fine in regions where fracture is expected based on experimental observations and coarse elsewhere. A horizontal force* ***F*** *is applied to the right hole to simulate the load applied through the pin, while the left hole is kept fixed.*

4

Results and Discussion

This chapter presents the results of the verification (performed in sub-section 3.3.2) and validation (illustrated in sub-section (3.4.2)) of the novel damage formulation for arbitrary damage in composites. The results are critically discussed, assessing the potential and the limitations of the new method.

4.1. Verification Results

The verification results for the the two interface configurations in sub-section (3.3.2) are illustrated in the graphs of figure (4.1). These graphs qualitatively demonstrate the error between the Finite Element (FE) formulation and the analytical formulation in terms of traction at the cohesive interface versus displacement applied at the right node of the model. The parameters selected for the analytical curves in figure (4.1) are summarized in table (4.1). The results indicate that setting a sufficiently low displacement rate d_r enables the traction-displacement curves for the two models to closely match. Small deviations from the analytical curve may be observed due to dynamic effects related to the chosen dynamic solver, especially upon damage onset, with these deviations expected to decrease further with a reduced d_r.

	Parallel	Transverse
E	$10.3\,GPa$	$147.0\,GPa$
σ_c	$57.0\,MPa$	$2280.0\,MPa$
G_c	$0.2\,KJ/m^2$	$50.0\,KJ/m^2$
L	$\sqrt{2}/10\,mm$	$\sqrt{2}\,mm$

Table 4.1: *Parameters chosen for the analytical curves of figure (4.1).*

It is noted that despite the errors in the novel damage formulation, specifically the improper definition of the vectors normal to the virtual cohesive interfaces and the incorrect sign correction of opening and traction components (detailed in sub-section (3.1.3)), the verification results appears to be correct.

Based on observations made in figure (4.2) an explanation is provided for why the verification results are correct despite the incorrect novel damage formulation. Firstly, it is highlighted that the verification results have been presented for the left element of figure (3.20), denoted as Ω_+. Considering the simultaneous fiber and matrix cracking scenario, the (wrong) parallel unit vector $\boldsymbol{n}_{\parallel}$ points in the same direction as the (correct) unit outward vector $\boldsymbol{n}^+_{\parallel}$ normal to the transverse virtual interface $s^+_{\perp}$, indicating that the parallel components $t^+_{\parallel}$ and $\Delta^+_{\parallel}$ implemented are correctly defined. Additionally, having $t^+_{\parallel}$ and $\Delta^+_{\parallel}$ the same sign as the normal traction and opening t^+_n and Δ^+_n defined according to the standard decomposition, the sign of $t^+_{\parallel}$ and $\Delta^+_{\parallel}$ is left unaltered by the (wrong) sign correction. This explains why the verification for the cohesive interface transverse to the fiber direction does not present issues. However, for the case of the cohesive interface parallel to the fiber direction, it is pointed out that the (incorrect) transverse unit vector $\boldsymbol{n}_{\perp}$ points in the opposite direction to the (correct) unit outward vector $\boldsymbol{n}^+_{\perp}$ normal to the parallel virtual interface $s^+_{\parallel}$, leading to the transverse components $t^+_{\perp}$

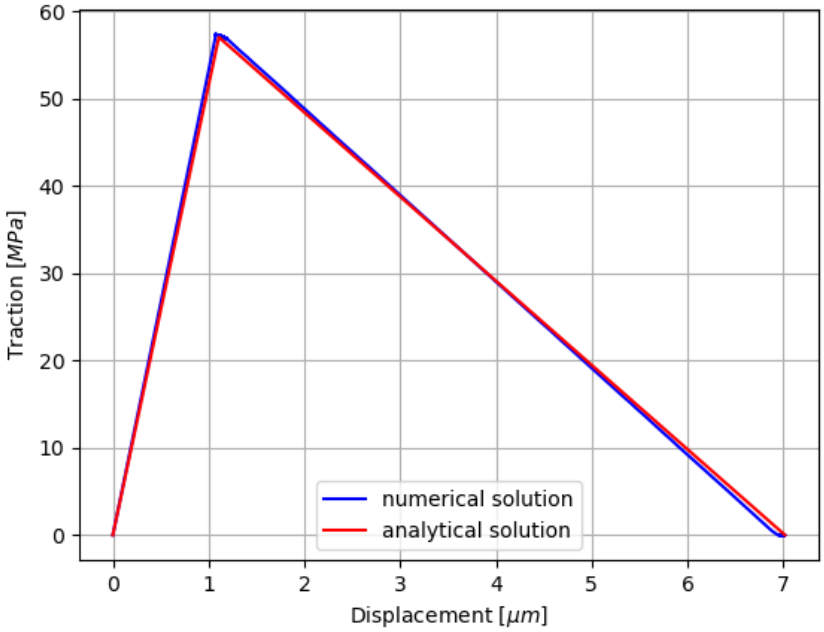

(a) Parallel interface configuration

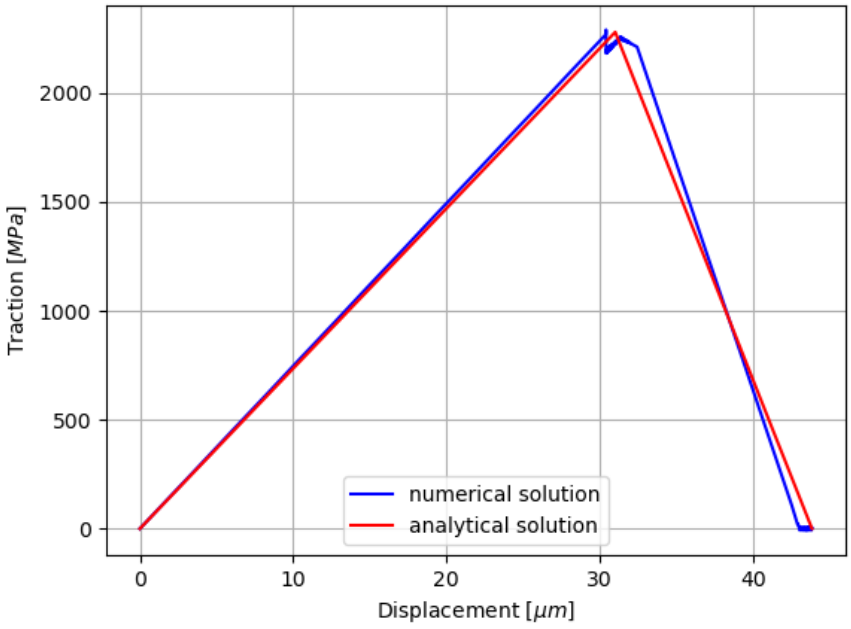

(b) Transverse interface configuration

Figure 4.1: *Comparison between the numerical and the analytical solution for the damage formulation verification. The numerical results are shown for the left element of figure (3.20). The figures qualitatively show the difference between the two solutions in terms of traction at the cohesive interface versus the displacement applied at the right node of the model.*

and $\Delta_{\perp}^{+}$ being defined with the wrong sign. Additionally, due to these $t_{\perp}^{+}$ and $\Delta_{\perp}^{+}$ components having the opposite sign compared to the normal traction and opening t_{n}^{+} and Δ_{n}^{+}, $t_{\perp}^{+}$ and $\Delta_{\perp}^{+}$ are reversed in sign during the (wrong) sign correction. Consequently, the verification for the cohesive interface parallel to the fiber direction appears to be correct despite the double mistake in the novel damage formulation.

It is noted that similar observations regarding the verification results could be made by considering the element Ω_{-}

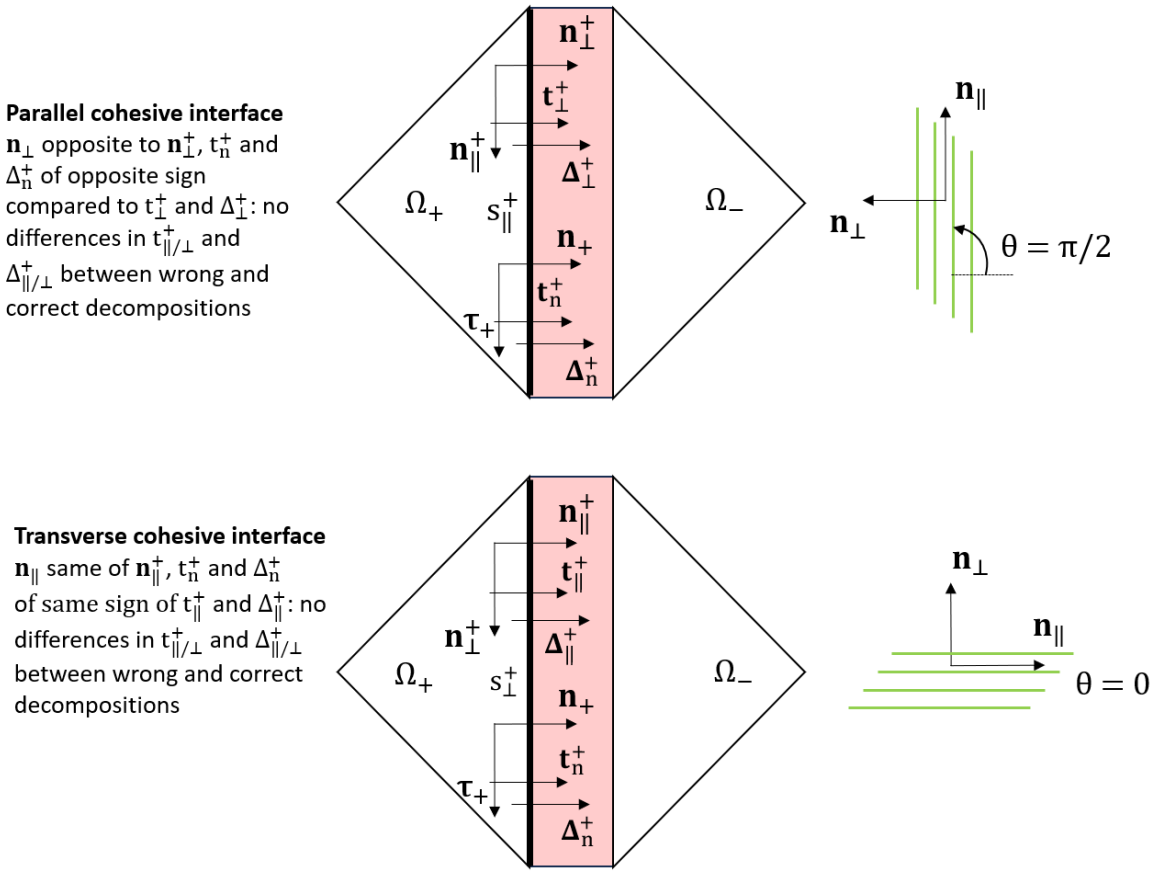

Figure 4.2: *The verification outcomes for the Ω_{+} element, as illustrated in figure (4.1), remain accurate for both cohesive interfaces parallel and transverse to the fiber direction, despite the errors within the implemented damage formulation. These errors concern the sign definition of vectors $\boldsymbol{n}_{\parallel}$ and $\boldsymbol{n}_{\perp}$, affecting the sign of components $t_{\parallel}^{+}$, $\Delta_{\parallel}^{+}$, $t_{\perp}^{+}$, and $\Delta_{\perp}^{+}$ evaluated on the virtual interfaces $s_{\perp}^{+}$ and $s_{\parallel}^{+}$, and the (incorrect) sign correction of $t_{\parallel}^{+}$, $\Delta_{\parallel}^{+}$, $t_{\perp}^{+}$ and $\Delta_{\perp}^{+}$ based on the sign of t_{n}^{+} and Δ_{n}^{+}.*

While the specific verification case examined in this study yielded satisfactory results, it's important to acknowledge the possibility of traction components at the virtual interfaces being defined with incorrect signs, even after the wrong sign adjustments. Such mismatch in sign could lead to cohesive interfaces opening when they should not or failing to open when they should. To exclude this potential issue and ensure the mismatch does not influence validation results presented in section (4.2), it is advisable to repeat the verification procedure with additional configurations where the traction components are defined with the wrong sign after sign adjustments. This would help establish the effect of the errors identified in the novel damage formulation.

4.2. Validation Results

Continuing with the examination of the results obtained for the novel Discontinuous Galerkin Cohesive Zone Model (DG/CZM) implemented in sub-section (3.4.2), aimed at replicating the experimental outcomes presented in sub-section (3.4.1), this section will analyze both the Force-Displacement (FD) curves and the numerical crack evolution.

Let's first compare the numerical and experimental FD curves depicted in figure (4.3). It is immedi-

ately apparent that the stiffness of the numerical curves does not match the experimental data retrieved from figure (3.24) even before damage onset when the novel damage formulation is not involved at all. The mismatch in stiffness before damage onset prompted an investigation into parameters related to the pre-fracture regime, excluding those solely related to the post-fracture regime:

- Material model definition: The orthotropic material model considered for validation is implemented in sub-section (3.2.1) and verified in sub-section (3.3.1). Since this model was successfully verified, it is not considered the cause of the stiffness mismatch;
- Crack Opening Displacement (COD) definition: The COD estimation in the numerical model is based on the difference in displacement of the two nodes at the opposite end to the crack tip, instead of the clip gauge reading done in the experiment and depicted in figure (3.25). However, this difference was proven not to significantly influence the stiffness;
- Pre-crack geometry definition: The pre-crack definition as a line with virtually no thickness, instead of a $1.5\,mm$ thick notch as in the experiment of Jose et al. [33], was not considered responsible for the difference in the slope of the curves;
- Material parameters selection: The variation of the material parameters ρ and ν_{23}, which are the only ones not retrieved from Jose et al. [33] but estimated in the present work, had a minor effect on the slope of the FD curves;
- Plane stress assumption: The thickness of the specimens being about 20 times smaller than the other dimensions, the plane stress mode assumed for the numerical model is not expected to deviate significantly from the 3D mode;
- Loading rate: Even with loading rates lower than those considered in the experiments of Jose et al. [33], no significant improvements on the stiffness were observed;
- Mesh size: Alternatively to implementing a coarse mesh in areas where damage is not anticipated, as illustrated in figure (3.26a), the mesh size of the entire specimen was selected to be sufficiently fine to ensure at least 3 FEs along the cohesive length l_{cz}, as estimated in equation (3.37). However, despite the refinement in these areas, no major effects on stiffness were observed;
- Element order: Elements of order up to cubic order were used, but they did not show appreciable improvement in stiffness compared to the quadratic elements used for the simulations whose results are shown.

Despite all the efforts in tracking down the issues, the discrepancy in the pre-fracture regime of the FD curves remains an open question.

Since the post-fracture results rely on pre-fracture results, any quantitative mismatch might propagate into the pre-fracture results as well. For this reason, the quantitative mismatch in the post-fracture regime is not analyzed. Instead, qualitative observations on damage behavior are provided through the visualization of the crack evolution.

Regarding the crack evolution for the $[90°]_{30}$ laminate depicted in figure (4.4), the numerical crack tends to follow the expected crack propagation observed in the experimental results illustrated in figure (3.23a). However, for the $[0°]_{30}$ laminate shown in figure (4.5), cracks propagate in two main directions, slightly biased towards the positive y direction. This contrasts with the experimental results shown in figure (3.23b), where the crack propagates along a single main direction parallel to the fiber direction.

The following remarks are made on the visualization of the numerical crack propagation:

- Stiffness mismatch in pre-fracture regime: Discrepancies observed in the pre-fracture FD curves, as illustrated in figure (4.3), might propagate into the post-fracture regime, casting doubt on the reliability of fracture behavior observations;
- Errors in novel damage formulation implementation: The results of figures (4.4) and (4.5), might be affected from errors in the novel damage formulation (sub-section (3.1.3)), namely the improper definition of the unit vectors normal to the virtual interfaces, together with the parallel and transverse opening and traction components, and the wrong sign correction applied to the parallel and transverse traction and opening components based on the sign of the components in the standard damage formulation. As pointed out in section (4.1), the mismatch in sign for the traction components could lead to cohesive interfaces opening when they should not or failing to open when they should;

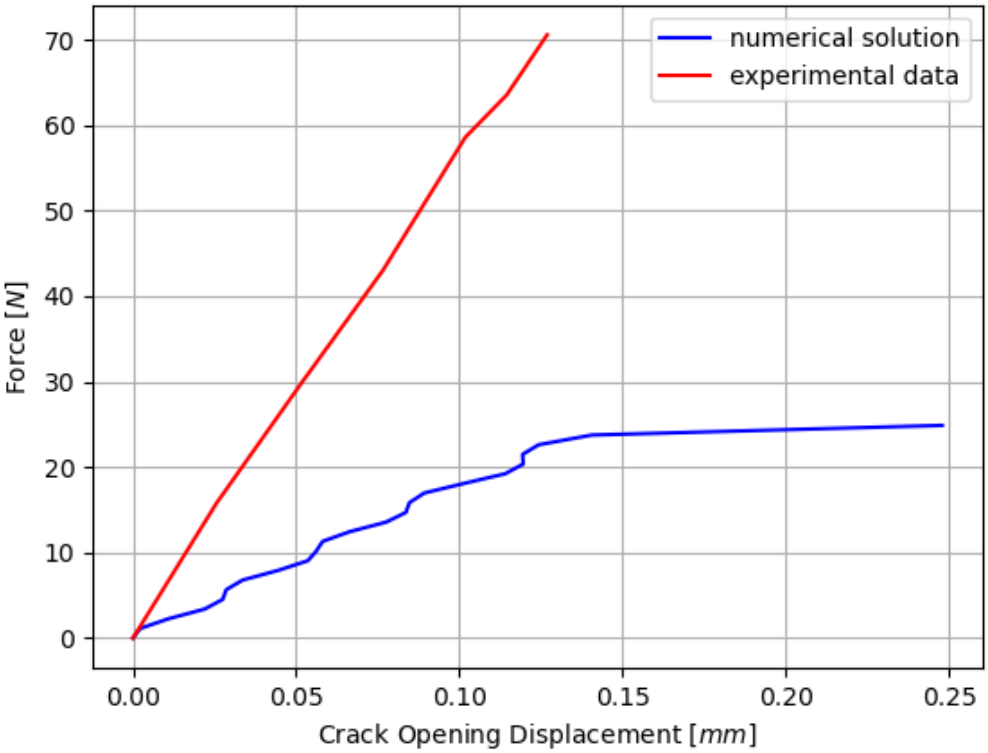

(a) 90 laminate FD curves

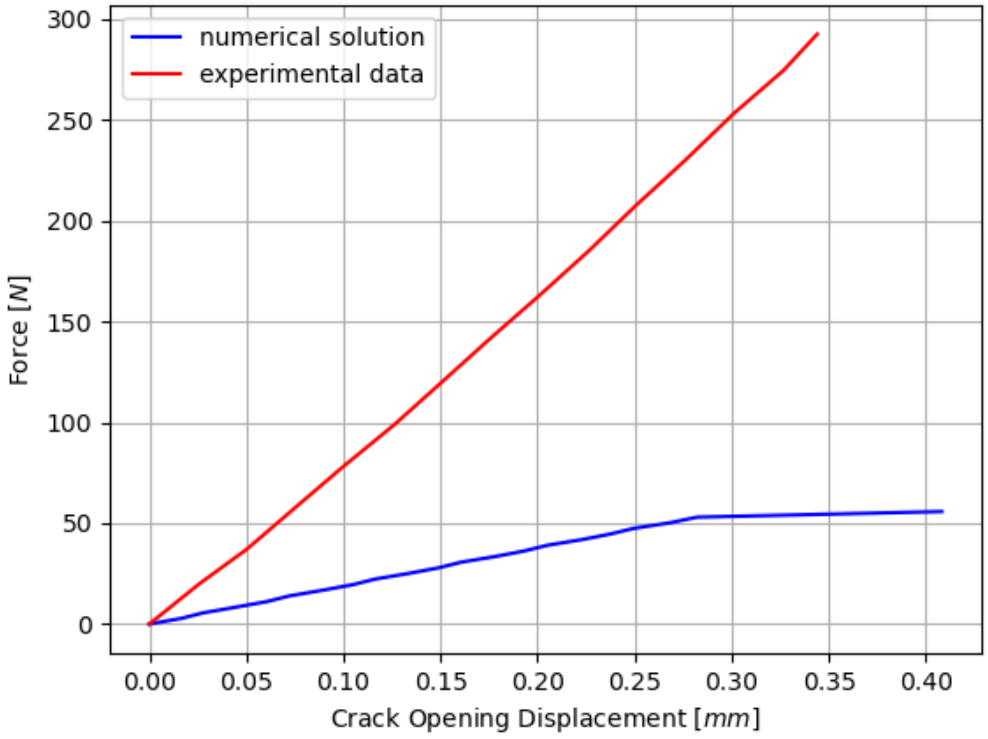

(b) 0 laminate FD curves

Figure 4.3: *The comparison between numerical and experimental FD curves for both the* $[90°]_{30}$ *and* $[0°]_{30}$ *laminates reveals a substantial discrepancy in stiffness. The numerical plot for the* $[90°]_{30}$ *laminate exhibits evident waviness, attributed to an excessively high load rate.*

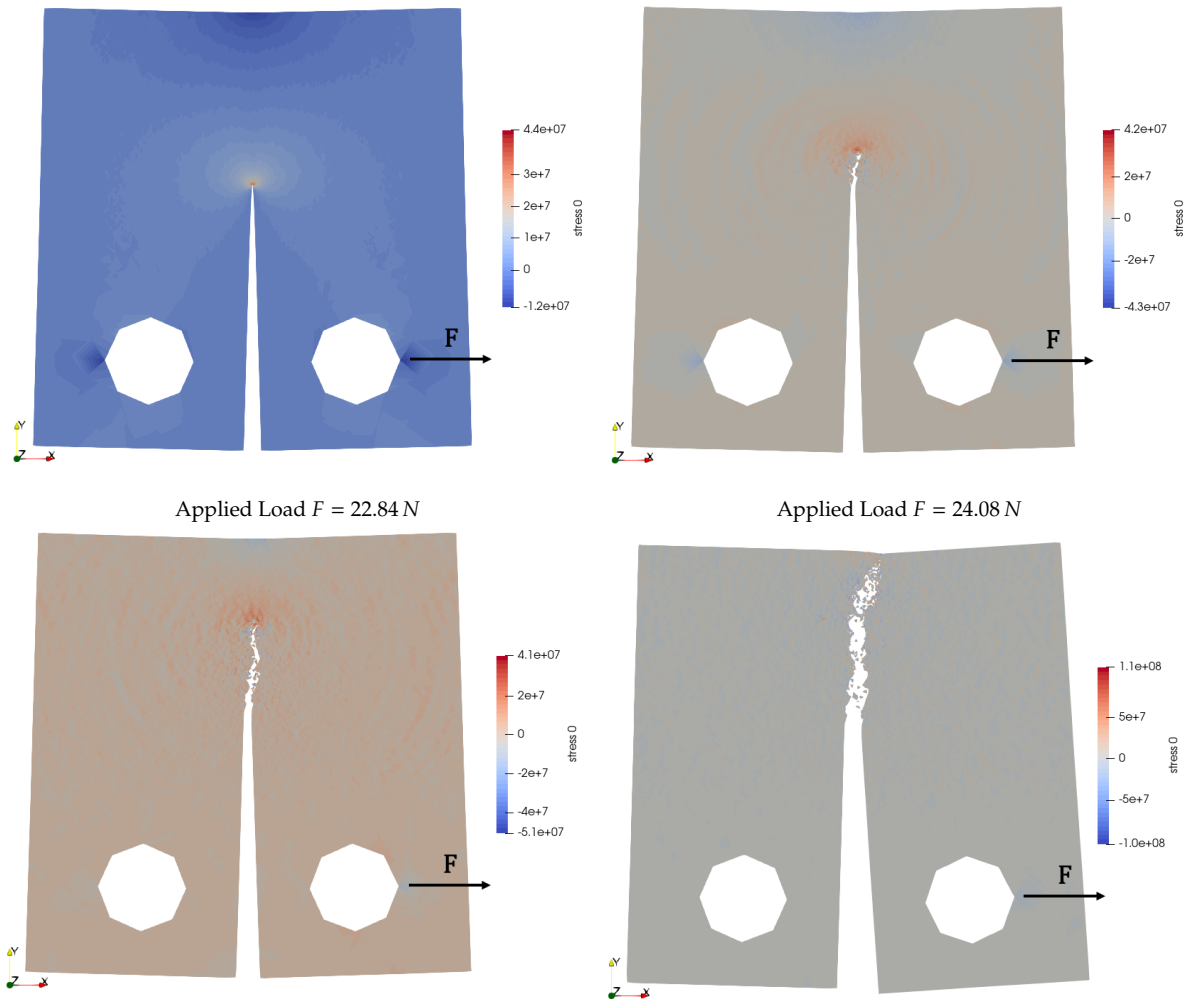

Applied Load $F = 22.84\,N$

Applied Load $F = 24.08\,N$

Applied Load $F = 24.42\,N$

Applied Load $F = 25.10\,N$

Figure 4.4: *Numerical crack evolution for the* $[90°]_{30}$ *laminate shown at different values of the applied load* $\mathbf{F}$*. To aid visualization of the crack, the displacement vector has been magnified by 20 times.* σ_0 *represents the* σ_x *stress in Pa for the plane stress laminate of the simulation, considered to be* $1\,m$ *thick. These stress values need to be scaled by the thickness ratio between the numerical thickness and that of the experiment. It is noted that the crack consists of matrix cracking only, and overall evolves along the fiber direction as expected from experimental data.*

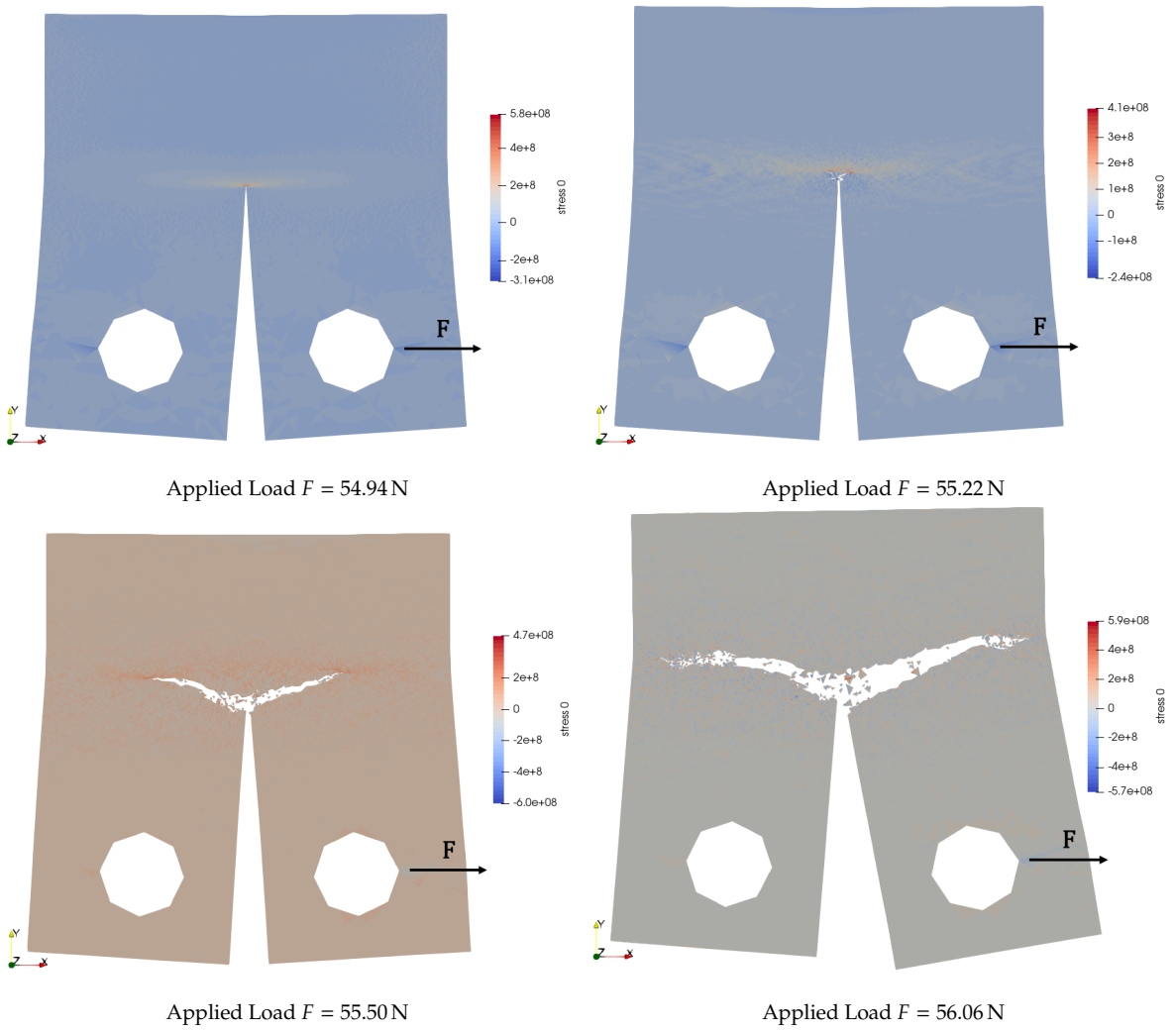

Applied Load $F = 54.94\,\mathrm{N}$ Applied Load $F = 55.22\,\mathrm{N}$

Applied Load $F = 55.50\,\mathrm{N}$ Applied Load $F = 56.06\,\mathrm{N}$

Figure 4.5: *Numerical crack evolution for the* $[0°]_{30}$ *laminate shown at different values of the applied load* $\boldsymbol{F}$*. To aid visualization of the crack, the displacement vector has been magnified by 20 times.* σ_0 *represents the* σ_x *stress in Pa for the plane stress laminate of the simulation, considered to be* $1\,m$ *thick. These stress values need to be scaled by the thickness ratio between the numerical thickness and that of the experiment. It is noted that the crack consists of matrix cracking only, and overall does not evolve along the fiber direction as expected from experimental data. Instead, there is a slight bias for the propagation along the* y *positive direction. Moreover, in contrast to experiments, the crack propagates along two distinct main directions, instead of one.*

- Novel damage formulation assumptions: It is likely that crack evolution is sensitive to the assumptions underlying the novel damage formulation (sub-section (3.1.3)), especially the neglect of shear opening effects. Taking into account these effects through a renewed and more comprehensive verification process considering interface configurations opening due to shear would probably improve both crack initiation and evolution results;
- Matrix cracking only: In both configurations depicted in figures (4.4) and (4.5), it is emphasized that only matrix cracking occurs. It is important to note that cracks appearing to cross the fiber direction are attributed to the assumptions underlying the novel damage formulation. This formulation relies on crack propagation along virtual interfaces parallel and transverse to the fiber direction, which then translates into propagation along the actual numerical interfaces. This may result in artificial propagation of matrix cracks across the fiber direction. By refining the mesh size, this tendency within the novel damage formulation framework is assumed to gradually diminish, aligning more closely with crack propagation observed in experiments;
- Propagation bias towards y direction for $[0°]_{30}$ laminate: As shown in figure (4.5), the crack propagation for the $[0°]_{30}$ laminate exhibits a slight bias towards the y positive direction instead of being along the x direction as observed in experiments. This bias may be caused by a mesh that is too structured, as indicated in figure (4.6) where many consecutive interfaces for the $[0°]_{30}$ laminate are oriented along the same direction, limiting freedom for crack propagation along an average horizontal direction parallel to the fibers;
- Propagation along two distinct main directions for $[0°]_{30}$ laminate: In the experimental case depicted in figure (3.23b), crack growth for laminate $[0°]_{30}$ occurs predominantly along a single direction. However, in the numerical simulation, the crack propagates in two distinct main directions. One possible explanation for this disparity could be the presence of material imperfections in real-world scenarios, which disrupt the symmetrical crack propagation of the numerical simulation and favor one direction over the other.

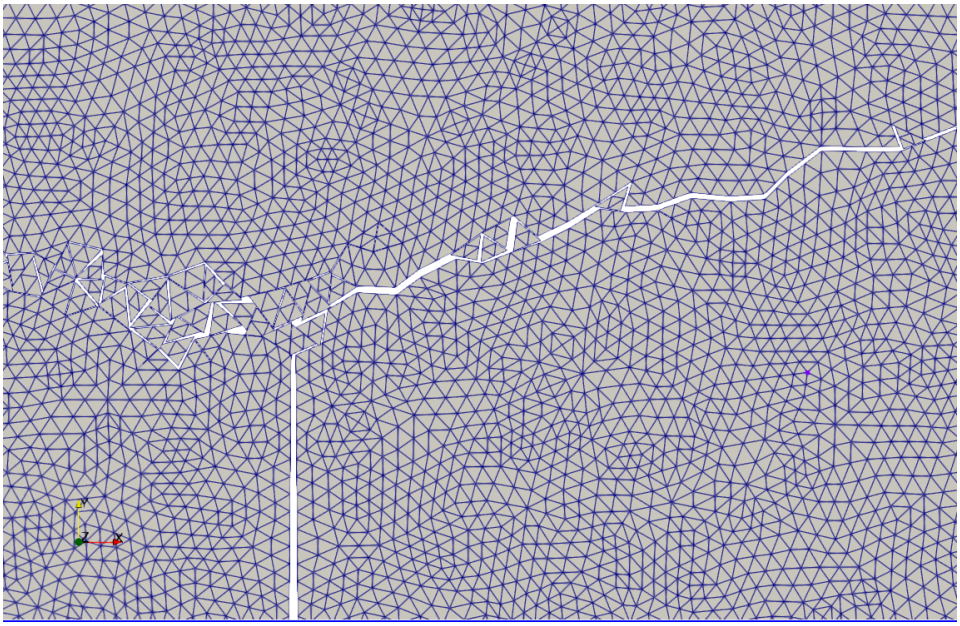

Figure 4.6: *Detail of the overly structured mesh for laminate* $[0°]_{30}$ *which could potentially contribute to bias in crack propagation towards the positive y direction. It is evident that many consecutive interfaces where crack occurs are aligned in the same direction. This alignment may restrict the freedom of crack propagation along an average horizontal direction parallel to the fibers.*

5

Conclusions

In this study, a novel Cohesive Zone Model (CZM) damage formulation for arbitrary fracture in composites was developed (sub-section (3.1.3)), implemented in the Summit-lite research code (section (3.2)), and verified against an analytical model (section (3.3)). Additionally, qualitative and quantitative validation against experimental data was conducted (section (3.4)).

The verification results (section (4.1)) initially suggested that the novel method accurately reproduces fracture onset and evolution for a cohesive interface under a tensile load transverse to it. However, subsequent analysis revealed errors in the novel damage formulation (sub-section (3.1.3)), particularly concerning the sign of the opening and traction components. Despite these errors, the specific verification case yielded satisfactory results as the errors partially cancelled each other out.

As the verification was assumed to be successful initially, a validation was conducted. The novel damage formulation qualitatively captures the fracture behavior observed in experimental data, but falls short in quantitative agreement (section (4.2)).

The qualitative visualization of crack evolution demonstrates that the novel method reproduces the overall damage pattern observed in Compact Tension (CT) test of composite Uni-Directional (UD) laminates. Nonetheless, there are noticeable issues with crack propagation in the $[0^\circ]_{30}$ laminate, especially a slight bias towards a direction transverse to the fiber direction. This issue may be related to overly-structured meshes which may cause biases in the crack propagation, or to the errors in the sign definition of opening and traction components in the novel damage formulation, and to its possibly over simplistic assumptions. These two concerns about the novel damage formulation should be addressed with a renewed and more comprehensive verification process that establishes their effects on the results.

Quantitative comparisons of Force-Displacement (FD) curves reveal discrepancies from the pre-fracture regime onwards, indicating that they are not entirely influenced by the novel damage formulation, and not at all up to fracture onset. Reasons for the errors in quantitative agreement before fracture initiation were thoroughly investigated (4.2), but specific causes could not be identified. The reasons for the quantitative mismatch in the post-fracture regime are assumed to be the the same as for the qualitative mismatch, and possibly also due to errors in the pre-fracture regime, as the post-fracture results rely on pre-fracture results.

Reflecting on the research question formulated in section (2.3) and reported here for convenience, an answer to it is now provided:

How can a novel CZM-based damage formulation be developed to facilitate arbitrary intra-laminar damage development by distinguishing between damage mechanisms based on the stress state of the laminate?

The novel damage formulation allows for arbitrary intra-laminar damage development based on the lamina stress state by decomposing numerical interfaces, along with the opening and traction acting on them, into parallel and transverse directions relative to the fiber direction of the lamina. Opening and traction components perpendicular to the virtual numerical interface aligned with the fiber direction are assumed to contribute to matrix damage along the fiber direction. Conversely, components perpendicular to the virtual numerical interface transverse to the fiber direction are assumed to contribute to simultaneous fiber and matrix damage transverse to the fiber direction. By assuming that damage virtually propagates along these virtual interfaces, where numerical fracture properties are known, and by considering the discrepancy in energy dissipation caused by the mismatch in length between the numerical interface and the virtual interface experiencing fracture, it becomes possible to model damage along arbitrary numerical interfaces solely based on the structural stress state.

In summary, the damage formulation developed in this study shows promise in qualitatively capturing arbitrary damage in composites based solely on the structural stress state. However, to assess the method suitability and validate its underlying assumptions, achieving a quantitative match between numerical simulations and experimental data is essential. Several factors contribute to the quantitative mismatch observed, including unidentified issues in the pre-fracture regime that require resolution. Additionally, errors in the sign of the opening and traction components, together with potentially overly simplistic assumptions of the novel damage method, contribute to the discrepancy. To ensure the accuracy and reliability of numerical results, a more comprehensive verification procedure should be developed. This procedure will assess the effects of these damage formulation errors and assumptions, helping to exclude any negative impact on the numerical outcomes of this work.

6

Recommendations

Based on the conclusions outlined in chapter (5), the following recommendations are provided:

- Ensure consistency in pre-fracture Force-Displacement (FD) curves: It is crucial to ensure consistency between the pre-fracture portions of numerical and experimental FD curves to effectively validate the novel damage formulation. Discrepancies observed in this stage may propagate into the post-fracture regime, potentially impacting the evaluation of the novel damage formulation's suitability to capture arbitrary intra-laminar damage in composites based on the structural stress state. To address this, a thorough examination of critical points mentioned in section (4.2) should be conducted. Additionally, verifying the reasonableness of test data from Jose et al. [33]'s article and assessing their compatibility with the numerical model assumptions of sub-section (3.4.2) is essential. Considering data from alternative sources or conducting new experiments may be necessary if discrepancies persist;
- Maintain consistency in post-fracture FD curves: Once quantitative agreement in the pre-fracture regime is achieved, it is possible to check for agreement in the post-fracture regime. Apart from errors in the pre-fracture regime, other elements are likely to influence the post-fracture results. To enhance accuracy:

    1. Address errors in novel damage formulation: Upon closer inspections, it was realized that mistakes in the sign of opening and traction components have been made in the novel damage formulation outlined in sub-section (3.1.3). These errors can be addressed by adjusting the unit normal vectors to the virtual interfaces, ensuring they point outward with respect to the Finite Element (FE) region. With this adjustment, there is no requirement to correct the sign of the opening and traction components based on those obtained for the standard decomposition, as mistakenly done in the present work. Unfortunately, these problems were not identified during the verification process outlined in section (3.3), leading to validation being conducted for the novel method containing errors. To ascertain that these errors do not adversely affect validation results, a more comprehensive verification process should be undertaken. This process should involve considering additional interface configurations with inverted traction components. By assessing the impact of these errors, particularly in terms of interfaces either erroneously initiating fracture or failing to initiate it when necessary, we can gain a deeper understanding regarding whether there were instances in the validation process where cohesive interfaces behaved incorrectly. Such insights are crucial for ensuring the reliability of the validation results;
    2. Revisit novel damage formulation assumptions: It is prudent to reconsider the assumptions underlying the novel damage formulation, as they may be overly simplistic and potentially unsuitable for accurately capturing experimental data from relevant literature. Specifically, reevaluating the contribution of both transverse and parallel components to the opening of virtual numerical interfaces, thereby incorporating a mixed-mode opening contribution rather than solely mode I as assumed in this study, could enhance the accuracy of damage simulation results. A renewed verification process could be developed to extend to interface

configurations opening under mixed-mode, allowing for observation of new validation results to assess whether the mode I opening assumption was overly simplistic or not;

3. Make the mesh more unstructured: To address the observed discrepancy in crack propagation for the $[0°]_{30}$ laminate, especially the slight deviation from the fiber direction compared to experimental data, employing a more unstructured mesh could be beneficial. This adjustment would provide greater freedom for crack evolution, thereby aligning it more closely with the expected crack path;

- Explore different fiber angles: Expanding simulations to include Uni-Directional (UD) laminate configurations with fiber angles other than 90° and 0° would provide insights into whether damage propagation patterns remain consistent across different orientations, showing damage propagation along the fiber direction;
- Extension to impact damage modeling: Future research efforts should focus on expanding the present approach to incorporate impact damage modeling, which is a significant concern in aerospace applications. If successful, the model could effectively simulate impact damage in composite laminates, encompassing both delamination and in-ply damage.

Bibliography

[1] M. Collinson. *MASTRO: Detecting barely visible damage with self-sensing carbon fibre components*. 2020.

[2] S. Z. Shah, S. Karuppanan, P. S. Megat-Yusoff, and Z. Sajid. "Impact resistance and damage tolerance of fiber reinforced composites: A review". *Composite Structures* 217 (June 2019), pp. 100–121. DOI: 10.1016/J.COMPSTRUCT.2019.03.021.

[3] T. Q. Bui and X. Hu. "A review of phase-field models, fundamentals and their applications to composite laminates". *Engineering Fracture Mechanics* 248 (May 2021). DOI: 10.1016/J.ENGFRACMECH.2021.107705.

[4] G. A. O. Davies and R. Olsson. "Impact on composite structures". *The Aeronautical Journal* 108 (1089 2004), pp. 541–563. DOI: 10.1017/S0001924000000385.

[5] R. Radovitzky, A. Seagraves, M. Tupek, and L. Noels. "A scalable 3D fracture and fragmentation algorithm based on a hybrid, discontinuous Galerkin, cohesive element method". *Computer Methods in Applied Mechanics and Engineering* 200 (2011), pp. 326–344. DOI: 10.1016/j.cma.2010.08.014.

[6] M. R. Wisnom. "Modelling discrete failures in composites with interface elements". *Composites Part A: Applied Science and Manufacturing* 41 (7 July 2010), pp. 795–805. DOI: 10.1016/J.COMPOSITESA.2010.02.011.

[7] R. Bogenfeld, J. Kreikemeier, and T. Wille. "Review and benchmark study on the analysis of low-velocity impact on composite laminates". *Engineering Failure Analysis* 86 (Apr. 2018), pp. 72–99. DOI: 10.1016/J.ENGFAILANAL.2017.12.019.

[8] Y. Shi, C. Pinna, and C. Soutis. "Modelling impact damage in composite laminates: A simulation of intra- and inter-laminar cracking". *Composite Structures* 114 (1 Aug. 2014), pp. 10–19. DOI: 10.1016/J.COMPSTRUCT.2014.03.052.

[9] S. Abrate, J. F. Ferrero, and P. Navarro. "Cohesive zone models and impact damage predictions for composite structures". *Meccanica* 50 (10 2015), pp. 2587–2620. DOI: 10.1007/s11012-015-0221-1.

[10] X. C. Sun, M. R. Wisnom, and S. R. Hallett. "Interaction of inter- and intralaminar damage in scaled quasi-static indentation tests: Part 2 – Numerical simulation". *Composite Structures* 136 (Feb. 2016), pp. 727–742. DOI: 10.1016/J.COMPSTRUCT.2015.09.062.

[11] D. J. Elder, R. S. Thomson, M. Q. Nguyen, and M. L. Scott. "Review of delamination predictive methods for low speed impact of composite laminates". *Composite Structures* 66 (1-4 Oct. 2004), pp. 677–683. DOI: 10.1016/J.COMPSTRUCT.2004.06.004.

[12] A. Tabiei and W. Zhang. "Composite laminate delamination simulation and experiment: A review of recent development". *Applied Mechanics Reviews* 70 (3 May 2018). DOI: 10.1115/1.4040448.

[13] A. Faggiani and B. G. Falzon. "Predicting low-velocity impact damage on a stiffened composite panel". *Composites Part A: Applied Science and Manufacturing* 41 (6 June 2010), pp. 737–749. DOI: 10.1016/J.COMPOSITESA.2010.02.005.

[14] Q. Guo, W. Yao, W. Li, and N. Gupta. "Constitutive models for the structural analysis of composite materials for the finite element analysis: A review of recent practices". *Composite Structures* 260 (Mar. 2021). DOI: 10.1016/J.COMPSTRUCT.2020.113267.

[15] A. Forghani, M. Shahbazi, N. Zobeiry, A. Poursartip, and R. Vaziri. "An overview of continuum damage models used to simulate intralaminar failure mechanisms in advanced composite materials". *Numerical Modelling of Failure in Advanced Composite Materials* (Jan. 2015), pp. 151–173. DOI: 10.1016/B978-0-08-100332-9.00006-2.

[16] S. Mukhopadhyay and S. R. Hallett. "A directed continuum damage mechanics method for modelling composite matrix cracks". *Composites Science and Technology* 176 (May 2019), pp. 1–8. DOI: 10.1016/J.COMPSCITECH.2019.03.022.

[17] T. Belytschko and T. Black. "Elastic crack growth in finite element with minimal remeshing". *International Journal for Numerical Methods in Engineering* 45.5 (1999), pp. 601–620. DOI: 10.1002/(SICI)1097-0207(19990620)45:5<601::AID-NME598>3.0.CO;2-S.

[18] N. Moës, J. Dolbow, and T. Belytschko. "A finite element method for crack growth without remeshing". *International Journal for Numerical Methods in Engineering* 46 (1999), pp. 131–150. DOI: 10.1002/(SICI)1097-0207(19990910)46:1%3C131::AID-NME726%3E3.0.CO;2-J.

[19] G. A. Francfort and J.-J. Marigo. "Revisiting brittle fracture as an energy minimization problem". *Journal of the Mechanics and Physics of Solids* 46 (1998), pp. 1319–1342. DOI: 10.1016/S0022-5096(98)00034-9.

[20] B. Bourdin, G. A. Francfort, and J.-J. Marigo. "Numerical experiments in revisited brittle fracture". *Journal of the Mechanics and Physics of Solids* 48.4 (2000), pp. 797–826. DOI: 10.1016/S0022-5096(99)00028-9.

[21] L. Ambrosio and V. M. Tortorelli. "Approximation of functional depending on jumps by elliptic functional via t-convergence". *Communications on Pure and Applied Mathematics* 43 (8 Dec. 1990), pp. 999–1036. DOI: 10.1002/cpa.3160430805.

[22] E. Tanné, T. Li, B. Bourdin, J. J. Marigo, and C. Maurini. "Crack nucleation in variational phase-field models of brittle fracture". *Journal of the Mechanics and Physics of Solids* 110 (Jan. 2018), pp. 80–99. DOI: 10.1016/J.JMPS.2017.09.006.

[23] G. I. Barenblatt. "The formation of equilibrium cracks during brittle fracture. General ideas and hypotheses. Axially-symmetric cracks." *Journal of Applied Mathematics and Mechanics* 23.3 (1959), pp. 622–636. DOI: 10.1016/0021-8928(59)90157-1.

[24] G. Barenblatt. "The mathematical theory of equilibrium cracks in brittle fracture". *Advances in Applied Mechanics* 7 (1962), pp. 55–129. DOI: 10.1016/S0065-2156(08)70121-2.

[25] D. S. Dugdale. "Yielding of steel sheets containing slits". *Journal of the Mechanics and Physics of Solids* 8 (2 May 1960), pp. 100–104. DOI: 10.1016/0022-5096(60)90013-2.

[26] A. Hillerborg, M. Modéer, and P.-E. Petersson. "Analysis of crack formation and crack growth in concrete by means of fracture mechanics and finite elements". *Cement and Concrete Research* 6 (1976), pp. 773–782. DOI: 10.1016/0008-8846(76)90007-7.

[27] B. Lecampion, A. Bunger, and X. Zhang. "Numerical methods for hydraulic fracture propagation: a review of recent trends". *Journal of Natural Gas Science & Engineering* 49 (2017), pp. 66–83. DOI: 10.1016/j.jngse.2017.10.012.

[28] B. Giovanardi. "Numerical Modeling of Hydro-Mechanical Coupling in Deformable Porous Media: Compaction and Fractures". Politecnico di Milano, 2016.

[29] U. Pillai. "Damage modelling in fibre-reinforced composite laminates using phase field approach". University of Nottingham, 2021.

[30] M. Alfano, F. Furgiuele, A. Leonardi, C. Maletta, and G. H. Paulino. "Mode I fracture of adhesive joints using tailored cohesive zone models". *International Journal of Fracture* 157 (1-2 2009), pp. 193–204. DOI: 10.1007/s10704-008-9293-4.

[31] M. Ortiz and A. Pandolfi. "Finite-deformation irreversible cohesive elements for three-dimensional crack-propagation analysis". *International Journal for Numerical Methods in Engineering* 44 (1999), pp. 1267–1282. DOI: 10.1002/(SICI)1097-0207(19990330)44:9<1267::AID-NME486>3.0.CO;2-7.

[32] L. Wu, D. Tjahjanto, G. Becker, A. Makradi, A. Jérusalem, and L. Noels. "A micro–meso-model of intra-laminar fracture in fiber-reinforced composites based on a discontinuous Galerkin/cohesive zone method". *Engineering Fracture Mechanics* 104 (May 2013), pp. 162–183. DOI: 10.1016/J.ENGFRACMECH.2013.03.018.

[33] S. Jose, R. R. Kumar, M. K. Jana, and G. V. Rao. "Intralaminar fracture toughness of a cross-ply laminate and its constituent sub-laminates". *Composites Science and Technology* 61 (2001), pp. 1115–1122. DOI: 10.1016/S0266-3538(01)00011-2.

[34] F. M. Monticeli, F. R. Fuga, and M. V. Donadon. "A systematic review on translaminar fracture damage propagation in fiber-reinforced polymer composites". *Thin-Walled Structures* 187 (June 2023). DOI: 10.1016/J.TWS.2023.110742.

[35] A. Turon, C. G. Dávila, P. P. Camanho, and J. Costa. "An engineering solution for mesh size effects in the simulation of delamination using cohesive zone models". *Engineering Fracture Mechanics* 74 (10 July 2007), pp. 1665–1682. DOI: 10.1016/J.ENGFRACMECH.2006.08.025.

[36] J.-A. Pascoe, S. Pimenta, and S. T. Pinho. *How to set up a cohesive zone model for an LEFM dominated problem: a detailed analysis for first time users*.

[37] J. N. Reddy. *Mechanics of Laminated Composite Plates and Shells Theory and Analysis*. CRC, 2004.

[38] C. Kassapoglou. *Design and analysis of composite structures with applications to aerospace structures*. Wiley, 2010.

A

Stress-Strain Equations for Composite Lamina

The 3D stress-strain equations for a composite lamina are derived by referring to the book of Reddy [37] as

$$\boldsymbol{\sigma}_{(xyz)} = \begin{bmatrix} \sigma_x \\ \sigma_y \\ \sigma_z \\ \sigma_{yz} \\ \sigma_{xz} \\ \sigma_{xy} \end{bmatrix} = \begin{bmatrix} Q_{11} & Q_{12} & Q_{13} & 0 & 0 & Q_{16} \\ Q_{12} & Q_{22} & Q_{23} & 0 & 0 & Q_{26} \\ Q_{13} & Q_{23} & Q_{33} & 0 & 0 & Q_{36} \\ 0 & 0 & 0 & Q_{44} & Q_{45} & 0 \\ 0 & 0 & 0 & Q_{45} & Q_{55} & 0 \\ Q_{16} & Q_{26} & Q_{36} & 0 & 0 & Q_{66} \end{bmatrix} \begin{bmatrix} \varepsilon_x \\ \varepsilon_y \\ \varepsilon_z \\ \gamma_{yz} \\ \gamma_{xz} \\ \gamma_{xy} \end{bmatrix} = \boldsymbol{Q}\boldsymbol{\varepsilon}_{(xyz)} \tag{A.1}$$

where the coefficients Q_{ij} are given by

$$\begin{aligned}
Q_{11} &= m^4 Q_{11}^0 + 2m^2 n^2 (Q_{12}^0 + 2Q_{66}^0) + n^4 Q_{22}^0 \\
Q_{22} &= n^4 Q_{11}^0 + 2m^2 n^2 (Q_{12}^0 + 2Q_{66}^0) + m^4 Q_{22}^0 \\
Q_{12} &= m^2 n^2 (Q_{11}^0 + Q_{22}^0 - 4Q_{66}^0) + (m^4 + n^4) Q_{12}^0 \\
Q_{13} &= m^2 Q_{13}^0 + n^2 Q_{23}^0 \\
Q_{23} &= n^2 Q_{13}^0 + m^2 Q_{23}^0 \\
Q_{33} &= Q_{33}^0 \\
Q_{16} &= m^3 n Q_{11}^0 - m n^3 Q_{22}^0 + (m n^3 - m^3 n)(Q_{12}^0 + 2Q_{66}^0) \\
Q_{26} &= m n^3 Q_{11}^0 - m^3 n Q_{22}^0 + (m^3 n - m n^3)(Q_{12}^0 + 2Q_{66}^0) \\
Q_{36} &= m n (Q_{13}^0 - Q_{23}^0) \\
Q_{44} &= m^2 Q_{44}^0 + n^2 Q_{55}^0 \\
Q_{55} &= n^2 Q_{44}^0 + m^2 Q_{55}^0 \\
Q_{45} &= m n (Q_{55}^0 - Q_{44}^0) \\
Q_{66} &= m^2 n^2 (Q_{11}^0 + Q_{22}^0 - 2Q_{12}^0) + (m^2 - n^2)^2 Q_{66}^0
\end{aligned} \tag{A.2}$$

The fiber angle θ dependence is expressed through the m and n parameters:

$$\begin{aligned}
m &= \cos\theta \\
n &= \sin\theta
\end{aligned} \tag{A.3}$$

The quantities

$$
\begin{aligned}
Q^0_{11} &= \frac{1-\nu_{23}\nu_{32}}{E_2E_3\Delta} \\
Q^0_{22} &= \frac{1-\nu_{13}\nu_{31}}{E_1E_3\Delta} \\
Q^0_{33} &= \frac{1-\nu_{12}\nu_{21}}{E_1E_2\Delta} \\
Q^0_{12} &= \frac{\nu_{21}+\nu_{31}\nu_{23}}{E_2E_3\Delta} \\
Q^0_{13} &= \frac{\nu_{31}+\nu_{21}\nu_{32}}{E_2E_3\Delta} \\
Q^0_{23} &= \frac{\nu_{32}+\nu_{12}\nu_{31}}{E_1E_3\Delta} \\
Q^0_{44} &= G_{23} \\
Q^0_{55} &= G_{13} \\
Q^0_{66} &= G_{12}
\end{aligned}
\tag{A.4}
$$

$$
\begin{aligned}
\nu_{21} &= \frac{E_2}{E_1}\nu_{12} \\
\nu_{31} &= \frac{E_3}{E_1}\nu_{13} \\
\nu_{32} &= \frac{E_3}{E_2}\nu_{23} \\
\Delta &= \frac{1-\nu_{12}\nu_{21}-\nu_{23}\nu_{32}-\nu_{31}\nu_{13}-2\nu_{21}\nu_{32}\nu_{13}}{E_1E_2E_3}
\end{aligned}
\tag{A.5}
$$

$$
\begin{aligned}
E_3 &= E_2 \\
G_{13} &= G_{12} \\
\nu_{13} &= \nu_{12} \\
G_{23} &= \frac{E_2}{2(1+\nu_{23})}
\end{aligned}
\tag{A.6}
$$

are functions of the lamina elastic parameters. $\boldsymbol{\sigma}_{(xyz)}$ and $\boldsymbol{\varepsilon}_{(xyz)}$ represent the stress and strain vectors in the laminate coordinate system (xyz), which may not necessarily coincide with the lamina reference system denoted by (123). The stiffness matrix $\boldsymbol{Q}$ is a function of the fiber angle θ, and the 5 independent elastic properties of the lamina: E_1, E_2, G_{12}, ν_{12}, ν_{23}. Several key assumptions underlie these stress-strain equations:

- Elastic hypothesis: Stress is assumed to vary linearly with strain;
- Homogeneous material hypothesis: The lamina is treated as macroscopically homogeneous, with its material properties derived from a weighted average of its constituent materials, namely the fiber and the matrix constituents;
- Transverse isotropy hypothesis: Isotropic material properties are assumed in the plane transverse to the fiber direction.

For further clarification, refer to the illustration of the laminate and lamina reference systems, and the fiber angle provided in figure (A.1).

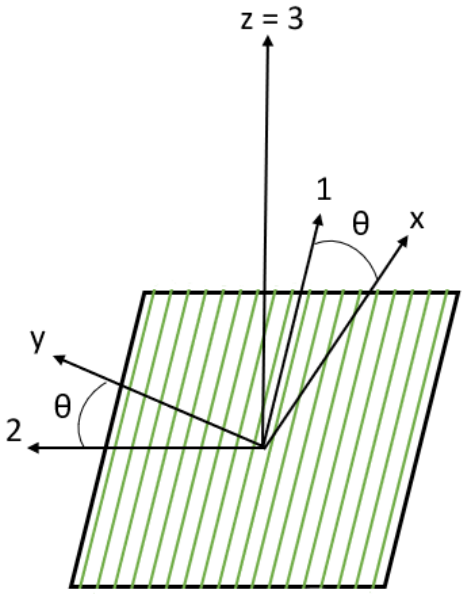

Figure A.1: *The fiber angle θ represents the deviation between the laminate reference system (xyz) and the lamina reference system* (123)*. In this context, direction* 1 *is aligned with the fiber direction, depicted in green, while direction* 2 *is orthogonal to the fiber direction.*

B

Classical Laminate Theory

The Classical Laminate Theory (CLT) provides an analytical framework for calculating strains and stresses in a composite laminate. The present derivation of the CLT equations is based on the book of Kassapoglou [38].

The CLT is based on several key assumptions:

- Plane stress mode assumption: The analysis assumes that the laminate experiences plane stress conditions, simplifying the 3D stress-strain equations for the lamina;
- Linear variation of strain: The strain in each lamina varies linearly along its thickness. This linear variation is characterized by pure membrane and pure bending deformations of the laminate;
- Standard Kirchhoff plate hypothesis: The theory follows the standard Kirchhoff plate theory, where plane sections remain plane and perpendicular to the neutral axis even after deformation;
- Uniform membrane strain: Each lamina experiences the same membrane strain, which is equal to the mid-plane strain of the laminate;
- Absence of intra- and inter-laminar damage: The theory assumes that there is no damage allowed within each lamina (intra-laminar) or between different laminae (inter-laminar);

The CLT stress-strain relations are obtained by following these steps:

1. Plane stress mode stress-strain equations: Under plane stress mode, the 3D stress-strain equations for a lamina (A.1) simplify into:

$$\boldsymbol{\sigma}_{(xy)} = \begin{bmatrix} \sigma_x \\ \sigma_y \\ \sigma_{xy} \end{bmatrix} = \begin{bmatrix} C_{11} & C_{12} & C_{16} \\ C_{12} & C_{22} & C_{26} \\ C_{16} & C_{26} & C_{66} \end{bmatrix} \begin{bmatrix} \varepsilon_x \\ \varepsilon_y \\ \gamma_{xy} \end{bmatrix} = \boldsymbol{C}\boldsymbol{\varepsilon}_{(xy)} \tag{B.1}$$

where the C_{ij} coefficients are given by

$$\begin{aligned}
C_{11} &= m^4 C_{11}^0 + 2m^2n^2(C_{12}^0 + 2C_{66}^0) + n^4 C_{22}^0 \\
C_{22} &= n^4 C_{11}^0 + 2m^2n^2(C_{12}^0 + 2C_{66}^0) + m^4 C_{22}^0 \\
C_{12} &= m^2n^2(C_{11}^0 + C_{22}^0 - 4C_{66}^0) + (m^4 + n^4)C_{12}^0 \\
C_{16} &= m^3nC_{11}^0 - mn^3C_{22}^0 + (mn^3 - m^3n)(C_{12}^0 + 2C_{66}^0) \\
C_{26} &= mn^3C_{11}^0 - m^3nC_{22}^0 + (m^3n - mn^3)(C_{12}^0 + 2C_{66}^0) \\
C_{66} &= m^2n^2(C_{11}^0 + C_{22}^0 - 2C_{12}^0) + (m^2 - n^2)^2 C_{66}^0
\end{aligned} \tag{B.2}$$

and the C_{ij}^0 coefficients are given by

$$\begin{aligned} C_{11}^0 &= \frac{E_1}{1-\nu_{12}\nu_{21}} \\ C_{22}^0 &= \frac{E_2}{1-\nu_{12}\nu_{21}} \\ C_{12}^0 &= \frac{\nu_{12}E_2}{1-\nu_{12}\nu_{21}} \\ C_{66}^0 &= G_{12} \end{aligned} \tag{B.3}$$

2. Linear strain-thickness equations: Due to the linearity of strain along the thickness, the strain at each ply k is expressed as a function of the mid-plane strains and curvatures of the laminate:

$$\boldsymbol{\varepsilon}_{(x,y)}^{(k)} = \begin{bmatrix} \varepsilon_x^{(k)} \\ \varepsilon_y^{(k)} \\ \gamma_{xy}^{(k)} \end{bmatrix} = \begin{bmatrix} \varepsilon_{x_0} \\ \varepsilon_{y_0} \\ \gamma_{xy_0} \end{bmatrix} + \begin{bmatrix} \kappa_x \\ \kappa_y \\ \kappa_{xy} \end{bmatrix} z^{(k)} = \boldsymbol{\varepsilon}_0 + \boldsymbol{\kappa} z^{(k)}, \quad z_{k-1} \leq z^{(k)} \leq z_k \tag{B.4}$$

Here, $\boldsymbol{\varepsilon}_0$ and $\boldsymbol{\kappa}$ represent the pure membrane and pure bending deformations of the laminate, or mid-plane strains and curvatures of the laminate. $z^{(k)}$ denotes the position across the thickness of the k-th ply;

3. Load-stress equations: The Boundary Conditions (BCs) are related to the stress at the laminate, where loads per unit width are expressed in terms of stresses integrated over the thickness:

$$\begin{aligned} N_x &= \int_{-h/2}^{h/2} \sigma_x \, dz \\ N_y &= \int_{-h/2}^{h/2} \sigma_y \, dz \\ N_{xy} &= \int_{-h/2}^{h/2} \sigma_{xy} \, dz \\ M_x &= \int_{-h/2}^{h/2} \sigma_x z \, dz \\ M_y &= \int_{-h/2}^{h/2} \sigma_y z \, dz \\ M_{xy} &= \int_{-h/2}^{h/2} \sigma_{xy} z \, dz \end{aligned} \tag{B.5}$$

where h is the thickness of the laminate. Figure (B.1) details the BCs applied to the laminate;

4. Mid-plane strains derivation: The CLT load-strain equations (B.6) are obtained by substituting strain-thickness equations (B.4) into stress-strain equations (B.1), and then into load-stress equations (B.5):

$$\begin{aligned} \begin{bmatrix} \boldsymbol{N} \\ \boldsymbol{M} \end{bmatrix} = \begin{bmatrix} N_x \\ N_y \\ N_{xy} \\ M_x \\ M_y \\ M_{xy} \end{bmatrix} &= \begin{bmatrix} A_{11} & A_{12} & A_{16} & B_{11} & B_{12} & B_{16} \\ A_{12} & A_{22} & A_{26} & B_{12} & B_{22} & B_{26} \\ A_{16} & A_{26} & A_{66} & B_{16} & B_{26} & B_{66} \\ B_{11} & B_{12} & B_{16} & D_{11} & D_{12} & D_{16} \\ B_{12} & B_{22} & B_{26} & D_{12} & D_{22} & D_{26} \\ B_{16} & B_{26} & B_{66} & D_{16} & D_{26} & D_{66} \end{bmatrix} \begin{bmatrix} \varepsilon_{x_0} \\ \varepsilon_{y_0} \\ \gamma_{xy_0} \\ \kappa_x \\ \kappa_y \\ \kappa_{xy} \end{bmatrix} \\ &= \begin{bmatrix} \boldsymbol{A} & \boldsymbol{B} \\ \boldsymbol{B} & \boldsymbol{D} \end{bmatrix} \begin{bmatrix} \boldsymbol{\varepsilon}_0 \\ \boldsymbol{\kappa} \end{bmatrix} \end{aligned} \tag{B.6}$$

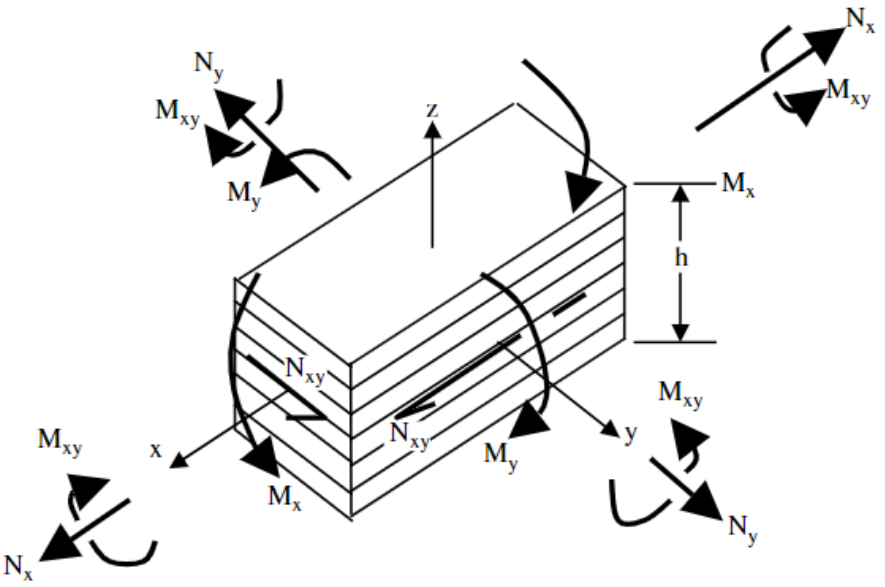

Figure B.1: *Illustration of the BCs in terms of loads per unit width for the CLT. The stretching and shearing loads are denoted by N_x, N_y, and N_{xy}, while the bending and torsion moments are denoted by M_x, M_y, and M_{xy}. The thickness of the laminate is represented by h. Figure credits: Kassapoglou [38].*

where

$$A_{ij} = \sum_{k=1}^{NP} C_{ij}^{(k)}(z_k - z_{k-1})$$
$$B_{ij} = \sum_{k=1}^{NP} C_{ij}^{(k)} \frac{(z_k^2 - z_{k-1}^2)}{2}$$
$$D_{ij} = \sum_{k=1}^{NP} C_{ij}^{(k)} \frac{(z_k^3 - z_{k-1}^3)}{3} \tag{B.7}$$

and NP is the number of plies. The mid-plane strains and the curvatures of the laminate are obtained by inverting load-strain equations (B.6):

$$\begin{bmatrix} \boldsymbol{\varepsilon}_0 \\ \boldsymbol{\kappa} \end{bmatrix} = \begin{bmatrix} \boldsymbol{a} & \boldsymbol{b} \\ \boldsymbol{b} & \boldsymbol{d} \end{bmatrix} \begin{bmatrix} \boldsymbol{N} \\ \boldsymbol{M} \end{bmatrix} \tag{B.8}$$

where

$$\begin{bmatrix} \boldsymbol{a} & \boldsymbol{b} \\ \boldsymbol{b} & \boldsymbol{d} \end{bmatrix} = \begin{bmatrix} \boldsymbol{A} & \boldsymbol{B} \\ \boldsymbol{B} & \boldsymbol{D} \end{bmatrix}^{-1} \tag{B.9}$$

5. Stress function of mid-plane strains: Finally, mid-plane strains and curvatures of the laminate are substituted into strain-thickness equations (B.4), and then into stress-strain equations (B.1):

$$\boldsymbol{\sigma}^{(k)} = \begin{bmatrix} \sigma_x^{(k)} \\ \sigma_y^{(k)} \\ \sigma_{xy}^{(k)} \end{bmatrix} = \begin{bmatrix} C_{11}^{(k)} & C_{12}^{(k)} & C_{16}^{(k)} \\ C_{12}^{(k)} & C_{22}^{(k)} & C_{26}^{(k)} \\ C_{16}^{(k)} & C_{26}^{(k)} & C_{66}^{(k)} \end{bmatrix} \left(\begin{bmatrix} \varepsilon_{x_0} \\ \varepsilon_{y_0} \\ \gamma_{xy_0} \end{bmatrix} + \begin{bmatrix} \kappa_x \\ \kappa_y \\ \kappa_{xy} \end{bmatrix} z^{(k)} \right) = \tag{B.10}$$
$$= \boldsymbol{C}^{(k)}(\boldsymbol{\varepsilon}_0 + \boldsymbol{\kappa} z^{(k)}), \quad z_{k-1} \leq z^{(k)} \leq z_k$$

C

Weak Formulation of Discontinuous Galerkin Cohesive Zone Model

The derivation of the Discontinuous Galerkin Cohesive Zone Model (DG/CZM) weak formulation of the equilibrium of the linear momentum is adapted from the one in the article by Radovitzki et al. [5]. The weak formulation provides a solution for the displacement $\boldsymbol{u}$ at a given quadrature point of the cohesive interface. The main assumptions for this formulation include small deformations, linear elastic stress-strain equations, and linear extrinsic Cohesive Law (CL). The derivation involves several steps, which are summarized as follows:

1. Strong formulation: The equilibrium of linear momentum entails balancing inertial, internal, and body forces $\boldsymbol{b}$ acting over a domain Ω. This equation is solved in terms of displacement, with BCs specified as traction $\hat{\boldsymbol{t}}$ at the Neumann boundary Γ_n and displacement $\hat{\boldsymbol{u}}$ at the Dirichlet boundary Γ_d. The strong formulation is expressed as follows:

$$\begin{aligned} \rho \frac{\partial^2 \boldsymbol{u}}{\partial t^2} &= \boldsymbol{\nabla} \cdot \boldsymbol{\sigma} + \boldsymbol{b}, \quad \text{in } \Omega \\ \boldsymbol{\sigma} \boldsymbol{n} &= \hat{\boldsymbol{t}}, \quad \text{on } \Gamma_n \\ \boldsymbol{u} &= \hat{\boldsymbol{u}}, \quad \text{on } \Gamma_d \end{aligned} \tag{C.1}$$

   Here, ρ represents density, $\boldsymbol{\sigma}$ denotes Cauchy's stress tensor, $\boldsymbol{n}$ signifies the unit vector normal to the boundary of the domain Γ. Under the assumptions of small deformations and linear elastic stress-strain relations, $\boldsymbol{\sigma}$ is expressed as a linear function of the displacement $\boldsymbol{u}$:

$$\boldsymbol{\sigma} = \boldsymbol{C} \boldsymbol{\varepsilon} = \boldsymbol{C} \frac{1}{2} [\nabla \boldsymbol{u} + (\nabla \boldsymbol{u})^T] \tag{C.2}$$

   Here, $\boldsymbol{C}$ represents the stiffness tensor, and $\boldsymbol{\varepsilon}$ signifies the strain tensor;

2. Discontinuous Galerkin (DG) weak formulation: The weak formulation is derived from the strong formulation by multiplying it by a trial function $\delta \boldsymbol{u}$. By integrating by parts and applying the divergence theorem, we arrive at the weak formulation. Unlike the Continuous Galerkin (CG) formulation, the DG approach does not strongly enforce the continuity of the displacement across the inter-element boundaries. Consequently, the test function $\boldsymbol{u}$ and the trial function $\delta \boldsymbol{u}$ are discontinuous at these boundaries. Therefore, integration by parts is performed over each element Ω_e rather than the entire domain Ω to yield the DG weak formulation:

$$\begin{aligned} \sum_e \int_{\Omega_e} \rho \frac{\partial^2 \boldsymbol{u}}{\partial t^2} \cdot \boldsymbol{\delta u} \, dV + \sum_e \int_{\Omega_e} \boldsymbol{\sigma} \cdot \nabla \boldsymbol{\delta u} \, dV = \\ = \sum_e \int_{\Gamma_e} \boldsymbol{\delta u} \cdot \boldsymbol{\sigma n} \, dS + \sum_e \int_{\Omega_e} \boldsymbol{b} \cdot \boldsymbol{\delta u} \, dV \end{aligned} \tag{C.3}$$

The domain boundary Γ is now partitioned into Γ_n and Γ_d. Additionally, Γ_d is subdivided into the outer region of the domain Γ_{ext} and the inter-element boundaries region Γ_{int}. Assuming that the trial function $\delta\boldsymbol{u}$ is 0 on Γ_{ext} and introducing the jump operator at the interface of two elements $[[\cdot]] = (\cdot^+ - \cdot^-)$, equation (C.3) is modified to

$$\int_\Omega \rho \frac{\partial^2 \boldsymbol{u}}{\partial t^2} \cdot \boldsymbol{\delta u}\, dV + \int_\Omega \boldsymbol{\sigma} \cdot \nabla \boldsymbol{\delta u}\, dV + \int_{\Gamma_{int}} [[\boldsymbol{\delta u} \cdot \boldsymbol{\sigma}]] \cdot \boldsymbol{n}^-\, dS = \\ = \int_{\Gamma_n} \boldsymbol{\delta u} \cdot \hat{\boldsymbol{t}}\, dS + \int_\Omega \boldsymbol{b} \cdot \boldsymbol{\delta u}\, dV \quad \text{(C.4)}$$

3. Inter-element flux term: Further manipulations are conducted on the inter-element boundary term. By introducing the average operator $\langle\cdot\rangle = \frac{1}{2}(\cdot^+ - \cdot^-)$, the inter-element boundary term becomes

$$\int_{\Gamma_{int}} [[\boldsymbol{\delta u} \cdot \boldsymbol{\sigma}]] \cdot \boldsymbol{n}^-\, dS = \int_{\Gamma_{int}} [[\boldsymbol{\delta u}]] \cdot \langle \boldsymbol{\sigma} \rangle \cdot \boldsymbol{n}^-\, dS + \int_{\Gamma_{int}} \langle \boldsymbol{\delta u} \rangle \cdot [[\boldsymbol{\sigma}]] \cdot \boldsymbol{n}^-\, dS = \\ = \int_{\Gamma_{int}} [[\boldsymbol{\delta u}]] \cdot \langle \boldsymbol{\sigma} \rangle \cdot \boldsymbol{n}^-\, dS = \int_{\Gamma_{int}} [[\boldsymbol{\delta u}]] \cdot \boldsymbol{h}\, dS \quad \text{(C.5)}$$

The inter-element boundary term addresses the discontinuity in displacement across inter-element boundaries by introducing a numerical flux $\boldsymbol{h} = \langle\boldsymbol{\sigma}\rangle\boldsymbol{n}^-$. The flux is proportional to the average of the stress tensor $\langle\boldsymbol{\sigma}\rangle$ at the two neighboring elements Ω_+ and Ω_-, as the stress tensor can experience discontinuity due to the weak enforcement of displacement continuity. The flux ceases to operate once fracture is activated at the given quadrature point;

4. Stabilization term: To weakly enforce displacement continuity at inter-element boundaries, a stabilization term is introduced:

$$\int_{\Gamma_{int}} [[\boldsymbol{\delta u}]] \otimes \boldsymbol{n}^- \cdot \langle \frac{\beta_s}{l_{ms}} \boldsymbol{C} \rangle \cdot [[\boldsymbol{u}]] \otimes \boldsymbol{n}^-\, dS \quad \text{(C.6)}$$

This term is crucial for ensuring numerical stability. The penalty stabilization parameter β_s determines the strength of displacement continuity enforcement. Notably, by assuming β_s to be infinite transitions from the DG to the CG method. In the stabilization term, l_{ms} is the mesh size;

5. Cohesive fracture initiation criterion: Upon damage initiation, the operation of the flux term and the stabilization term ceases, while the Traction-Separation Law (TSL) term comes into effect. To appropriately handle contributions before and after damage initiation, a boolean parameter α is introduced. α transitions from 0 to 1 once the fracture initiation criterion at the quadrature point is met. The function $\boldsymbol{t}([[\boldsymbol{u}]])$ present in the TSL term is explicitly derived in section (3.1);

6. DG/CZM weak formulation: In equation (C.4), the inter-element flux term is rewritten as shown in equation (C.5). Additionally, the stabilization term (equation (C.6)) and the TSL term are included. To account fracture initiation, the α correction is introduced. The resulting DG/CZM weak formulation is given by:

$$\int_\Omega \rho \frac{\partial^2 \boldsymbol{u}}{\partial t^2} \cdot \boldsymbol{\delta u}\, dV + \int_\Omega \boldsymbol{\sigma}(\nabla \boldsymbol{u}) \cdot \nabla \boldsymbol{\delta u}\, dV + \int_{\Gamma_{int}} \alpha \boldsymbol{t}([[\boldsymbol{u}]]) \cdot \boldsymbol{\delta u}\, dS + \\ + \int_{\Gamma_{int}} (1-\alpha)[[\boldsymbol{\delta u}]] \cdot \langle \boldsymbol{\sigma}(\nabla \boldsymbol{u}) \rangle \boldsymbol{n}^-\, dS + \\ + \int_{\Gamma_{int}} (1-\alpha)[[\boldsymbol{\delta u}]] \otimes \boldsymbol{n}^- \cdot \langle \frac{\beta_s}{l_{ms}} \boldsymbol{C} \rangle \cdot [[\boldsymbol{u}]] \otimes \boldsymbol{n}^-\, dS = \\ = \int_{\Gamma_n} \boldsymbol{\delta u} \cdot \hat{\boldsymbol{t}}\, dS + \int_\Omega \boldsymbol{b} \cdot \boldsymbol{\delta u}\, dV \quad \text{(C.7)}$$

It is noted that the present equation is linear in $\boldsymbol{u}$, implying that it can be integrated exactly in space by selecting a linear quadrature rule.